THÈSE

En vue de l'obtention du

DOCTORAT DE L'UNIVERSITÉ DE TOULOUSE

Délivré par :
Institut National Polytechnique de Toulouse (INP Toulouse)

Discipline ou spécialité :
Dynamique des fluides

Présentée et soutenue par :
Mario FALESE

le : 07/10/2013

Titre :

A study of the effects of bifurcations in swirling flows using Large Eddy Simulation and mesh adaptation

---

Ecole doctorale :
Mécanique, Energétique, Génie civil et Procédés (MEGeP)

Unité de recherche :
CERFACS

Directeur(s) de Thèse :
Thierry Poinsot
Eleonore RIBER

Rapporteurs :
Stephan MOREAU
Patrick BONTOUX

Membre(s) du jury :

Pascal BRUEL
François GALLAIRE
Vincent MOUREAU
Cecile DOBRZYNSKI

A study of the effects of bifurcations in swirling flows using Large Eddy Simulation and mesh adaptation

Mario Falese

October 7, 2013

This manuscript is dedicated to the two masters I never knew:
Max Stirner who teached me grammar,
Ernst Junger who showed me how to make poetry out of it.

Abstract and *Résumeé en français*

Swirling flows, which are widely employed in gas turbines, are known to undergo bifurcation between different topologies (large reconfigurations of the flow field) affecting the engine performance and safety.
This work focuses on the study of such bifurcations using Large-Eddy Simulation (LES). It shows that a small change in the fluid dynamics conditions, induced by the different Sub-Grid Scale (SGS) models used in the simulations, can cause a transition between two, distinct, flow states when the swirling flow is close to transition conditions. The sensitivity of LES to SGS modeling is also identified as the result of a lack of mesh resolution at some critical locations, a problem which is analyzed using mesh adaptation. Mesh adaptation is tested on canonical and industrial flows. Here, by adjusting the mesh resolution based on the characteristics of the flow examined (refining and coarsening the grid keeping constant the numerical cost), substantial improvements of the LES predictions can be obtained.
This work can be considered as the first step toward the establishment of a standard (repeatable and user independent) meshing procedure for LES.

Les écoulements tourbillonnants, qui sont largement utilisés dans les turbines à gaz, sont connus pour etre subject a des bifurcationnes entre différentes topologies (grandes reconfigurations du champ d'écoulement) qui peuvent affecter les performances et la sécurité du moteur.
Ce travail se concentre sur l'étude de ces bifurcations en utilisant la simulation aux grandes échelles (LES). Ce travail montre qu'un petit changement dans les conditions dynamique du fluide, induite par les différentes modèles de sous-maille utilisés, peut provoquer une transition entre deux, distincts, régimes d'écoulement lorsque l'écoulement tourbillonnaire est proche des conditions de critiques et de transition. La sensibilité des la LES au modeles de sous-maille est également identifié comme le résultat d'un manque de résolution à certains endroits critiques, un problème qui est analysé en utilisant une methode d'adaptation du maillage. L' adaptation du maillage est testé sur des cas accademique et industrielle. Ici, par ajustement de la résolution du maillage sur la base des caractéristiques de l'écoulement étudié (affinage et le grossissement de la grille en maintenant constant le coût numérique), des améliorations substantielles des prédictions de la LES peuvent être obtenue.
Ce travail peut être considéré comme une des premières étapes vers la mise en place d'une procédure standard (reproductible et utilisateur indépendant) de maillage pour la LES.

Thanks

It was always a good place for working (...)
Some other places were not so good,
but maybe we were not so good when we were in them.
E. Hemingway

I would like to thanks the following people. Geoffroy (aka *J'ai frois* or *le tap*) and Mi, my good friends and fellow sailors in the mediterranean sea. Lukash Kuban (aka *Mastro Lindo* or *Monsieur Proper*) my fellow polish liberal, Dmitry Kolomenskiy, Guillame Le Coq (aka *Olivia*) and Matthias Kraushaar with whom I shared some weird months living in meteofrance (and a weird week in Poland). Javier Urzay, who showed me the power of pen-and-paper.
All my collegues at CERFACS: Gregory Hannebiq (aka *le Canard*) and Basti Hermerth (aka *l'allemande*), Remy Franzen, Emmanuel Motheau (a good example of "la france profonde"), Stephane Jaure (whose conversations about coding in C helped me a lot) et JP Rocchi, Anthony Ruiz (whose conversations about LOTAR helped me a lot), Ignacio Duran (see you in London), Pablo Salas (aka *the brandy guy*, who opened my eyes on "les vins du sud-ouest"), Pierre Quillarte (aka *le rouge*) and David (aka *le petit muscle*) who had the pleasure to play with a superior italian footballer (yes, I brought football knowdlege to you, frenchies), Jerome Dombard and Elza Gullaud and Sandrine Berger (fellow sailors) and Abdulla Ghani (who, the legend says, is doing my PhD at my place), and all the others who shared with me the last 3 years at CERFACS. Also, I would like to thank (in chronological order) Valentina and Marta, my sweets.

I want to thank the real Chief of CERFACS (Marie Labadens) and Nicole Boutet and all the people of CSG and administration, above all Michelle Campassens. Laurent Giquel, Gabriel Staffelbach and Jens Muller for all their help/supervision during my thesis. Cecile Dobrzynski from INRIA for MMG3D, then all the seniors of CERFACS: Eleonore, Benedicte, Antoine, Olivier and Frank Nicoud who were always available for a scientific chat: all of this was useful. Thanks to the reviewers of this manuscript and to all the members of the jury. Finally, I want to thank my supervisor Thierry Poinsot for his scientific guidance and supervision.

Contents

Chapter 1

Introduction

Aeronautical transportation is one of the few markets un-affected by the world economic crisis. For instance, the long-range forecasts of the two major aircraft builders, AIRBUS and Boeing, predict an agglomerate business of more than 7 trillions dollar (7×10^{10}\$) between now and 2030 thanks to a combination of both emerging-market and rich world growth.
The source of demand is driven by the rising numbers of urban middle-class people (a demand insensitive to any world crisis, see Fig. 1.1 left), but also, from the rich world, by the need to replace ageing and inefficient planes in order to fulfill new regulations on emissions [1]. For instance, new regulations (demanded by the Advisory Council for Aero-

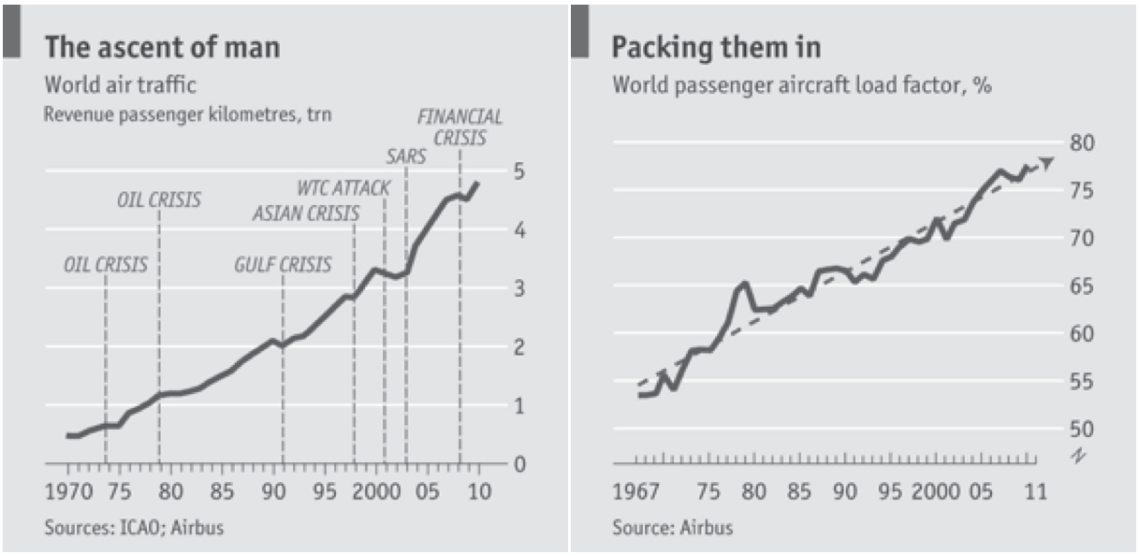

Figure 1.1: From [1]. Growth trend of aeronautical passengers and airplanes load factor.

nautics Research in Europe) will force a reduction of the exhaust greenhouse gases such as CO2 by 50% and of pollutant such as NOx by 80% in 2020 [55]. This context explains the need for new engine designs to gain in efficiency and reduce pollution[1].
Aeronautical propulsion relies heavily on combustion technology, therefore reducing green-

[1]Note that a large increase in efficiency is given by the growing airplane load factor [1] (Fig. 1.1 right).

house gases and pollutant consists mainly in improving combustion. Other propulsion systems (i.e. not involving combustion) are limited to small-scale unmanned or proof-of-concept research applications [47]. Fig. 1.2 shows a typical aircraft modern engine. In

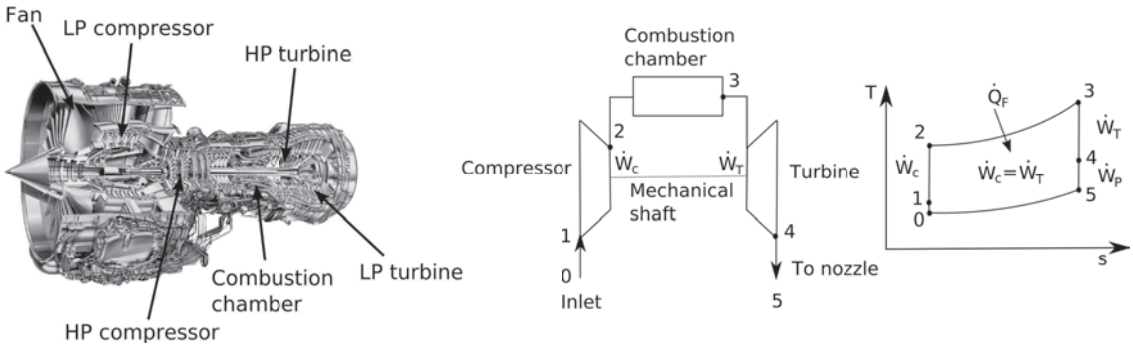

Figure 1.2: From [101]. Left: a typical aircraft modern engine, a turbogas (V 2500). Center: scheme of a simplified jet engine operation and the associated idealized Joule-Brayton cycle (right).

such combustion-based propulsion systems (Fig. 1.2) energy conversion, from the chemical energy of the fuel to internal energy of the gas, takes place in the combustion chamber which is therefore central in the engine performance. Almost all gas turbines combustion systems employ swirl flows whose dynamics are determined by the swirler geometry (Fig. 1.3). The swirler is a device which is mounted at the entry of the combustion chamber to generate a flow which helps to stabilize the flame, by the transport of burnt gases at the fuel injection point and to improve mixing via higher turbulence levels. This thesis focuses on the simulation of the complex flow field generated by such devices: the swirling injection system.

1.1 Swirling injection systems

Swirling injection systems used in most gas turbines lead to complex flows which control the fuel atomization, the shape of the recirculating zone produced in front of the swirler and ultimately a large part of the performances of the engine. Predicting these flows has been a major challenge for CFD for a long time. It did not take a long time to realize that RANS codes (predicting mean steady turbulent flows) had difficulties in these flows with strong rotation and LES has rapidly proved its superior potential, allowing to capture not only the mean flow velocity fields with precision but also the flow instabilities, such as the PVC (Precessing Vortex Core), with or without combustion, for gaseous or liquid fuels [42, 99, 11, 5].

Fig. 1.3 (left) displays a typical LES result performed in 2004 by S. Roux et al. on 2 million cells where the PVC is visualized using a low-pressure region [91]. Fig. 1.3 (right) shows one of the largest LES ever performed for a swirled flow in 2010, in the same geometry as Roux et al [91], but on a much finer mesh using 2.6 billion cells [76].

After a first period (until 2009) where LES seemed to deliver all expected results in swirlers, a few disturbing facts appeared: (1) despite the fact that the velocity fields produced by LES were accurate, the pressure losses through the swirlers were definitely not as good showing errors of the order of 30 to 100 percent and (2) LES results also seemed extremely

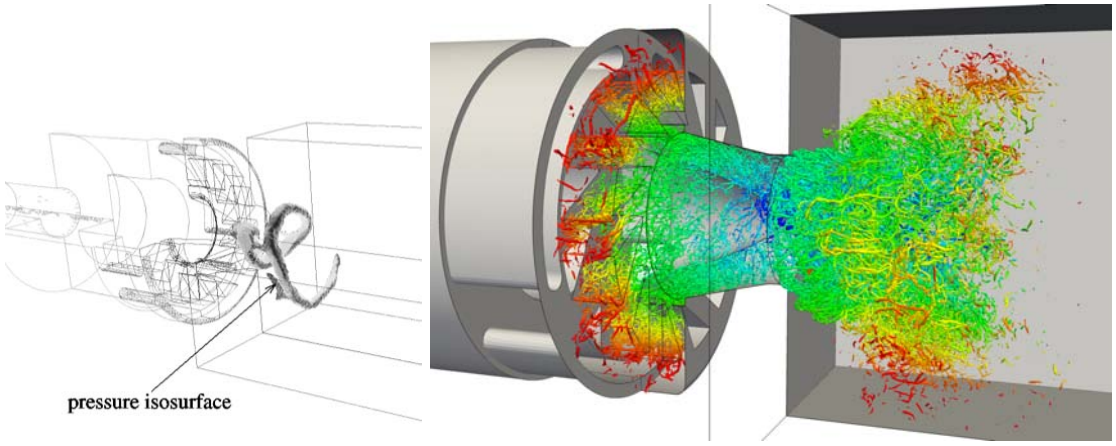

Figure 1.3: Examples of LES of swirled flows. Left: the LES of Roux et al [91]. Right: the LES of Moureau et al [76]

sensitive to parameters such as the SGS model or the boundary conditions. An additional difficulty arising with recent swirlers is that they use multiple passages while the injection system of Fig. 1.3 used in [91, 76] used a single swirling passage. For a single swirler, errors on pressure losses have no effect on the velocity field since the flow can use only one passage. As soon as a swirler with multiple passages is used, any error on pressure losses will directly impact the flow split between the passages, leading to significant flow variations. Finally, the impact of the mesh (quality and number of points) remains obviously a weak point for all LES where near-wall regions must be resolved and the impact of the wall model on the results is also certainly an issue in these swirlers.

The difficulties encountered to simulate swirling flows are less surprising when one considers the experimental literature on these flows [10, 32]. Experimentalists know that bifurcation is a common feature in many swirling flows where multiple instabilities take place. Even simple, academic flows shows multiple configurations: seven different types of vortex breakdown (vortex breakdown is the main structure of highly swirled flows) have been identified depending on the swirl and Reynolds number [23] and there are numerous borderline ranges for which two forms or more can exist and transform spontaneously into each other [64]. As a result, the combustion community today has clearly identified the fact that (1) swirl flows are important but pathological flows subject to violent bifurcations and that (2) even though LES seems to correctly capture these flows, as the output of LES codes depends strongly on external settings and modeling, the margin of reliability is low.

These observations share many common points with a more general field called UQ (Quantification of uncertainties) which has been growing rapidly in the CFD community in the last five years [65, 20]. Obviously, what the previous statements demonstrate is that swirling flows are highly dependent on multiple uncertain parameters and that since these flows are also submitted to bifurcations, these two phenomena (large UQ sensitivity and possible bifurcations) lead to a problem which becomes very difficult for simulation. We will not develop any element of the UQ methodology in the present work because we needed to identify which parameters are actually important before trying to vary them in a systematic fashion. At the present stage, there are too many important parameters

(mesh, SGS model, boundary conditions, inlet conditions, wall models, numerical dissipation) which affect the solution of swirling flow simulations in practical configurations to apply a UQ technique but we are aware that this will be the next logical step, once the controlling parameters will have been identified. A second reason why UQ was not used here is that we will be considering unsteady solutions and unsteady flows are still very difficult to handle with UQ tools.

1.2 Mesh adaptation, the way toward standardization

As underlined in section 1.1 and as will be shown in this thesis, simulating swirling flows presents major difficulties. Such difficulties have a trivial solution: resolving all turbulent length scales, which is also known as Direct Numerical Simulation (DNS). Despite the fact that computational power is constantly increasing (see Fig. 1.4) DNS is unaffordable at the present time for industrial configurations[2].

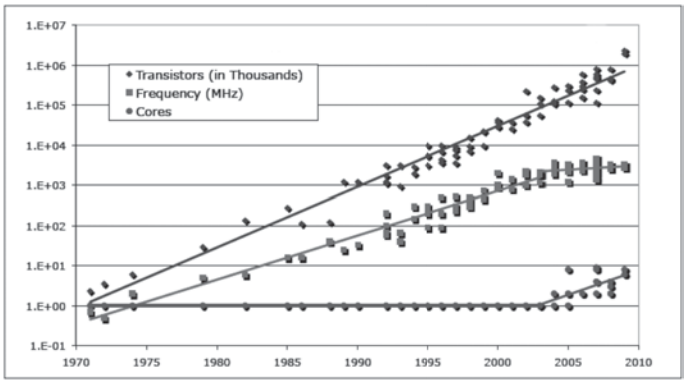

Figure 1.4: Frequency and number of transistors for CPU plotted against Moore s law from 1965 (continuos line on the top). A change occurred after year 2000, showing an increase of the number of cores per processor. From [55].

As a consequence of the cost of DNS in industrial configurations, LES is employed. LES requires modeling to close its formulation and modeling is, by construction, affected by the grid size. However, to choose the proper grid size presents some major difficulties because of the very wide range of length scales and phenomena involved in industrial flows. A very fine grid implies unaffordable numerical costs while a very coarse grid will lead to wrong predictions. A compromise solution between the two extrema, i.e. an homogeneous mesh as fine as possible but not as fine as a DNS mesh, does not represent the optimum solution: some turbulent length scales could be properly resolved in such grid, some others not. Since turbulent structures interact with each other in a non-linear manner, the outcome of such approximations is unknown and unpredictable a priori.
Non-homogeneous grids, which are used in most LES of industrial flows, represent a solution to take into account the different flow length scales. However, there is no general

[2]For instance, if only one of all simulations performed during this thesis would have employed a grid size in the order of the Kolmogorov length scales, i.e. $\Delta = O(\eta_k)$, such LES would have required 3.21×10^{11} CPU hours. (this approximation is obtained extrapolating the numerical cost of the LES performed) that makes, at a cost of 0.01 euro for CPU hour, a cost of 3 billions of euro in the best case scenario

criterion to design such grids. The mesh, which is the leading order parameter in LES, is most of the time created arbitrarily and its quality relies on the experience of the scientist (in the best case scenario) or of the first year phd student/engineer (as usually happens) who is generating it.
The most obvious solution to this problem is mesh convergence studies. However, such studies are not always affordable in industrial configurations since the numerical cost is usually pushed to its edge from the beginning. Since the scientific study of industrial flows is by default computing-time expensive, a factor 16 (which implies the use of a twice finer mesh) on its cost is most of the time unaffordable, especially when multiple configurations are tested. Also, the whole set of the flow statistics will never converge and the only option available is to hope low order statistics to converge with increasing mesh resolution [90], and that numerical and modeling errors do not compensate each other [72].
As a consequence, the most important LES parameter, the mesh, is chosen more or less arbitrarily. What should be the result of a scientific investigation (which requires standard parameters such as well established numerical methods, SGS models or boundary treatments), is often the outcome of an arbitrary choice made on the mesh. This disturbing truth contrasts a global trend, for instance in industry where it is becoming more and more common to certify (using international standards such as ISO9001 etc.) all procedures in order to ensure high quality standards.
For all these reasons, the second part of this thesis focuses on mesh adaptation, that is the ability of manipulating a grid based on a set of criteria. Mesh adaptation methods have been widely applied to improve mesh quality based on the mesh geometrical properties (which is also known as *a priori* adaptation) or coupled with a flow solver to adapt the mesh based on a given flow property (which is also known as *a posteriori* adaptation).
An example of *a priori* adaptation is shown in Fig. 1.5 which shows a basic mesh (left) with bad quality elements (highly stretched) which comes from two different domains and an adapted mesh (right) where such elements are replaced by more regular ones to obtain a smoother grid.

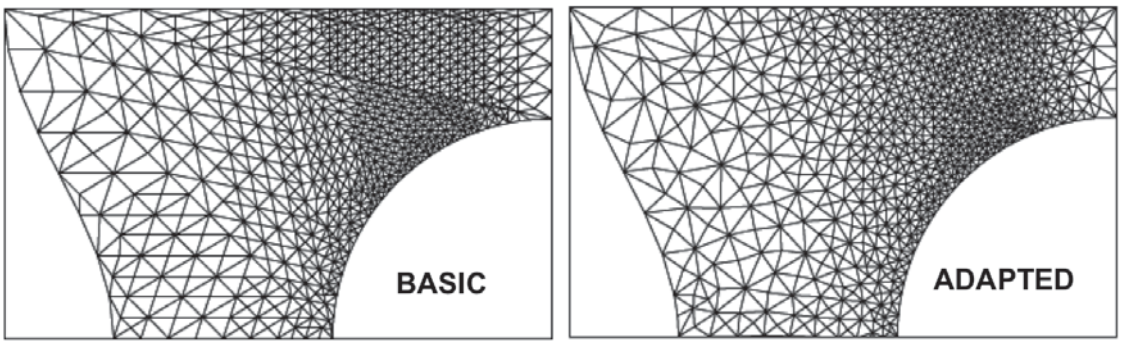

Figure 1.5: *A priori* mesh adaptation, from Freitag et al. [24]

An example of *a posteriori* mesh adaptation is shown in Fig. 1.6, in which the mesh is adapted to capture the shock interface (which is moving) caused by a blast: the grid resolution is increased where the shock is located, a type of refinement impossible to perform a priori (without knowing the shock location) or to be made by hand with a common commercial mesh generator.

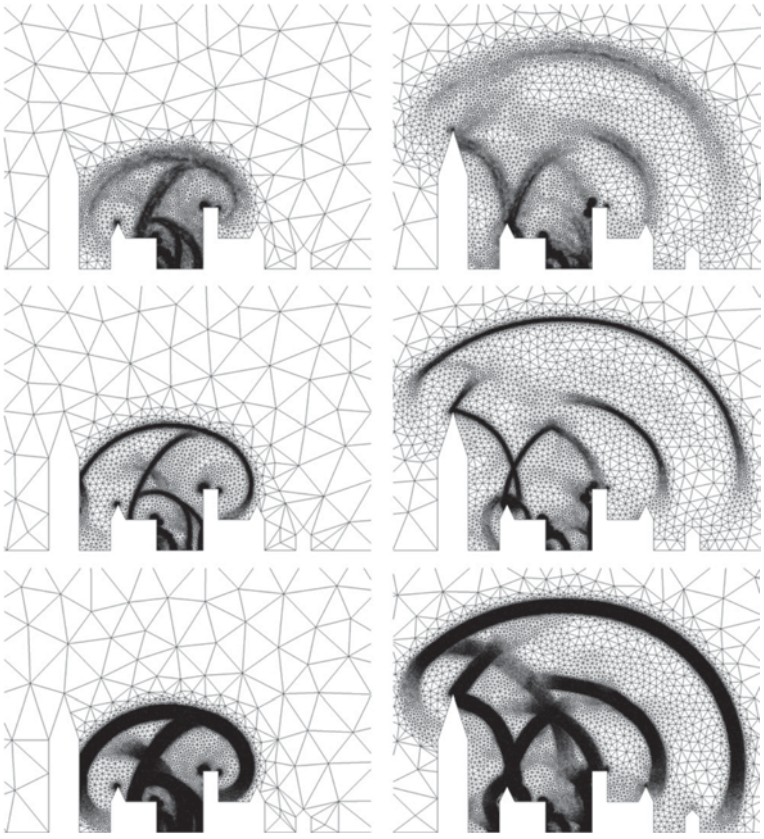

Figure 1.6: *A posteriori* mesh adaptation, from Alauzet et al. [3]. The mesh is adapted continuously in order to capture the moving shock wave caused by a blast (the different images corresponds to different instants).

Such mesh adaptation methods have been widely used in the context of the Euler equation (see for instance [25, 3, 2, 63]) while very few examples in LES can be found in the literature.
One example is the work of Hertel and Frohlich [37], who used a self-adaptive method executed in parallel to the LES solver. Mesh adaptation, obtained by nodes displacement, is included in the LES equations via the ALE (Arbitrary Lagrangian Eulerian) formulation. The results of such a method [37], tested on the flow over a periodic hill, showed (for a sensor based on the velocity gradient) a quality comparable to a highly-resolved LES many times bigger in terms of the number of nodes.
Here, a metric based mesh adaptation method will be used (the same as [25, 3, 2, 63]) coupled with simple, empirical criteria for adaptation. It will be shown that mesh adaptation can improve results while keeping the numerical cost of the simulation constant, therefore optimizing the simulation outcome, and making the meshing process a repeatable procedure.
A clear distinction must be made between standardization/repeatability and optimization.

- Standardization/repeatability is the ability to use the same adaptation method on different flows and configurations and allows to transform meshing from an handicraft process to an industrial process.

- Optimization is the ability of the adapted mesh to improve results and is a function of the particular criterion chosen for adaptation and of the flow which is simulated.

All mesh adaptation results presented in this thesis show improvements with respect to the original, arbitrary mesh used for comparison[3]. What makes them useful is the possibility to apply them to similar configurations in an automatic fashion, i.e. without relying strongly on the experience of the person who is using them. Of course, there is large margin of improvement in all of them, but thanks to the repeatability property of mesh adaptation, an optimal criterion for a given flow can be easily extended to all similar flows. Note that mesh adaptation has been applied to a very limited number of canonical LES studies [37, 38, 39] and has never been tested in complex, industrial configurations such as the aeronautical swirler studied in the first part of this thesis. This work can be considered as one of the first efforts in such direction and is the first step toward establishing such a mesh adaptation framework.

1.3 Plan of the work

This thesis is organized as follows:

- The first part (Chapters 2-3-4) discusses the difficulties encountered in simulating a confined, industrial swirling jet. Such difficulties will be related to natural phenomena, such as violent bifurcations and hysteresis, present in the flow and which are investigated on a very fine mesh in chapter 5.

- In the second part (Chapter 5-6-7-8) the fundamental of mesh adaptation are presented and tested in simple cases.

- In chapter 9 the first two parts merge. Mesh adaptation methods presented in part II are tested on the industrial configuration studied in part I. In this last chapter a mesh adaptation criterion will be presented which improves significantly the flow prediction in terms of velocity profiles and pressure drop and can be extended to other similar industrial configurations without tuning.

[3]Note that only simulations at the same numerical cost are compared.

Part I

Bifurcations & hysteresis in LES of swirling flows

Chapter 2

LES of swirling flows

The objective of the first part of this thesis is to study mechanisms which control the accuracy of LES when it is used to compute strongly swirled flows in a real, industrial configuration. Here the LOTAR experiment, a high Reynolds number flow using multiple swirling jets installed at ONERA Fauga for the KIAI European Program, is chosen but we expect results to be fairly general.
In order to study leading order simulation parameters, a sensitivity analysis is performed by changing:

- subgrid scale models: ranging from SIGMA [80], to Dynamic Smagorinsky [29],
- the mesh,

while keeping constant all fluid dynamics and thermodynamics conditions. All variations artificially induced by simulation settings will be then analyzed and linked to local modifications in the computed flow field. As swirl jets are subject to bifurcation, **LES results will show that such small modifications can trigger large flow reconfigurations**. The various numerical and physical parameters have the capacity to modify the results: small, local, variations can lead to global bifurcation phenomena if the flow is close to critical conditions. The most obvious example is artificial viscosity: a small amount of numerical viscosity can be enough to decrease the effective Reynolds number seen by the flow and lead to another regime; if the flow is very Reynolds sensitive, this small variation in numerical parameters may trigger a large change in the results.
LES results are compared to experimental data obtained at ONERA. It is known that the main drawback of such a posteriori testing is that it characterizes whole codes and not only single parameters [51]. To overcome this problem two completely different LES codes are tested on the same numerical mesh and settings: an incompressible LES code, YALES2 [76], and AVBP, a compressible LES solver [93, 92]. Using two codes allows to identify the effects of a single parameter variation by isolating spurious, hidden effects of the numerical procedure. The configurations are itemized in table 2.1. A complete span of the parameter space would have required an excessive number of simulations but this reduced set is sufficient to obtain conclusions at a reasonable cost. Sensitivity analysis is then performed in a limited way and the use of two codes has been limited to the most significant cases.

NAME OF RUN	MESH USED	CODE MODEL	SGS
AVBP-SIGMA	basic (14M cells)	AVBP	SIGMA
YALES-SIGMA	basic (14M cells)	YALES2	SIGMA
AVBP-DSMAG.	basic (14M cells)	AVBP	DYN. SMAG.
YALES-DSMAG.	basic (14M cells)	YALES2	DYN. SMAG.
YALES-DSMAG._O	optimized (15M cells)	YALES2	DYN. SMAG.
YALES-SIGMA_O	optimized (15M cells)	YALES2	SIGMA
AVBP-SIGMA_O	optimized (15M cells)	AVBP	SIGMA

Table 2.1: List of LES performed in Chapter 3.

After the main flow features for the various configurations of table 2.1 (i.e. flow split, swirl numbers and ratio) were obtained, a new experiment was performed on a simplified geometry extracted from the complete configuration (Fig. 2.1) to be able to change the swirl level continuously.

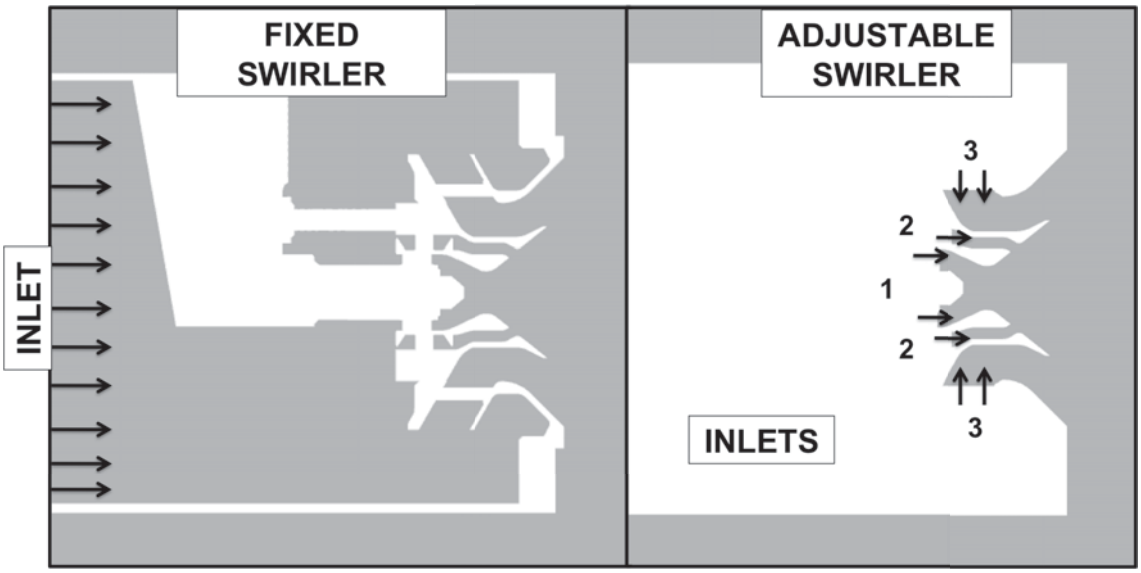

Figure 2.1: Fixed swirler, used for simulation in table 2.1, and adjustable swirler, used for the fluid dynamics analysis of chapter 4. Arrows represent inlet boundary conditions.

In this simplified domain, called adjustable swirler in Fig. 2.1 right, the inlet boundary condition has been shifted downstream at the exit of the swirler vanes in order to decouple the flow swirl and Reynolds numbers from the injector geometry: this geometry is therefore named adjustable swirler. Removing the small swirl passages, O(1) mm in size, present in the complete domain reduces the computational effort and resolution can be increased in the swirler bowls at a reasonable computational cost. It also allows to change the swirl level easily by changing the velocity angle on the boundary conditions 1-2-3 (Fig. 2.1 right), something that is more difficult in the full configuration (named therefore fixed swirler, Fig. 2.1) where any change of swirl would require a total change of the CAD/mesh.

In this second analysis numerical settings are kept constant while fluid dynamics conditions (which are controlled by swirl) are varied. Results agree with the first analysis, showing that a small variation of the leading order parameter (the swirl ratio) for a fixed geometry and Re, can cause a natural bifurcation. These numerical results are then compared to a similar study performed experimentally by Vanierschot and Van Den Bulck [105]. Even if the exact limits of the different states and the hysteresis patterns differ (as a consequence of the different geometries), both the present LES of an aeronautical swirler and the simpler configuration of Vanierschot et al. [105], exhibit similar bifurcations mainly controlled by the swirl level.

2.1 Organization

This first part of this thesis focuses on the simulation and the analysis of the swirled flow in the configurations of Fig. 2.1. It is organized as follows.

- **Chapter 2**

  In the following part of this chapter evidences of hysteresis, bifurcation and bistability in swirl flows will be given, based on the experimental literature on the subject. The main features of swirl flows, such as vortex breakdown and the Precessing Vortex Core (PVC), will be shown. A review of the state of the art of LES of industrial flow will be presented in order to clarify up-to-date requirements for such simulations and which level of complexity it has reached. The mathematical foundation of bifurcation will also be recalled briefly.

- **Chapter 3**

  In this chapter the LOTAR experiment of ONERA, the numerical setups used for AVBP and YALES2 and the characteristics of the SGS models and numerics used, will be clarified. The discussion of results will begin in Section 3.4 by presenting a baseline case where AVBP and YALES2 results are compared for a first mesh called *basic* (see Table 2.1). The two codes are using the same mesh and the same SGS model (SIGMA). Results are compared to experiment in terms of velocity fields and pressure losses: they show that the flow is badly predicted in both cases leading to a jet which expands too much and a level of accuracy very far from what usually observed in LES. The effect of the SGS model is discussed in Section 3.5 by replacing the SIGMA model by the Dynamic Smagorinsky model. Finally the effect of the mesh is determined using an *optimized* mesh (Section 3.7), which does not have significantly more cells (15 millions vs. 14 millions) but where nodes have been placed in critical zones, reducing the local mesh size where needed. Results show that the changes in the numerical settings can cause the flow solution to bifurcate leading to a jet which expands less rapidly and a comparison with experimental velocity fields which is much better.

- **Chapter 4**

  While chapter 3 shows evidences of bifurcation induced by numerical settings, chapter 4 proves that this strong non-linear response is due to the fact that the baseline case studied in LOTAR corresponds to a geometry and a swirl ratio (of the order of 0.8) close to critical conditions where a bifurcation takes place. For a fixed numerical setup, fluid dynamics conditions are varied in the configuration called adjustable thanks to a simplification (see Fig. 2.1) introduced in the geometry (which also allows to use a very fine mesh). Results confirm that the swirl ratio of the radial jet of LOTAR controls the flow states and allow to construct a bifurcation diagram where the flow state is determined by the swirl ratio and by the flow history.

2.2 General features of swirling flows

The aim of this section is to review the main features of free swirl flows and their different instabilities (Vortex breakdown, PVC, axial and azimuthal Kelvin-Helmholtz instabilities). Experimental evidences of bifurcation and hysteresis phenomena for confined swirling flows (such as the one that will be shown in chapter 3 and 4) will be presented and finally the mathematical basis of bifurcation will be exposed briefly.

2.2.1 Nondimensional parameters.

A swirling flow, or jet, is defined as one undergoing simultaneous axial and azimuthal motions. Swirl flows are characterized by the Reynolds number and the Swirl number S (or the swirl ratio S_r).
The Reynolds number is a measure of inertia force over viscous force and is used to characterize the transition from a laminar to a turbulent regime:

$$Re = \frac{U\ D}{\nu}, \tag{2.1}$$

where U and D are the characteristic speed and dimension of the flow respectively, while ν is the kinematic viscosity. Industrial flows are fully turbulent and swirling flows in combustors are usually built to be insensitive to small Reynolds number modifications to avoid transition between vortex breakdown type, as this could cause large variations in the recirculation and mixing zones [32].
The swirl number (S) is defined as the ratio of axial transport of angular momentum over axial transport of axial momentum: both are invariant for a jet in stagnant surroundings [32] (see also [83] for a rigorous derivation). There are several definitions in the literature of the swirl number that also include the axial thrust due to pressure difference and the Reynolds stresses representative of turbulence intensity. In this work these terms will not be included and the swirl number will be defined as:

$$S = \frac{\int_A \rho u_a u_\theta r dA}{R \int_A \rho u_a^2 dA} \tag{2.2}$$

where u_a is the axial velocity, ($u_\theta\ r$) is the angular momentum in the longitudinal direction, R is the characteristic radius of the jet[1]. When the swirl number is increased above a critical value $S \approx 0.6$ (that is an empirical criterion while Eq.(2.7) derives from analytical considerations) vortex breakdown is triggered.
In addition to the swirl number S, another non-dimensional number called swirl ratio (S_r) is also used in certain cases. The swirl ratio is defined as:

$$S_r = \frac{\int_A u_\theta dA}{\int_A u_a dA}. \tag{2.3}$$

[1]Since some of the flows here examined are made of multiple concentric and counter-rotating jets, R is chosen arbitrarily as the radius of the largest.

2.2.2 Main instabilities of free swirling flows

Experimentalists know that bifurcation is a common feature in many swirling flows where multiple instabilities take place [23]. The most common of them is vortex breakdown [10, 64], which occurs when reverse flow takes place along the jet axis [13]. As first proposed by Hall [35], vortex breakdown can be explained with the presence of an adverse pressure gradient induced by the conservation of circulation and the jet expansion [10]. The presence of azimuthal velocity (and therefore centrifugal force) induces a radial pressure gradient given by the simplified radial equilibrium relation (radial velocity is assumed to be zero):

$$\frac{dp}{dr} = \rho \frac{u_\theta^2}{r}. \tag{2.4}$$

For a stagnant fluid, the pressure field imposed by centrifugal force and local pressure (P_r) must balance pressure at infinity (P). As a consequence, the presence of a zone with a strongly rotating flow results in a local subpressure (P_d),

$$P_d = P \quad - P(r) = \int_0^r \rho \frac{u_\theta^2}{r} dr. \tag{2.5}$$

As the jet is spreading along the axial direction (x), the conservation of total circulation implies a decay of the tangential velocity and therefore a recover of $P(r)$ to P . As a consequence, the flow senses an adverse pressure gradient along the axial direction,

$$\frac{dP(r)}{dx} > 0. \tag{2.6}$$

Above given critical conditions (when the swirl is larger than a critical threshold, see Eq.(2.7)), axial momentum is first balanced and then overwhelmed by this secondary axial pressure gradient (Eq.(2.6)). The result is the creation of a recirculation zone: vortex breakdown is taking place.

As stated by Liang and Maxworthy [60], vortex breakdown is commonly associated with a finite transition between a super-critical upstream and sub-critical downstream states in an axisymmetric flow, as first proposed by Benjamin [9]. The location of breakdown can be predicted by the non-dissipative transition from a super-critical to a sub-critical flow [60]. Using the assumptions of Escudier et al. [22], Billiant et al. [10] developed a criterion ($C_{Billant}$ in Eq.(2.7)) for the appearance of the vortex breakdown as:

$$C_{Billant} = \frac{(\int_0^r \rho \frac{u_\theta^2}{r} dr)^{\frac{1}{2}}}{u_a} = \frac{1}{\overline{2}}, \tag{2.7}$$

which shows a very good comparison with experimental data [10, 60]. The Rankine vortex of Billiant et al. [10] (Fig. 2.2) is of particular interest since it is prone to hysteresis between different flow states (as the open cone shown in Fig. 2.2 or as a closed bubble) and flow states can appear randomly (as they lie in the same parameter space).

In general, seven different types of vortex breakdown have been identified depending on the Reynolds (Eq. 2.1) and swirl (Eq. 2.2) numbers [23] but there are numerous parameters ranges for which two forms (or more) can exist and transform spontaneously into each other [64]. The seven different types of vortex breakdown found by Faler and

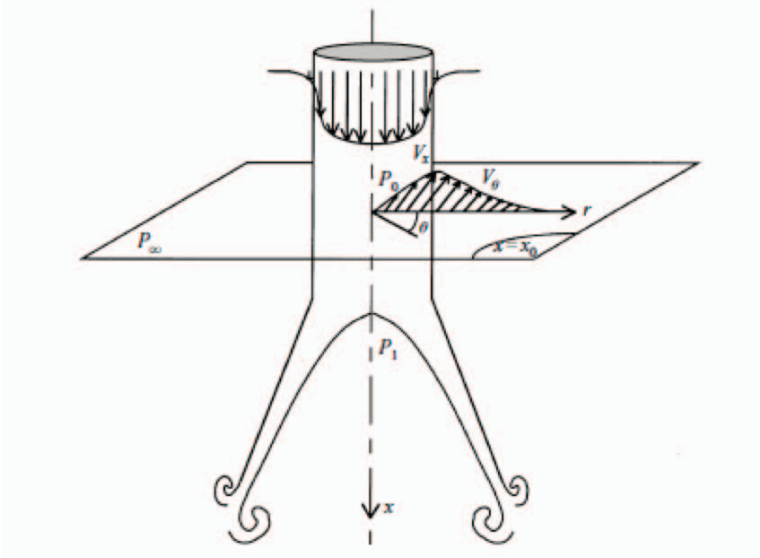

Figure 2.2: Cone vortex breakdown mode, from Billant et al. [10]

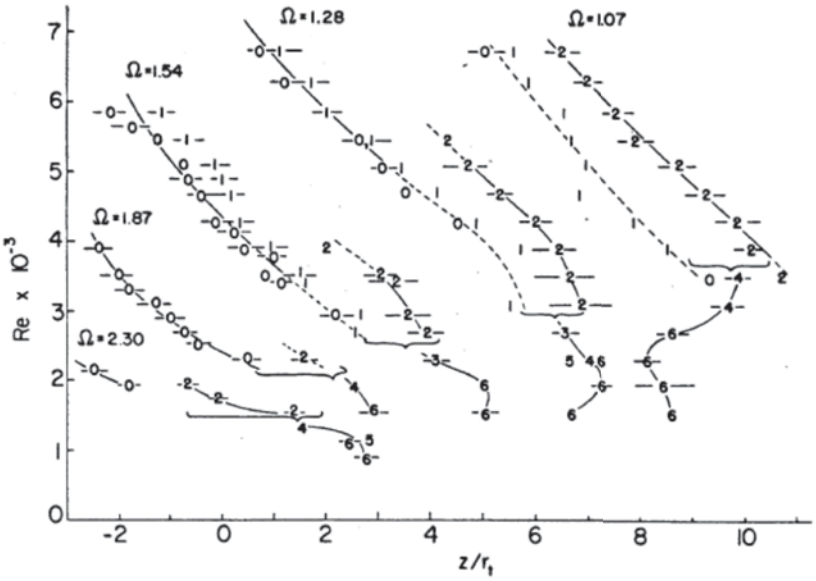

Figure 2.3: Vortex breakdown types (from zero to six) as a function of the Reynolds (in ordinate) and circulation number (in abscissa), from Faler and Leibovich [23]

Leibovich [23] are summarized in Fig. 2.3 where flow states are plotted in the Reynolds number (Re) - circulation number (Ω) space ($\Omega = \frac{\Gamma}{u_a D}$, with $\Gamma = 2\pi R_e u_\theta$).

Mode 3,4,5,6 in Fig. 2.3 are less commonly observed than the others and occur only for low Re, while at high Reynolds number the only characteristic forms are the bubble (Fig. 2.4(a)) and spiral (Fig. 2.4(b)) [64], respectively modes zero and two in Fig. 2.3 (while mode one is a slightly asymmetric bubble).

The bubble mode is characterized by a stagnation point on the swirl axis followed by an abrupt expansion of the centerline dye filament to form the envelope of a bubble of

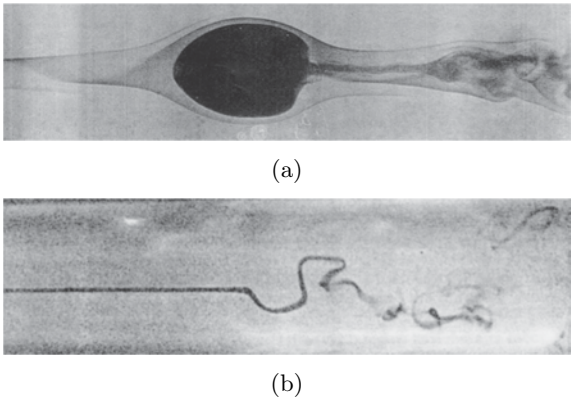

(a)

(b)

Figure 2.4: The bubble mode (a), from Sarpkaya [96], and the spiral mode (b), from Faler and Leibovich [23]

recirculating fluid [64] (Fig. 2.4(a)). The spiral mode is characterized by a rapid deceleration of the dye filament marking the swirl axis which causes stagnation and by an abrupt kink followed by a corkscrew-shaped twisting of the dye [64] (Fig. 2.4(b)). The spiral mode is associated to the instability of the bubble: the development of disturbances in the flow is responsible for the appearance of a breakdown dominated by spiral waves [60]. However, this two-modes classification (bubble-spiral) is by no means certain and is open to further interpretation [60]. Discharge orifice geometry [32] as well as adverse pressure gradient, [96] (i.e. generated by a divergent nozzle) can modify the features of swirl flows; in general the overall pressure and velocity fields are important as they are interrelated [34].

A clear example of the large sensitivity of swirling flows to small variations in the flow fields is the delta wing of Lambourne [59] (Fig. 2.5) in which each side of the wing shows different breakdown types at the same time (so, in a first approximation if the flow is axisymmetric, under the same fluid dynamics conditions). Even though it is a physically complex mechanism, vortex breakdown is also a desirable property of high swirl flows as the vast majority of gas turbine systems employ it to provide flame stabilization [43].

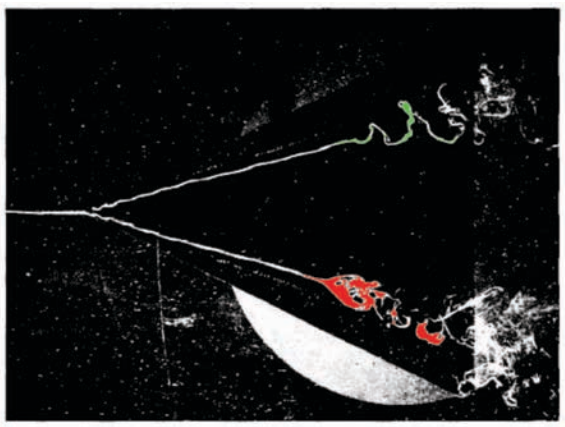

Figure 2.5: Delta wing of Lambourne [59]: upper side, spiral breakdown mode, bottom size, bubble mode. The picture has been colored.

A second important instability of swirling flows is PVC (Fig. 2.6): after vortex breakdown has occurred, the central forced vortex region of the flow can become unstable and start to precess about the axis of symmetry [64]. The frequency of the PVC can be characterized by the Strouhal number (which is a weak function of the Reynolds number) and by the swirl number [102]. However, its frequency and shape remain a function of the particular burner/swirler flow system configuration [102].

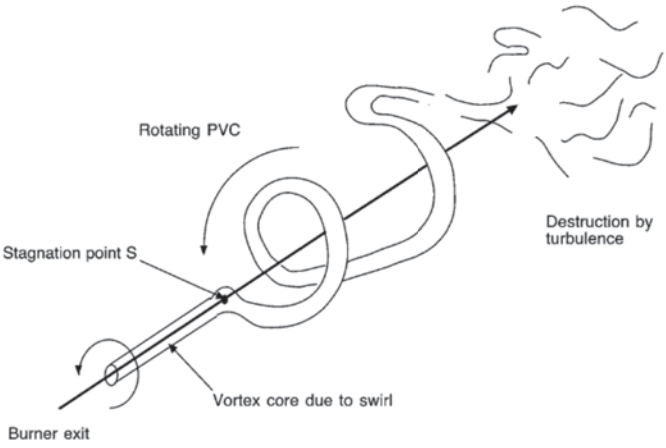

Figure 2.6: Schematic view of the PVC, from Selle et al. [100].

The PVC can be useful or detrimental for the engine performance, since, as stated by Huang [43], the PVC may improve combustion efficiency through its enhancement of turbulence intensity and mixing, but it also represents a largely undesired characteristic because of the possible resonant coupling with low frequency acoustic oscillation in the gas turbine combustor .
Finally, two types of Kelvin-Helmholtz instabilities, related to the presence of an axial shear layer (which eventually degenerate in an external PVC, as shown by Villalba et al. [28]) and an azimuthal shear layer (which give birth to the helical instabilities shown in Fig. 2.7 which are related to a stratification of the angular momentum along the radial direction [60]) can be present in swirling flows depending on the swirl level and the jet configuration.

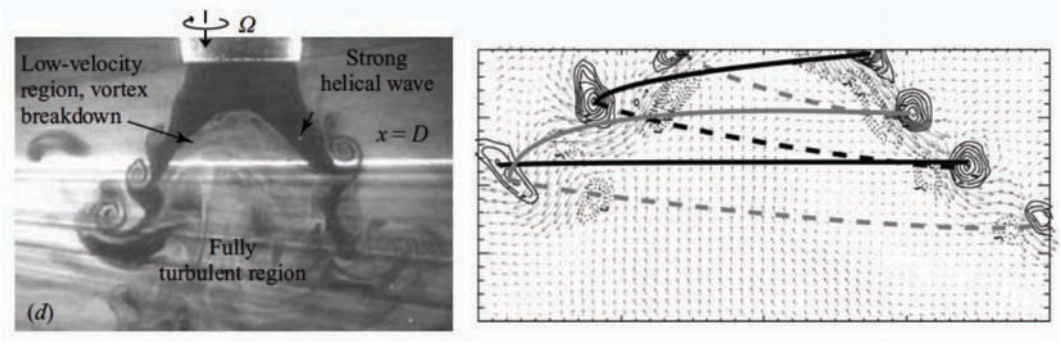

Figure 2.7: From Liang and Maxworthy [60], (left) picture of the free swirling jet and (right) a couple of vortex spirals (helical instabilities).

2.2.3 Bifurcation & hysteresis in confined swirling flows.

This section discusses flow states which can appear in confined swirling flows because of the proximity of solid boundaries. Without confinement walls, after vortex breakdown has occurred, the jet opening half-angle (α, expressed in degrees) varies linearly with the swirl number of the jet [32] as:

$$\alpha = 4.8 + 14 \;\; S. \tag{2.8}$$

Eq.(2.8) is obtained by regression of experimental data. One can imagine this condition as if a solid body is forced to rotate around an axis by a spring. As the solid body gets closer to the axis of rotation, centrifugal force ($F_c = \frac{\rho u_\theta^2}{r}$) gets higher and pushes it radially; moving away from the axis, centrifugal force weakens and the solid body is re-called by the spring. The resulting jet opening angle (in a first approximation) is linearly dependent on the introduced angular momentum (considering a constant streamwise velocity) as the radial position of the solid body would be in the system spring-rotating body.
Above a critical swirl strength (which is configuration dependent), confinement walls alter the expansion angle of the jet, which can attach to the sidewalls and behave like a radial jet, a phenomenon similar to the Coanda effect [32]. The Coanda effect is the tendency of a jet stream to adhere to a wall. Using the words of the first European colloquium on the subject (1965), the Coanda effect is the rather spectacular phenomenon which can be observed by holding a finger against a jet of water running out of a tap: the jet will adhere to some extent to the finger and be deflected [112].
The critical swirl number at which this transition takes place is dependent on the nozzle geometry: in Chedaille et al. [46], three different swirling jet configurations appear depending on the nozzle opening angle or on the expansion rate of the divergent nozzle. Similar jet configurations and recirculation zones are reported by Beer and Chigier [8], in a qualitative manner and more recently by Vanierschot and Van Den Bulck [105]. The experiment of Vanierschot et al. [105] (whose geometry is shown in Fig. 2.8) provides a quantitative analysis of a flow with variable swirl and will be used here as a reference example to classify flow states.

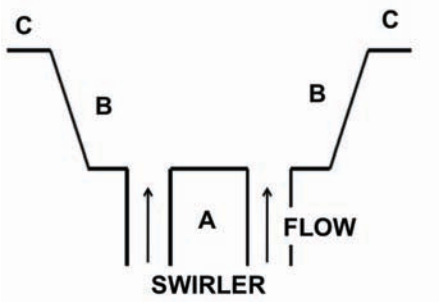

Figure 2.8: Geometry (nozzle) of Vanierschot and Van Den Bulck, [105]. A: central rod, B: nozzle walls, C: side walls. The swirler is upstream while arrows indicate the flow.

Vanierschot et al. [105], investigated the influence of swirl (Eq. 2.2) on an annular jet with a stepped-conical expansion (Fig. 2.8) at $Re = 11000$, identifying four, distinct flow states. The first two states identified by Vanierschot et al. [105], are named here, Unbroken axial jet (UJ) and free Axial Jet (AJ) (Fig.2.9). UJ states are obtained when $S < 0.4$ while AJ states appear for $S \geq 0.4$. At $S = 0.4$, vortex breakdown takes place

in this configuration. The transition between the Axial Jet and the Weak axial Jet (WJ), as named here, and the transition between the WJ and the Blasted Breakdown jet (BB), as named here, take place as follows (Fig. 2.10).

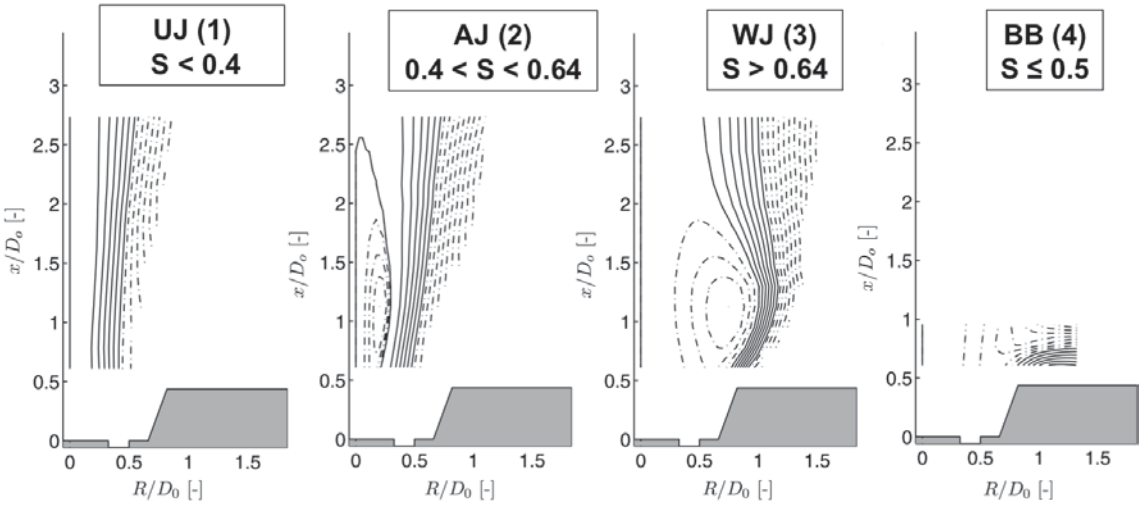

Figure 2.9: Experimental results of Vanierschot and Van Den Bulck, [105]: streamlines for four different flow states. Solid lines correspond to the jet boundaries and dashed-dotted lines are recirculation zones. Swirl number exact values are from left to right: $S = 0.335, 0.56, 0.69, 0.5$.

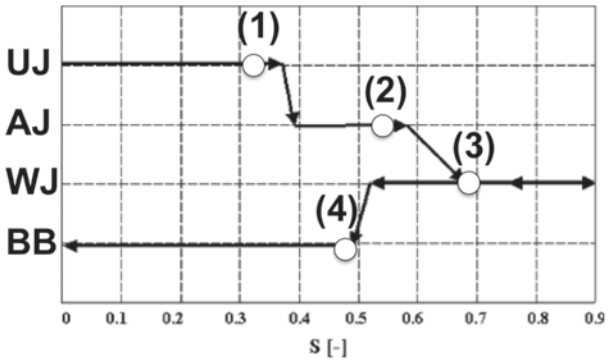

Figure 2.10: Transition map of Vanierschot and Van Den Bulck, [105]. The different flow states are plotted against the swirl number S. The four states of Fig. 2.9 (1 to 4) are added on the diagram.

First, increasing the swirl number up, from state AJ, to the second critical threshold of $S = 0.6$, the flow bifurcates to the WJ state. This bifurcation is characterized by an abrupt expansion of the Central Toroidal Recirculation Zone (CTRZ) which doubles its diameter (Fig. 2.9 & Fig. 2.11(a)). At the same time, the azimuthal velocity (Fig. 2.11(b)), turbulence levels (Fig. 2.11(c)) and the sub-pressure (Fig. 2.11(d)) in the CTRZ, decrease. The transition AJ-WJ is due to the appearance of a vortical structure close to the diffuser walls, named *Corner Recirculation Zone* (CRZ) in [107]. This structure is generated by the interaction of the jet shear layer, which, as the swirl number increases, gets closer to the solid boundary, and the inclined diffuser walls. Because of hysteresis, the WJ state remains stable even when swirl is decreased back to values which are lower than the transition point AJ-WJ ($S = 0.6$). At $S = 0.5$ (transition WJ-BB), a third bifurcation

takes place: the recirculation zone widens even more (its eye has disappeared from Fig. 2.9 & Fig. 2.11(a)); sub-pressure (Fig. 2.11(d)), tangential velocity (Fig. 2.11(b)) and turbulent intensity (Fig. 2.11(c)) drop to zero close to the flow centerline (where the vortex breakdown, in the WJ state, is located). Subpressure, or pressure deficit, is defined as:

$$P_D = (P_{atm} - P)/(0.5\ U_0^2\ \rho), \tag{2.9}$$

where P_{atm} is the far field atmospheric pressure, P is the local pressure, while $0.5\ U_0^2\ \rho$ is the kinetic energy of the jet[2]. In Vanierschot et al. [108] this counter-intuitive behavior (an expanding CTRZ with a decreasing swirl) is explained with a pressure balance between the CTRZ and the surroundings. In the author s opinion, this transition has to be explained with the CRZ dynamics (as for example explained in Vanierschot et al. [107] which seems to be in contradiction with itself [108]) and with the flow field close to the discharge orifice. However, the present work will not focus on this controversial and geometry dependent aspect. The characteristics of the three flow states of interest for the current study are summarized in table 2.2: after each transition (AJ-WJ-BB) CTRZ expands, tangential velocity and subpressure (which are inter-related) diminish, turbulence intensity reduces. For a swirl number of 0.3, for example, two very different states (UJ and BB) can be obtained (Fig. 2.10).

flow state	CTRZ size	normalized subpressure	CTRZ tangential velocity	CTRZ Reynolds Stresses
AJ	$R_v < 0.5$	$1.4 < P_D < 0.8$	high	high
WJ	$0.5 < R_v < 1$	$P_D < 0.4$	moderate	moderate
BB	$R_v >> 1$	$P_D = 0$	zero	zero

Table 2.2: Summary of the characteristics of the three different states (AJ-WJ-BB) documented in [105] after vortex breakdown. R_v indicates the approximate radial position of the eye of the CTRZ.

As mentioned before, similar results are present in the literature but no quantitative characterization of the flow (such as RMS profiles) are available. Fig. 2.12 shows the flow patterns described by Beer and Chigier [8] for a divergent nozzle (the figure is extracted from [83]). The swirl number increases from the flow of type A to type C. The type A flow, using the nomenclature used to classify [105], is a UJ, the type B is an AJ and the type C looks like a BB: no WJ was documented in [8].

Finally Fig. 2.13 shows the flow states documented in Chedaille et al. [46]. The flow configuration named B in Fig. 2.13 corresponds to an AJ state while configurations B and C are more difficult to classify. Flows B and C show a recirculation zone which is open-ended and the annular character of the flow is preserved for the entire length of the chamber [46]. Also, the internal reverse flow is weak and the static pressure throughout the whole recirculation zone is close to atmospheric [46] (see the WJ and BB states of table 2.2). States B and C appear depending on the nozzle geometry.

[2]Pressure deficit is usually measured inside the recirculation zone where it is minimum. Therefore, the subpressure characterizes the strength of the recirculating flow.

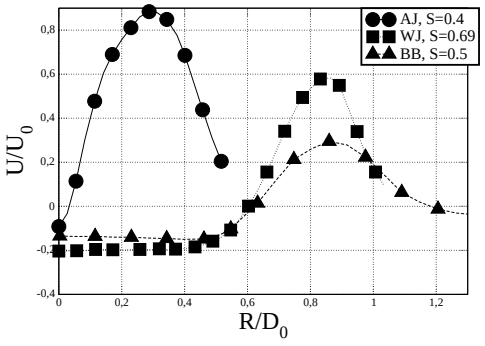

(a) Axial speed.

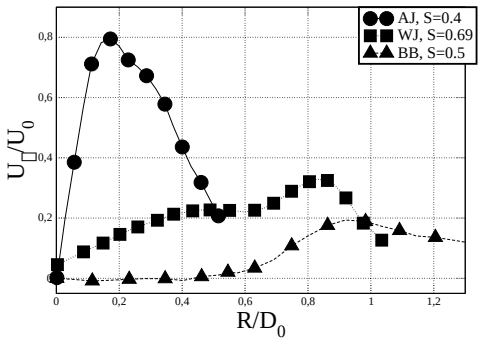

(b) Tangential speed.

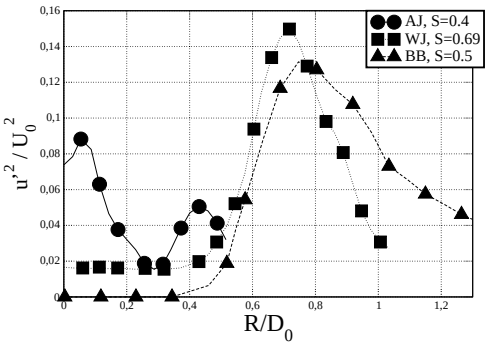

(c) Axial Reynolds stresses.

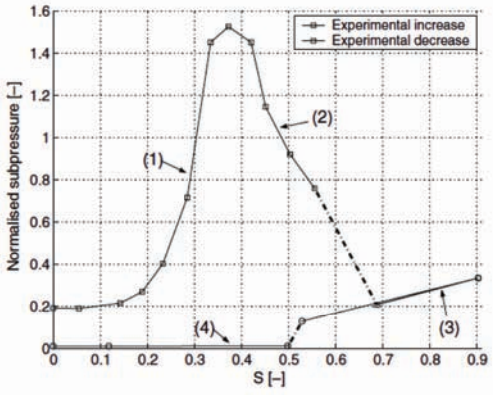

(d) Normalized subpressure.

Figure 2.11: (a)-(b)-(c) Flow measurement at an axial position of $x/D = 0.61$ plotted against the swirl number S, for the AJ, WJ and BB states. (d) Normalized subpressure ($P_D = \frac{P_{atm}-P}{0.5\rho U_0^2}$) where P is measured $3[mm]$ downstream of the injector orifice plotted against the swirl number S (rearranged from [105]).

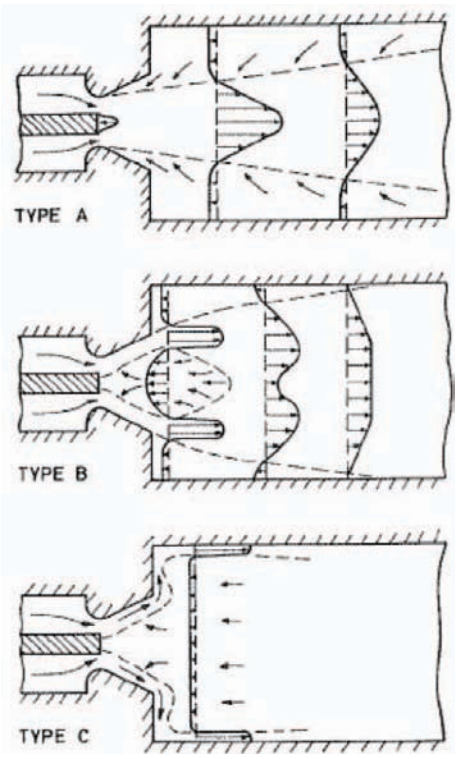

(a)

Figure 2.12: From[83] (rearranged from [8]): flow states issuing from a divergent nozzle, swirl intensity increases from type A to type C flows. Flow states show characteristics similar to Vanierschot et al.[105] (Fig. 2.9).

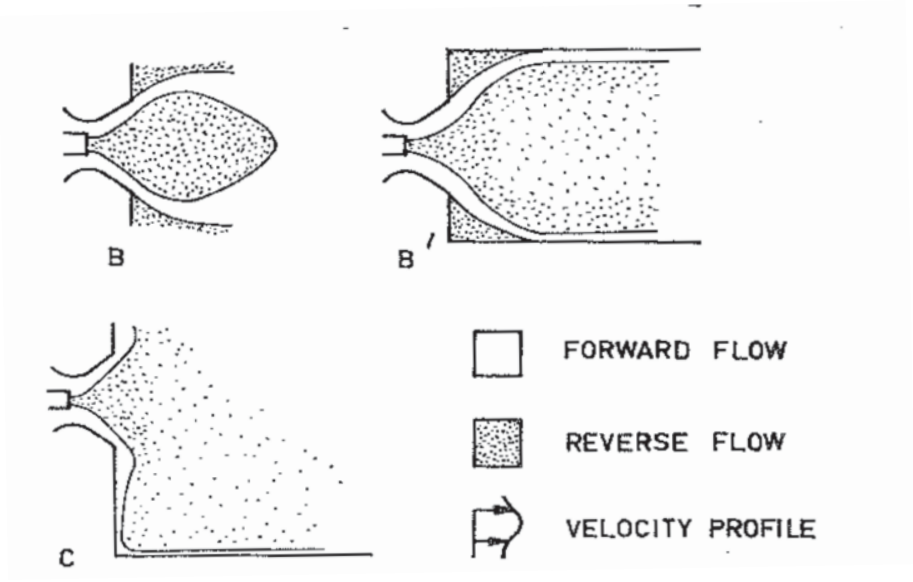

Figure 2.13: From[46] Flow states show characteristics similar to Vanierschot et al.[105] (Fig. 2.9).

2.3 Mathematical definition of bifurcation

This section, extracted from the book of Y.A. Kuznetsov Elements of Applied Bifurcation Theory [57], gives a very brief overview of dynamical systems and of bifurcation. A mathematically rigorous analysis of the phenomena described in this thesis would be too complicated because of the flow configuration complexity (such analytical efforts are commonly focused on much simpler-configuration, free swirling flows [60, 61]; already such type of canonical problems require complex analytical solutions).
A dynamical system is the mathematical formalization of the general scientific concept of a deterministic process [57]. The future and past states of many physical, economical, chemical systems can be predicted knowing their present state and the laws (φ^t) governing their evolution [57]. A dynamical system is defined as:

Definition 1 *A dynamical system is a triple* T, X, φ^t *where* T *is a time set,* X *is a state space and* φ^t *is a family of evolution operators parametrized by* t T *and satisfying* $\varphi^0 x = x$ *and* $\varphi^{t+s} x = \varphi^t(\varphi^s x)$

The properties of a dynamical system can be represented using geometrical images. The basic geometrical objects associated with a dynamical system T, x, φ^t are its orbits in the state space ($Orbit(x_0) =$ x $X : x = \varphi^t x_0,$ t T such that $\varphi^t x_0$ is defined) and the phase portraits composed of these orbits. Orbits in continuous-time system with continuous evolution operator are curves in the state space X parametrized by the time t and oriented by its direction of increase (see Fig. 2.14). A phase portrait of a continuous-time dynamical system could be interpreted as an image of the flow of some fluid, where the orbits show the path of the fluid particles as they follow the current [57]. All possible orbits can be classified into equilibrium points (x^0 is an equilibrium point if x^0 X $\varphi^t x^0 = x^0$ t T), cycles (see later for the definition of a periodic cycle) and all others [57].
Dynamical system can depend on parameters. Let us take a dynamical system of such type, in the continuous-time case it can be written as:

$$x = f(x, \alpha), \tag{2.10}$$

where x $\mathbb{R}$ and α $\mathbb{R}^m$ represent phase variables and parameters respectively. As the parameters vary, the phase portrait (the flow field) also varies. There are two possibilities: **either the system remains topologically equivalent to the original one**[3], **or its topology changes**. This is taken as the definition of a bifurcation:

Definition 2 *The appearance of a topologically nonequivalent phase portrait under variation of parameters is called a* ***bifurcation****.*

Thus a bifurcation is a change of the topological type of the system as its parameters pass through a *bifurcation (critical) value*. In order to clarify this definition, an example of

[3]"Two topologically equivalent systems have the same number of equilibria and cycles of the same stability types. Formally two systems are topologically equivalent if there is an homeomorphis (an invertible map such that both the map and its inverse are continuous) mapping the orbits of the first system onto orbits of the second system preserving the direction of time" [57].

bifurcation is given. Consider a planar system in polar coordinates ($\rho = radius, \theta = angle$) as:

$$\begin{cases} \rho = \rho(\alpha - \rho^2), \\ \theta = 1. \end{cases} \tag{2.11}$$

Since α and θ are independent in Eq.(2.11), it is possible to easily draw phase portraits of the system in a fixed neighborhood of the origin (Fig. 2.14).

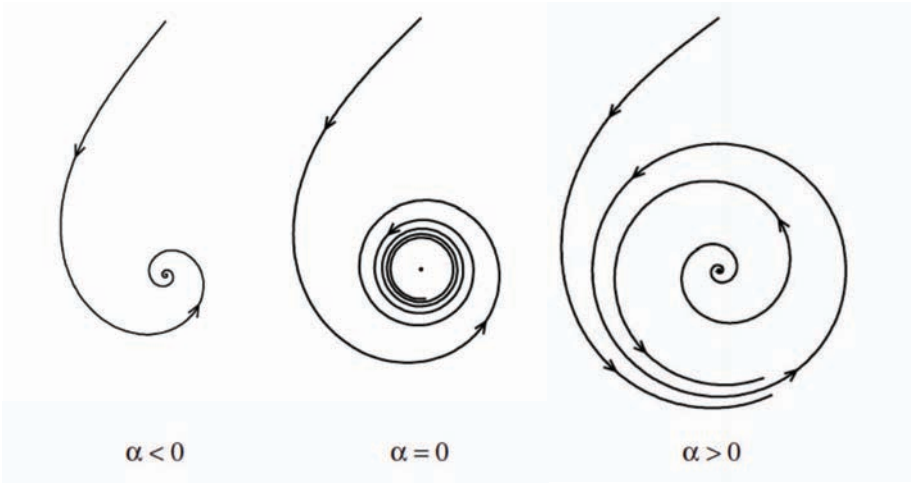

Figure 2.14: From [57], phase portraits of an Hopf bifurcation.

For $\alpha < 0$ the equilibrium is a stable focus (for which perturbations decay oscillatorily, the system always falls to $\rho = 0$), since $\rho < 0$ and $\rho(t)$ 0 if we start from any initial point. On the other hand, if $\alpha \geq 0$ it is easy to see that the system has a periodic orbit at $\rho_0 = \overline{\alpha}$ (a periodic orbit L_0 is defined as: $\varphi^{t+T_0}x_0 = \varphi^t x_0 \quad x_0 \quad L_0$ with some $T_0 > 0$) and this periodic orbit is stable since $\rho > 0$ if $\rho < \rho_0$ and $\rho < 0$ if $\rho > \rho_0$. Therefore $\alpha = 0$ is a bifurcation parameter value since the topology of the system varies (compare the phase portraits of Fig. 2.14 for $\alpha < 0$ and $\alpha \geq 0$). This type of bifurcation is called the *Andronov-Hopf bifurcation*.
Swirl flows are subject to bifurcations, for instance the one shown in Liang and Maxworthy [60] is likely to be of the Andronov-Hopf type. Even turbulence can be explained with the evolution of a dynamical system. As stated by Jimenez [50], one of the surprising discoveries of the last fifty years has been that deterministic systems with relatively few degrees of freedom can behave in very complex ways, and that as soon as the topological restriction of two-dimensional systems is removed (the system of Eq.(2.11) is two-dimensional), the generic behavior of an arbitrary system is to be chaotic . The key property of chaotic system is their sensitivity to initial conditions: two orbits with initial conditions which differs only by a small amount diverge exponentially and soon become completely de-correlated [50], as happens to flow particles in turbulent flows.

2.4 LES of realistic swirl injectors: state of the art

This section is dedicated to a brief review of LES of aeronautical swirling flows, results are analyzed with a particular focus on the similarities/differences with the LOTAR injector

that will be shown on chapters 3 & 4, and on useful tips in terms of numerics and mesh requirements. Swirl motion is usually generated in aeronautical engines by a swirler; the swirler is commonly mounted at the entry of the combustion chamber as vortex breakdown is used to stabilize the flame, to help ignition by the transport of burnt gases at the fuel injection point and to improve mixing via higher turbulence levels. Fig. 2.4 shows an example of such devices.

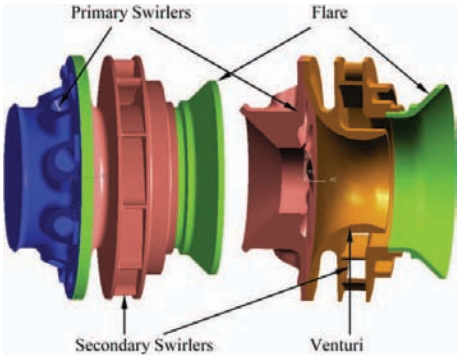

Figure 2.15: Swirler of Wang et al.[111].

The swirler of Fig. 2.4 consists of eight counter-clockwise elliptical primary jets and ten clockwise secondary vanes, a venturi section and a flare and it was numerically studied by Wang et al. [111] using a compressible LES solver (finite differences on a fully structured grid, 2^{nd} order accurate in space and time, employing static and dynamic [29] Smagorinsky SGS models and the Van Driest dumping function near the walls). The computational domain of Wang et al. [111] was restricted to the swirler and the downstream chamber, inlet boundary conditions were imposed inside the swirler vanes using average values obtained by a RANS simulation (a similar exercise will be done in this thesis in chapter 4). The typical flow structures of high swirl confined flows are present in this configuration: a Precessing Vortex Core (PVC), Central Toroidal Recirculation Zone (CTRZ) and Corner Recirculation Zones (CRZ) at the periphery of the chamber; proper-orthogonal-decomposition (POD) analysis reveals that the PVC is dictating flow dynamics, while standing acoustic waves play a minor role. A similar study was repeated by the same authors (Wang and Yang [109, 110]) for a twin-swirler injector. This study [109, 110] focuses on the different flow instabilities and their interaction for different swirl numbers and in forcing conditions and it can be used as a source of inspiration for a further analysis of the swirler studied here.
A realistic, complex Pratt & Whitney combustor (only a portion of the whole device), with a swirl injector device is the simulation domain of Moin and Apte [74]. Due to the complexity of the geometry, domain is triangulated via irregular polyhedra (hybrid mesh with tetrahedra, prisms, pyramids) and a compressible LES formulation equations is performed using an energy conserving, finite volume, numerical algorithm [67].

A specific aspect of this paper is the numerical scheme employed (energy conserving). Numerical dissipation has been shown to be detrimental in accurate prediction of turbulent flows, for instance in Mittal et al. [73] an up-wind biased high-order numerical methods is compared with a lower order central difference numerical scheme on flow past a cylinder at Re=3900: numerical dissipation inherent in the up-wind scheme removes substantial

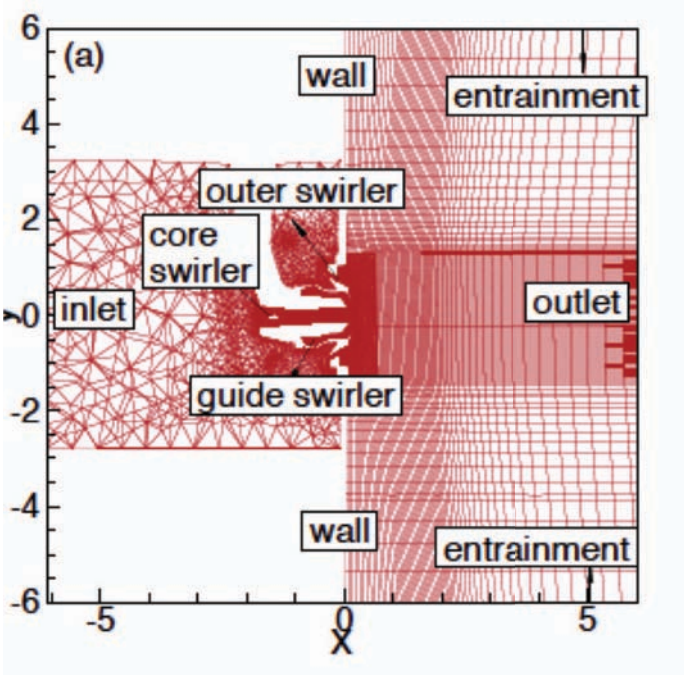

Figure 2.16: Pratt & Whitney combustor of Moin et al. [74]

energy from roughly three quarters of the resolved wave number range, while the non-dissipative, lower order central scheme shows much better agreement with experimental energy spectrum. The impact of the numerical scheme is clarified in Mahesh et al. [67]. The numerical algorithm is a kinetic energy conserving finite volume scheme with no artificial viscosity. Energy conservation assures that numerical instabilities due to non-dissipative central difference schemes remain bounded. With such a scheme a fully non-dissipative (switching off SGS modeling) HIT (Homogeneous Isotropic Turbulence) simulation at $Re = O(10^9)$ is obtained without any dissipation of kinetic energy (for such a Re, viscous scales lies outside the grid spacing and kinetic energy is transferred from the largest scale to smallest and remains there because, in absence of an eddy viscosity model, it can only be dissipated by laminar viscosity).

It is important to note that the criterion of kinetic energy conserving schemes is not globally accepted by the LES community. Many finite differences schemes and hybrid schemes [77, 93] do not try to conserve kinetic energy, as for a compressible flow it is not conserved. Moreover tests show that a 3^{rd} or 4^{th} order scheme (as the one used in the present work) which does not conserve kinetic energy still offers much better precision than a second order scheme conserving kinetic energy on simple tests such as the conservation of vorticity. Focusing on swirling flows, numerical dissipation gives a faster decay to swirl velocities and this has an impact on length of the recirculation region [104].

Swirl injectors are everyday bread of CERFACS researchers and some of their results will be summarized below. One of the classical applications of LES is to couple it with an acoustic solver [68, 91, 100]. LES is used to extract unsteady flame response to resolved acoustic oscillations (heat release). The obtained Flame Transfer Function (FTF) is fed to the acoustic solver, flame/acoustics interaction are then studied in order to optimize

combustion chamber design. In Selle et al. [100] this coupled LES- Helmoltz solver is performed on the geometry of Fig. 2.17.

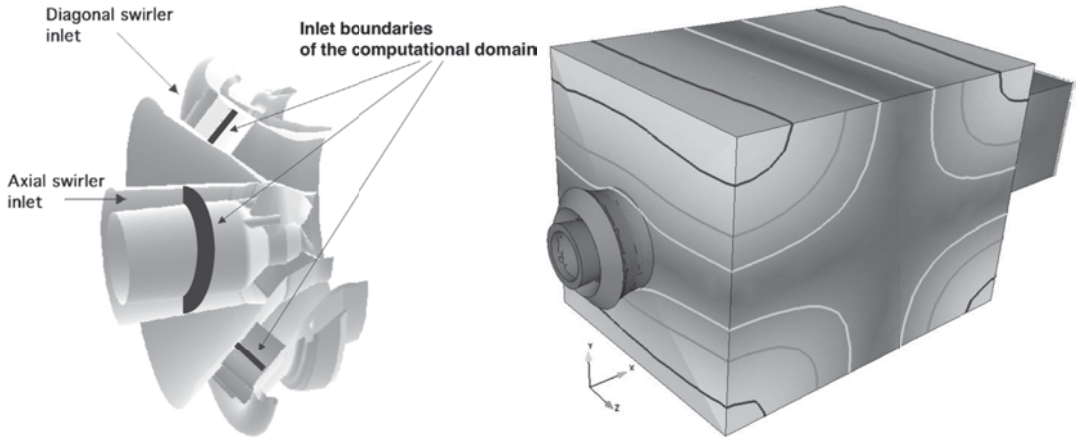

(a) (b)

Figure 2.17: (a)Injector of and (b) pressure fluctuation modulo if on e transverse mode calculated by the Helmoltz solver from [100]

Results of Selle et al. [100] show that the flow field in the reacting configuration is dominated by a PVC at a Strouhal number $St = 0.62$ (typical of these swirl flows, see section 4.6.2), while the reacting case is fully dominated by acoustics and the PVC is not observed. Similar results were obtained recently by Oberleithner et al. [81] which shows how non-uniform density suppresses the PVC. A similar numerical experiment is repeated in Roux et al. [91], where the computational domain is enlarged in order to reduce BCs effects (which are placed inside the vanes in [100], see Fig. 2.17). A phenomenon similar to [100] is again experienced: cold flow is hydrodynamically dominated by a PVC (no acoustics eigenmodes around its frequency are identified) while reacting case is dominated by acoustics. Combustion, dilatation and increased viscosity induced in the burnt gases seem to damp the PVC, while the flame acts as a strong acoustic energy source. As for [100], LES prediction matches experimental data without tuning BCs.

A non-reacting, two-phase flow staged, injector was simulated by Sanjose et al. [95] and Jaegle et al. [48] (Fig. 2.18). The swirler design is basically the same as LOTAR and the injector is a good example of recent staged architectures: three counter-rotating jets are generated by a series of three different swirl vanes. Flow split in this configuration is 90% through the radial swirler (while for LOTAR is $\approx 86\%$) and 10% in the two co-axial swirlers but no comparison with the experimental permeability measurements is available. Results showed a good comparison with experimental data for the axial and the tangential velocity components for both single and multiphase approaches, while the radial velocity component is not shown.
To summarize the non exhaustive survey given in this section, several issues in simulating swirl flows of real injectors have been identified. The first limitation of real life LES is related to the grid used to discretize the domain: while structured grids can be generated to discretize simple geometries, their use is almost impossible when the level of geometrical detail is increased. Structured meshes are put aside and unstructured meshes within

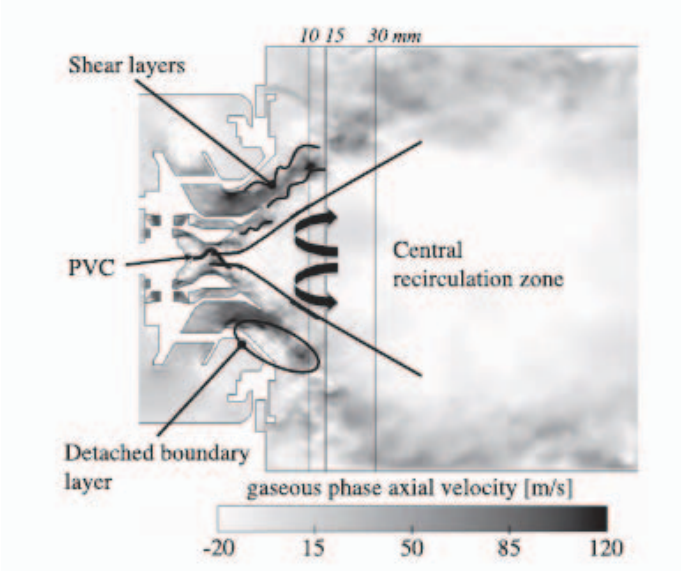

Figure 2.18: domain and flow structures of [48]

elements of any shape must be deployed; at the present time commercial programs are able to generate such unstructured meshes using tetrahedral elements, fast and accurately. Unstructured meshes imply that finite differences, so in general higher-order schemes, such as six or eight-order accurate, cannot be employed. Variational methods, such as Finite Volumes or Finite Elements must be used.

As for higher-order methods, it is difficult to perform explicit filtering LES on unstructured meshes. At the present time explicit filters have been used only on academic cases [12, 66, 30] and implicit filtering in LES is often the only practical solution for complex geometries (despite the numerical corruption of the highest wave number [31, 16]). However, from the theoretical point of view, implicit filtering in LES cannot be strictly derived from the Navier Stokes equations if the filter is not homogeneous in space [66]; from a more practical point of view, to define filter size (which determines the magnitude of the modeled term in LES) on highly anisotropic grids is an open research issue [98, 97]. Finally a properly resolved LES everywhere in the flow field is an expensive task, modeling is necessary and therefore remains a central issue; in particular cases, such as LOTAR, it will be shown that LES modeling can trigger strong variations in the simulated flow field. These three main issues, which impact accuracy for a single-phase, non-reacting flow, were already itemized by Selle et al. [100]:

1. dispersion and dissipation of numerical schemes,
2. filtering operation on unstructured grids,
3. modeling subfilter phenomena.

The impact of these issues grows with the level of complexity of the flow as multiple instabilities can arise depending on the LES setting (as will be shown in this work). Despite these drawbacks LES represent the future in this field as RANS, for such complex turbulent flows, fails in predicting the proper velocity profiles. In Moin et al. [74] RANS

velocity profiles are off experimental data by a large amount. In Wang et al. [111] RANS predicts the two jets to counter rotate while experiment shows a strong mixing with only clockwise velocity profiles. In Kim and Syed [52] LES and RANS are directly compared: RANS modeling fails in predicting spreading of a swirling jet in a confined aero rig or to properly simulate jet in cross flow. This suggests that LES is the only tool which is sufficiently accurate to simulate swirl injectors.

	STRUCTURED	UNSTRUCTURED
RANS	Wang et al. [111]	Moin et al. [74]
LES	Wang et al. [111]	Jaegle et al. [48], Selle et al. [100] Roux et al. [91], Moin et al. [74]

Table 2.3: LES analyzed in this section

Considering LES performed at CERFACS, there is a clear trend in increase the simulation domain in order to include all geometrical details of the combustion chamber and the plenum. Such an increase and an effort to extend the CFD domain is mainly motivated by the importance of acoustics which requires proper boundary conditions. Clearly it is easier to define a boundary condition at the plenum inlet and outlet from the acoustics and fluid dynamics point of view than inside the vanes of a swirler or in the middle of a chamber. In the case of a multiple passages injector, computing the whole domain, including the plenum, also avoids to guess the flow split.
Note also that in none of the simulations of industrial swirlers of this section, bifurcations or hysteresis as the one shown here in chapters 3 & 4 were identified. Even though these mechanisms may have been observed, they were not reported yet. This is why they are specifically discussed in the present thesis.

Chapter 3

Sensitivity analysis of swirling flows LES to numerical settings

3.1 The LOTAR experiment: description and working conditions

The fuel injector used on LOTAR set-up is a SNECMA aeronautical injector displayed in Fig. 3.1 & 3.2. This multipoint injection system was used during the TLC European program [36]. It consists of a pilot injector, surrounded by two axial swirlers and a multipoint injection system, surrounded by a radial swirler with a perforated plate which let s air bypass the injection swirlers to create a cooling film on the periphery of the section [82] (here it will be also referred to cooling film).

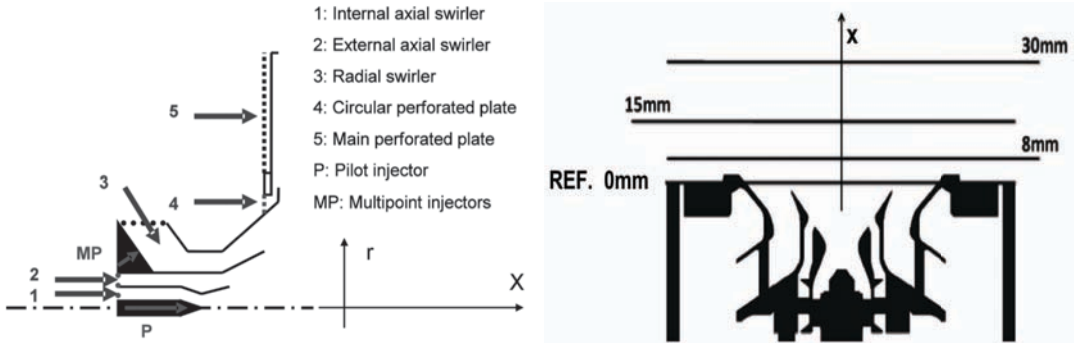

(a) (b)

Figure 3.1: (a) Injector scheme from ONERA KIAI deliverables[82] and (b) measurement planes. The zero position (REF. in Fig.) corresponds to the end plate of the injector.

Each swirler stage generates a counter rotating jet, increasing shear and turbulence level and improving mixing in between the two phases. Experimental measurements are taken in open atmosphere: the injector is fed with air and the resulting free jet is analyzed in terms of the mean and root mean square (RMS) velocity field. The injection device is mounted downstream of a plenum. Measurements are taken at three different planes situated 8 [mm], 15 [mm] and 30 [mm] downstream of the injector end plate along two

perpendicular directions, Fig. 3.1b. Velocity profiles were measured with a Laser Doppler Anemometry (LDA) technique [82]. ONERA used zirconium dioxide (ZrO2) particles injected inside the plenum; the particles mean diameter was 3e-6 [m] [82].

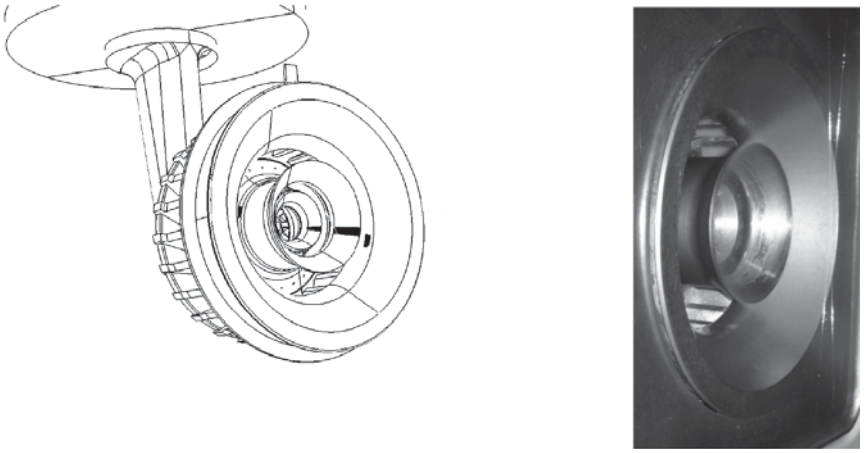

Figure 3.2: Injector device, CAD and real picture, from ONERA KIAI deliverables [82].

The injector is fed with a mass flow rate of 138 [g/s], with a confidence of 2.6 %, at 270 K. The atmospheric pressure of the chamber is 99000 [Pa]. Pressure is measured between the atmosphere and the plenum using a 0 to 10 kPa micro-manometer with an accuracy of 0.1 %. The pressure drop corresponding to this condition is **4.8 KPa**. Permeability measurements are also available with the corresponding flow split between the five different air passages of Fig. 3.1(three swirler stages + circular and main perforated plates). Globally 5 % of the mass flow rate pass through the innermost axial swirler (1 in Fig. 3.1a), 7 % through outermost axial swirler (2 in Fig. 3.1a) and 62 % through the radial stage (3 in Fig. 3.1a). The remaining 26 % is evacuated by the perforated plates (4 & 5 in Fig. 3.1a), used for cooling purposes.
Thanks to permeability measurements the flow split is, under a first approximation, known: it is therefore possible to avoid including these small passages in LES (as it will be done in chapter 4 *for all* flow passages of Fig. 3.1). Note that, even though bifurcations will be observed between the AJ and BB states (see the nomenclature of section 2.2) only the AJ state was observed experimentally. Studying bifurcation in LES was not the objective of the LOTAR experiment and no time was available to study this question experimentally at ONERA since it would have required substantial modifications of the experimental setup.

3.2 The LOTAR LES

The numerical settings are obtained by plugging the mesh obtained from the CAD of the swirler injector in an open atmosphere like cylinder. The swirler blows into open atmosphere where the domain is limited to a large cylinder with non reflecting boundary conditions [87] (Fig. 3.3 right). As in the experiment, the injector studied with these conditions in LES, generates an unconfined jet.

3.2.1 Boundary & initial conditions, numerical grid.

Fig. 3.3 shows a cut of the injector mounted inside the plenum and its boundary conditions (swirler B.C.s), the whole simulation domain and its boundary conditions (far field B.C.s). Boundary conditions are summarized in table 3.1.

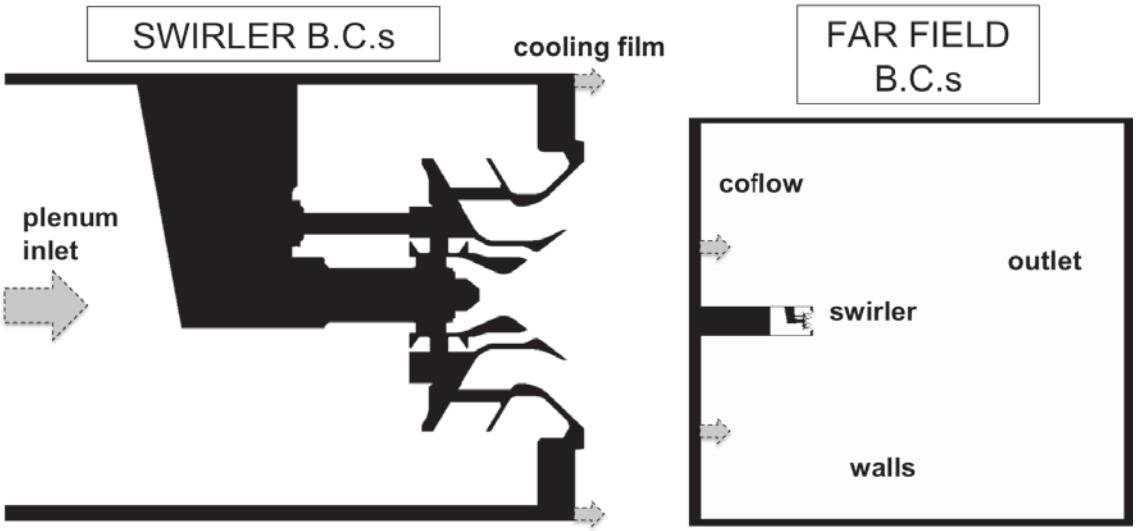

Figure 3.3: LOTAR boundary conditions. Arrows indicates inlets.

There are three inlets in the simulation domain, represented in Fig. 3.3 by arrows. The first inlet, named *coflow*[1], is introduced far upstream of the injector with an imposed velocity of 1 [m/s], (1.3 % of the jet characteristic speed). In the current analysis, the zone upstream of the injector is included (Fig. 3.3) and the largest flow structures generated by the jet in the cylindrical box are explicitly resolved. To test the effects of the coflow, a simulation was performed imposing a higher streamwise velocity (10 [m/s]) in section 4: the jet is not modified, confirming, as shown in [28], that the coflow speed has no major influence on the flow structure.
The second inlet, named *plenum inlet*, feeds only the two stages of the injector device, since the main and the circular perforated plates of Fig. 3.1(a), are not included in the geometry. The mass flow rate imposed at the *plenum inlet* is derived from the permeability measurement and equal to the supposed value passing through the swirler injector alone ($5\% + 7\% + 62\% = 74\%$ of 138 [g/s] so 102 [g/s]). This choice has been made to avoid meshing the extremely small details of the perforated plates.
The cooling film originated by the flow passing through the main perforated plate is not negligible in terms of top speed (from experimental results ≈ 40 [m/s]) and mass flow rate (from permeability measurement 22 % of 138 [g/s] so 30.36 [g/s]). Therefore a third inlet, named *cooling film*, representative of this flux, is directly introduced inside the atmosphere-like cylinder and the imposed target value is derived from the permeability measurement.

[1]The introduction of a coflow is a usual method to simplify the computation of jets, especially in terms of boundary conditions for compressible flows. It is justified only if the coflow has a limited effect on the results. This was verified in our setup for the configuration studied in Chapter 4, while these results are shown in Appendix B.

Fig. 3.4 clarifies this setup.

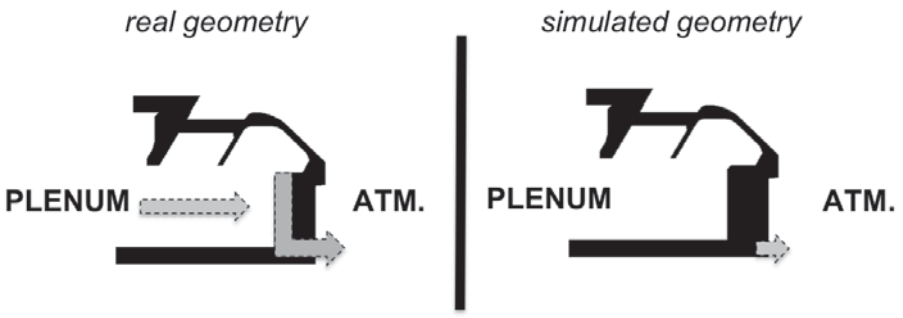

Figure 3.4: Real geometry scheme: a perforated plate connects the plenum and the open atmosphere (left). Simulated geometry, the perforated plate has been erased and an inlet is directly introduced in open atmosphere (right). The corresponding flow rate is deducted from the flow rate injected in the plenum by B.C. plenum inlet of Fig. 3.3.

At the periphery of the cylinder, solid walls are setup. The simulation outlet is located at the end of the cylinder. Boundary conditions at the periphery of the cylindrical box have been pushed as far as possible from the injector nozzle and the mesh size increases in their proximity to damp numerical oscillations. The bounding cylinder was sufficiently wide to totally contain the recirculation zone created by the jet, as will be shown later on. Because a bigger cylindrical box would have increased the computational cost without improving accuracy, its dimensions have been limited.

Reference temperature = 270 [K]		
BC NAME	IMPOSED PROPERTY	TARGET VALUE
coflow	velocity	1 $[m/s]$
plenum inlet	mass flow rate	102 $[g/s]$
cooling film	mass flow rate	30.3 $[g/s]$
outlet	pressure	99000 $[Pa]$
walls	adherence, impermeability, adiabaticity	

Table 3.1: Imposed values for boundary conditions sketched in Fig. 3.3.

In AVBP, as acoustics are directly simulated, each BCs target value is reached in a relaxation time (imposing a relaxation coefficient) to avoid reflexion of sound wave or their generation. In YALES2, thanks to the incompressibility assumption, boundary values are imposed in an hard way. Quantitatively, in terms of target values, the same set of boundary condition is used in YALES2 & AVBP. At the plenum inlet a volumetric mass flow rate is imposed and at the outlet, a reference pressure (in YALES2 outlet BC is based on the so-called *convective boundary condition* [85]). In both codes the imposed mass flow rates are the same. The mesh named *basic* in table 2.1 is presented in Fig. 3.5(a). The *basic* mesh has 2499443 nodes and 14081708 elements. It is a fully unstructured tetrahedral mesh. The minimum element volume is $\approx 3 \times 10^{-4}\,[\mathrm{mm}^3] < 0.1^3\,[\mathrm{mm}^3]$ and it is located inside the innermost axial swirler. The mesh wall resolution (Fig. 3.5(b)) expressed in terms of walls units:

$$y^+ = y\frac{u_\tau}{\nu}, \tag{3.1}$$

where u_τ is the friction velocity and y is the wall distance in [m], is in the range[2] y^+ $[30, 100]$.

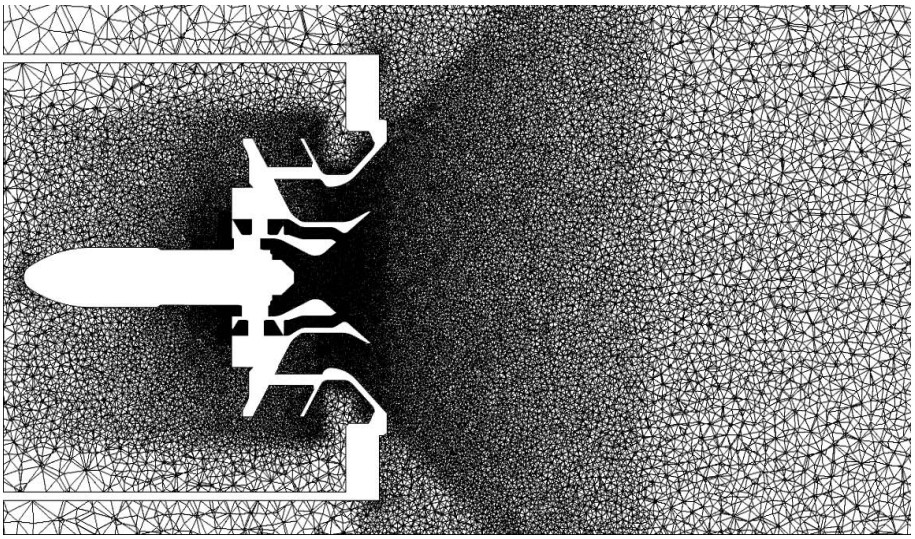

(a) Mesh, bulk of the jet.

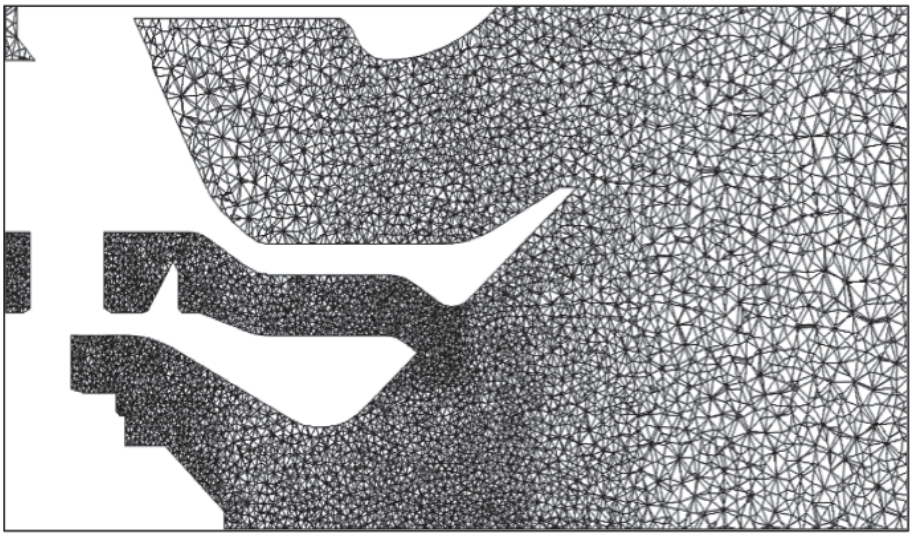

(b) Mesh, zoom at the walls.

Figure 3.5: Numerical grid named *basic* mesh.

Most simulations start from a zero velocity[3] solution except when bifurcation diagrams are studied for which LES are initialized using the final state of the previous run, as it will be done in chapter 4. All simulations run for at least 0.050 [s] equivalent to 5 flow through times, considering the plenum length, O(0.1) [m] and imposed velocity, O(10) [m/s].

[2]In Chapter 9 the y^+ distribution in the domain is shown.

[3]In AVBP the initial velocity field was imposed to be 1 [m/s] to avoid the generation of acoustic waves by the *coflow* inlet.

3.2.2 LES solvers & settings.

All simulations of the present work are performed using the compressible LES solver named AVBP [93, 92] or the incompressible LES solver named YALES2 [76].
AVBP is a finite-volume/elements solver, cell-vertex (i.e. variables are stored at nodes while conservation laws are integrated inside the elements).
YALES2 is a finite-volume solver, vertex centered (equations are solved at the element vertex), 4th-order accurate in space.
The numerical scheme chosen for time advancement is Lax Wendroff for AVBP while is TRK4 [55], for YALES2. TRK4 (or TFV4A) is a fourth order time integration scheme providing a large region of stability (in terms of the Courant-Friedrichs-Lewy, CFL, number) which gives the possibility to adjust the incorporated numerical diffusion [55]. The CFL number chosen for the current study is 0.9 for YALES2 and 0.7 (acoustic CFL number) for AVBP.
Both solvers use classical LES models. The Large-Eddy Simulation derivation of governing equations is obtained by introducing operators to be applied to the set of compressible or incompressible Navier-Stokes equations. Unclosed terms arise from these manipulations and models need to be supplied for the problem to be solved. The peculiarity of LES comes from the operator employed in the derivation. In LES, the operator is a spatially localized time independent filter of given size, Δ, to be applied to a single realization of the studied flow. This spatial average creates a separation between the large (greater than the filter size) and small (smaller than the filter size) scales. The unclosed terms are representative of the physics associated with the small, high frequency, structures present in the flow [6].
The filtered incompressible NS equations (which are chosen to be presented here for their simpler formulation) reduce to (using the implicit summation rule):

$$\frac{\partial u_i}{\partial x_i} = 0, \tag{3.2}$$

$$\frac{\partial u_j}{\partial t} + \frac{\partial \widetilde{u_i u_j}}{\partial x_i} = \nu \frac{\partial^2 u_j}{\partial x_i \partial x_j} - \frac{1}{\rho}\frac{\partial p}{\partial x_j}. \tag{3.3}$$

which are the mass and the momentum conservation equations respectively. The symbol f defines the mass weighted filter $f = \overline{f\rho}/\overline{\rho}$ where $\overline{f}$ is the spatial filter applied to the property f. The second term on the left-hand side of equation 3.3 is split in two parts: one part that is explicitly resolved and a second part, representative of the smallest flow scales, that is modeled. This second part is the so-called sub-filter (or sub-grid), stress tensor:

$$\frac{\partial \widetilde{u_i u_j}}{\partial x_i} = \frac{\partial (u_i\ u_j)}{\partial x_i} - \frac{\partial \tau_{ij}^{SGS}}{\partial x_i}. \tag{3.4}$$

For implicit filtering LES (i.e. the grid size corresponds to the filter size), the terms sub-filter scale and sub-grid scale (SGS) have the same meaning. The isotropic part of the SGS tensor is included in the modified filtered pressure term p [89], while the anisotropic part is modeled as:

$$\tau_{ij}^{SGS} - \frac{1}{3}\delta_{ij}\tau_{kk} = 2\rho\nu_{SGS}(S_{ij} - \frac{1}{3}\delta_{ij}S_{kk}). \tag{3.5}$$

Equation 3.5 assumes that the SGS term is aligned with the rate-of-strain tensor S_{ij}: this assumption is also known as the eddy viscosity assumption originally applied to the time-averaged NS equations (Boussinesq, 1877). However, in many Direct Numerical Simulation

(DNS), S_{ij} and τ_{ij}^{SGS} are found to be poorly correlated [70]. The proportionality coefficient between these two tensors is the turbulent viscosity, ν_{SGS}. Turbulent viscosity is expressed as:

$$\nu_{SGS} = (C_m \Delta)^2 D_m(u), \tag{3.6}$$

so that ν_{SGS} is proportional to the square of the grid size per an ad-hoc coefficient multiplied by a differential operator associated with the model $D_m(u)$ [80]. Two SGS models are chosen for the current study. The first is SIGMA [80], whose differential operator (i.e. turbulent viscosity coefficient) goes to zero in near-wall regions in order to mimic the turbulence damping due to the no-slip condition (turbulent stress should decay as the distance to the solid boundary to the third power [15]) and vanishes in the case of a flow in solid rotation and in the case of a pure shear [80]. These properties are of importance since the flow under examination in the present study is both confined and swirled.
The second is Dynamic Smagorinsky, whose ad-hoc coefficient is computed dynamically as the calculation progresses rather than input a priori [29]. The model is constructed to generate an effective viscosity which is proportional to some measure of the turbulent energy at the high wavenumber end of the spectrum [49] which evidently vanishes in the case of laminar flows and therefore is suited, for instance, to simulate transition to turbulence [49]. However, this model shows a very good performance even when its basic hypothesis (i.e. scale similarity) is not satisfied and it is argued [49] that the reason why it works so well is that it contains a sensor which responds to the energy in the high wavenumber of the spectrum before it contaminates the energy containing range [49].

3.3 Terminology.

Here the different jets definitions and the measurement locations of some fluid dynamics properties, are clarified. These definitions will be used later on during the sensitivity analysis. In all the table and figures, the experimental data are named *EXP*. For clarity, the different swirlers, stages and jets are summarized in Fig. 3.6A. Each swirler device is made of different vanes. The two coaxial swirlers, forming the axial swirler stage, will be referred to the **innermost** (or the inner) and the **outermost** (or the outer) axial swirlers. The flow passing through these swirlers (or simply passages) generates the **innermost** respectively **outermost axial jets** which together are called the **central jet**. On the contrary, the radial swirler, or the radial stage, generates the **radial jet**.

3.3.1 Non-dimensional numbers

For all simulations of this sensitivity analysis, the swirl (Eq.(2.2)) and Reynolds (Eq.(2.1)) numbers have been monitored at three different locations (S_1, S_2 and S_3, Fig. 3.6B), in order to be representative of the three different jets before they merge in common structures. It has to be noticed that:

- the swirl number (defined by Eq. (2.2)) of the outermost axial jet (measured on surface S2 in Fig. 3.6B), shows no dependence on the particular sampling location (as the axial momentum flux and angular momentum are invariant of the free jet, even if in this case it is a wall bounded jet);

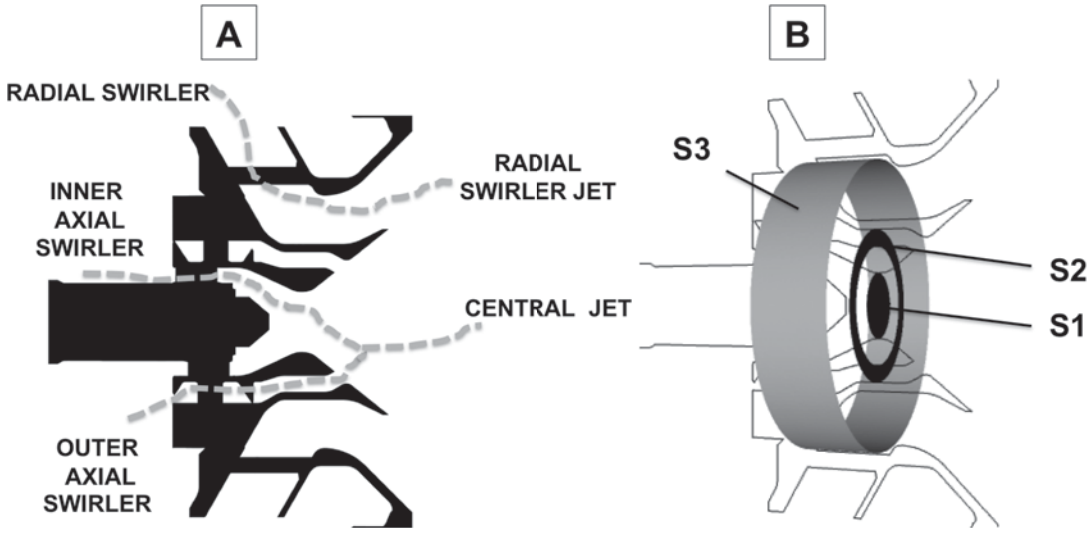

Figure 3.6: Different swirlers, stages and jets of LOTAR.

- the swirl number of the innermost axial jet (measured on surface S1 in Fig. 3.6B) has been measured at the minimum section. It varies because of the curvature of the injector and of the recirculation zones present in the innermost bowl; at the location chosen in Fig. 3.6B it is exactly equal to the swirl measured inside the vanes;

- the swirl number of the radial jet varies too because of the strong flow curvature (which turns from radial to axial direction). For this reason, the swirl number of the radial jet, evaluated using formula 2.2, does not properly represent the flow and the swirl ratio (defined by Eq.(2.3)) has been monitored instead.

The swirl ratio is measured on a cylindrical surface ($R = const.$) downstream of the radial swirler boundary condition (surface S3 in Fig. 3.6). Here, introducing the approximation of constant jet velocity and density, the two definitions, Eq.(2.2) & Eq.(2.3), are equivalent:

$$S = \frac{\int_A \rho u_d u_\theta r dA}{R \int_A \rho u_d^2 dA} \approx \frac{\int_A u_\theta dA}{\int_A u_d dA} = S_r, \tag{3.7}$$

where u_d is the discharge speed ($u_d = u_r$ on $S3$ in Fig. 3.6). The monitored quantities of the different jets are summarized in table 3.2. Note that the value of R is the same for all jets and equal to $R = 0.018\,[\mathrm{m}]$. The Reynolds number results of each jet are close to $O(40000)$ for the outer axial jet and $O(75000)$ for the inner and for the radial jets, independently of the flow configuration.

	Reynolds	Swirl ratio	Swirl number
Formula	Eq.(2.1)	Eq.(2.3)	Eq.(2.2)
Symbol	Re	S_r	S

Table 3.2: Non-dimensional numbers monitored for the different jets of Fig. 3.6B

3.3.2 Jet opening half-angle.

LES results and experimental data are presented in cylindrical coordinates. Experimental data, extracted for each of the three planes of Fig. 3.1, along two lines normal to each other, are averaged into a single curve using the axisymmetry of the results. The same procedure is repeated for the LES results in order to use the same approach for both, the simulation and the experiment. LES and experimental data are then compared along the radial direction. The jet opening half-angle has been measured at the 30 [mm] plane (Fig. 3.1b) and it is defined as the angle subtended at the apparent origin by the axis and a line to the half-velocity radial location, so: $\frac{u(r)}{u_{max}(r)} = \frac{1}{2}$ [32]. The definition of the jet opening half-angle is explained in Fig. 3.7.

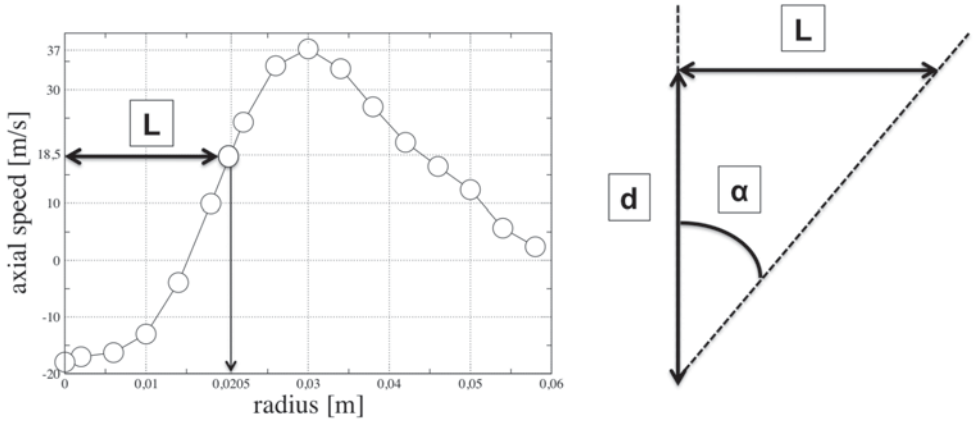

Figure 3.7: Evaluation of the jet opening half-angle for experimental data at the last measurement plane of Fig. 3.1. L = radial location of the half velocity, $d = 30[mm]$ (distance from the injector ending plate), α is the jet opening half-angle.

For all the BB states shown in the next sections (with a jet that stick to the diffuser walls and expands radially), α is set to 90 deg. For experimental data (circles in Fig. 3.7) the radial location at which axial velocity is half of the jet top speed is $L = 20.5[mm]$, therefore for $d = 30[mm]$ it corresponds to a jet opening half-angle of $\alpha = arctan(\frac{L}{d}) \approx 34 \ \ deg$. **Note that throughout this thesis $R_0 = 30[mm]$ is taken as the injector reference radius**.

3.4 Baseline simulation of the LOTAR swirler

The baseline LOTAR simulation has been first performed using the SIGMA model [80] coupled with no-slip boundary conditions at the solid boundaries on both codes while the other boundaries are shown in table 3.1. The simulations settings are summarized in table 3.3.

name	mesh	code	SGS	Wall
AVBP-SIGMA	basic	AVBP	SIGMA	NO SLIP
YALES-SIGMA	basic	YALES2	SIGMA	NO SLIP

Table 3.3: Baseline LES

3.4.1 Global flow field

Both codes show the same general behavior and only minor discrepancies are present. Despite the fact that the two LES codes are very different, they provide similar results. This result is quite encouraging considering that RANS solvers usually exhibit much larger variability for such flows. Opening half-angles of the jets are 90 deg (as evident from Fig. 3.8) in LES results of both codes. The jet arising from the radial swirler first separates in the diffuser then soon reattaches following the geometrical curvature of the device. The central jet, generated by the two inner coaxial swirlers, sticks to the wall until it merges with the outermost flow (Fig. 3.8).

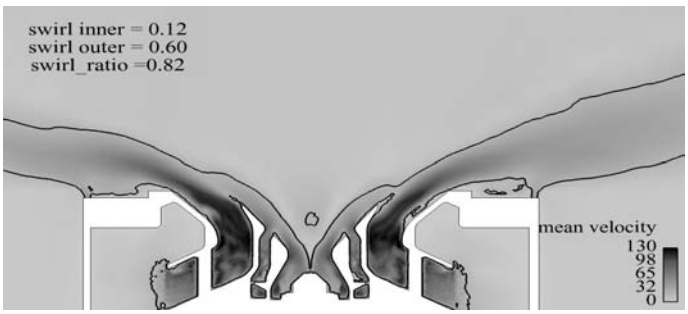

(a) AVBP-SIGMA

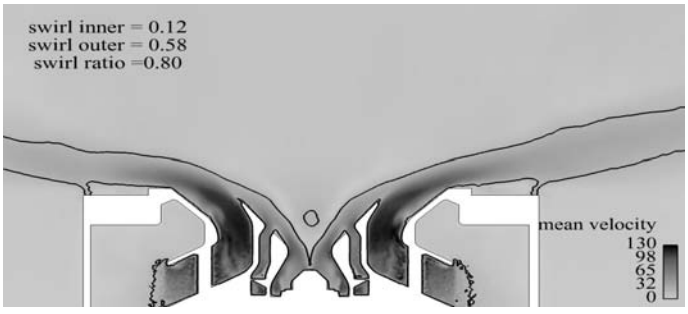

(b) YALES-SIGMA

Figure 3.8: Mean velocity magnitude [m/s] and mean velocity isoline ($u_{mean} = 10$ [m/s]) for simulations of table 3.3. The swirl values indicated on the figures correspond to the swirl number (S, Eq.(2.2)) for the inner and outer jets and to the swirl ratio (S_r, Eq.(2.3)) for the radial jet.

3.4.2 Flow split and pressure drop

Both codes provide a similar flow split in the two different stages. The small discrepancy in the total mass flow rate is due to the AVBP target oriented BC (target values are not imposed in a hard way but reached in a relaxation time to limit acoustic oscillations). Most of the flow is passing through the radial swirler, because of its bigger section, table 3.4. Computed pressure drops are similar within the two codes, table 3.5.

Flow repartition			
	axial stage	radial stage	total
EXP	16.5 [g/s]	85.5 [g/s]	102 [g/s]
AVBP-SIGMA	13.8 [g/s]	88.6 [g/s]	102.4 [g/s]
YALES-SIGMA	14.2 [g/s]	87.6 [g/s]	102.0 [g/s]

Table 3.4: flow repartition in the baseline configuration

Pressure drop		
	LES	reference
EXP	4800 Pa	+0%
AVBP-SIGMA	8248 Pa	+72%
YALES-SIGMA	7945 Pa	+66%

Table 3.5: pressure drop in the baseline configuration

3.4.3 Swirl numbers and ratio

The swirl numbers and the swirl ratios computed by the two codes are similar, table 3.6 & table 3.7.

Swirl number		
	AVBP-SIGMA	YALES-SIGMA
INNER	0.12	0.12
OUTER	0.60	0.58

Table 3.6: Swirl numbers, S Eq.(2.2), for the baseline configuration

Swirl ratio		
	AVBP-SIGMA	YALES-SIGMA
mean axial velocity	32.5 [m/s]	33.50[m/s]
mean radial velocity	-41.77 [m/s]	-41.34[m/s]
mean tangential velocity	-33.45 [m/s]	-34.08[m/s]
Swirl ratio, Eq.(2.3)	0.8	0.82

Table 3.7: Mean velocities and swirl ratios, S_r Eq.(2.3), for the baseline configuration

3.4.4 Recirculation zone

The recirculation zone extends several diameters downstream of the injector orifice along the streamwise and radial directions (Fig. 3.9). The recirculation zone slightly differs in the two codes because of different running times of the two simulations related to the cheaper numerical cost of YALES2. Note that the far field, i.e. the flow inside the cylindrical box, keeps on slowly evolving while the jet remains, unaffected, in the same flow state.

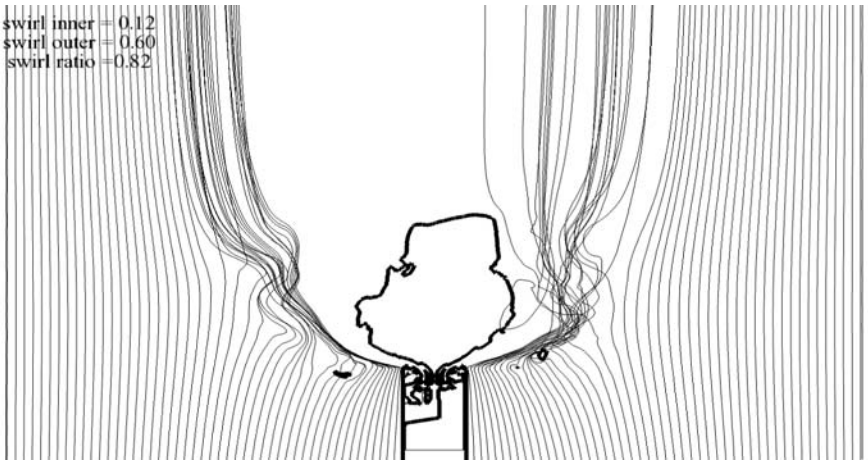

(a) AVBP-SIGMA

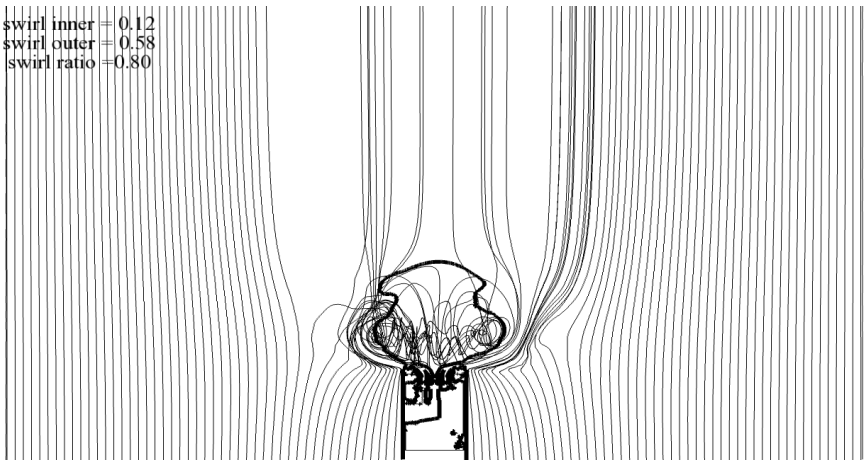

(b) YALES-SIGMA

Figure 3.9: Recirculation bubble. Zero axial velocity (thicker black line) and streamlines for simulations of table 3.3. The seeding used is a line upstream of the injector and is the same for both simulations.

3.4.5 Comparison with experimental data

LES results show a poor comparison with experimental measurements, the two LES codes simply predict the wrong flow topology. The swirling jet obtained experimentally at ONERA is a free Axial Jet (see section 2.2.3) as shown by the size of the recirculation zone (Fig. 3.10), the high tangential velocity (Fig. 3.10) and high turbulence intensity

inside the CTRZ[4] (as it will be shown later in Fig. 3.15). On the contrary, LES using the settings of table 3.3 predicts in both codes a flow that looks like a Blasted Breakdown jet (BB) of section 2.2.3. The wrong LES prediction is evident from Fig. 3.10 which shows profiles of axial, radial and tangential velocity at three axial positions.

3.4.6 Summary of the main features of the "baseline" run

The baseline LOTAR simulation was performed on both codes using SIGMA as SGS model coupled with no-slip boundary conditions at the solid walls. In both codes the opening angle is large ($\approx 90\,\text{deg}$). Both codes predict, in the axial swirlers, a similar swirl number, table 3.6, flow split, table 3.4, and swirl ratio of the radial jet, table 3.7. The recirculation zone established by the jet is wide and spans several injector diameters in both radial and axial directions (Fig. 3.9). The pressure drop through the device estimated by both codes is higher than experimental results, table 3.5. Comparisons with velocity profiles of experimental data are poor (Fig. 3.10). Obviously the two LES codes have a major difficulty to predict this case: the two LES codes predict a jet in the BB state[5] (using the nomenclature of section 2.2.3) while the experiment corresponds to an AJ state. LES prediction and experimental measurements do not match because they corresponds to two totally different flow states.

[4]Note that no pressure signal from the inside of the jet was taken experimentally.

[5]This classification will be proven and clarified in section 3.6.

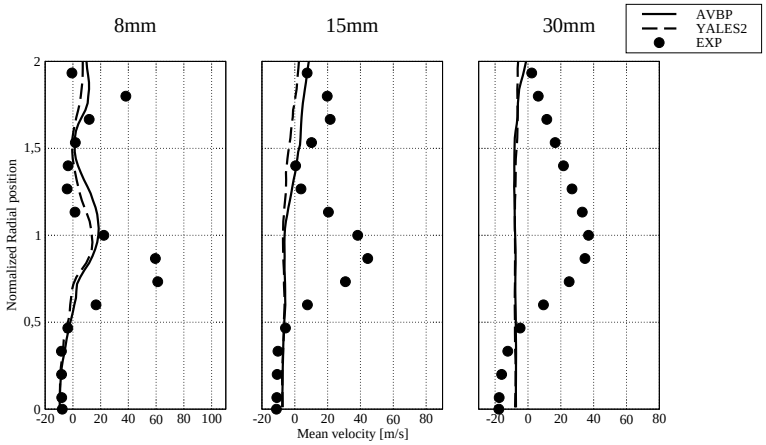

(a) Axial

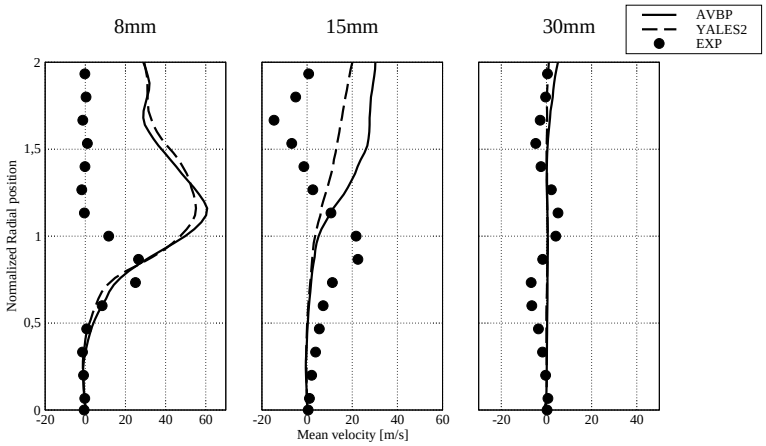

(b) Radial

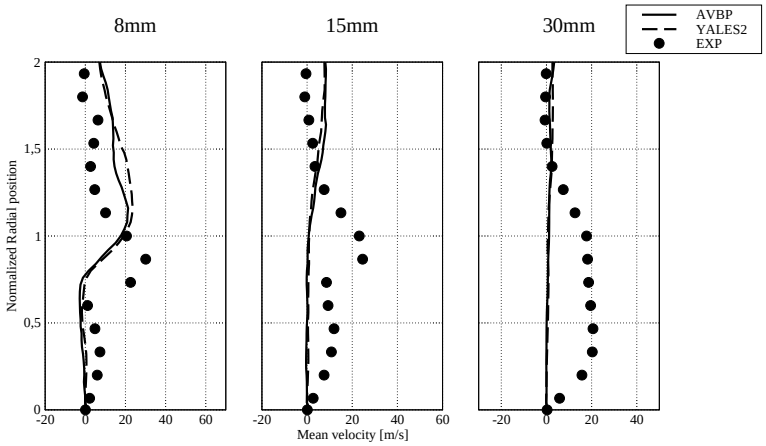

(c) Tangential

Figure 3.10: Velocity profiles for AVBP-SIGMA and YALES-SIGMA, the normalization radius is $R_0 = 30[mm]$.

3.5 Sensitivity to SGS modeling

The previous section has shown that both YALES2 and AVBP failed to give proper results for the first two runs of Table 2.1, apparently capturing the wrong flow state (BB instead of AJ). In this section the effect of the SGS term is investigated by replacing the SIGMA model [80] used in section 3.4 by the Dynamic Smagorinsky model [29] in both codes, keeping constant all other numerical parameters.

3.5.1 Global flow field

name	mesh	code	SGS	Wall
AVBP-DSMAG.	basic	AVBP	DYN. SMAGO.	NO SLIP
YALES-DSMAG.	basic	YALES2	DYN. SMAGO.	NO SLIP

Table 3.8: Influence of the SGS model tests

The first result obtained when changing the SGS model is that the flow state changes: a strong flow reconfiguration is induced in both codes. Jet opening half-angle is now reduced to $\approx 23 - 33\,\text{deg}$ from $\approx 90\,\text{deg}$. The BB jet experienced in the previous simulations has disappeared (Fig. 3.11). Despite the fact that the two codes give a similar jet opening half-angle (showing a net improvement with respect to the run of section 3.4), the flow fields slightly differ.

3.5.2 Flow split and pressure drop

Flow split changes with the jet configuration but both codes compute a similar flow split, which is now closer to permeability measurements, table 3.9.

Flow repartition			
	axial stage	radial stage	total
EXP	16.5 [g/s]	85.5 [g/s]	102 [g/s]
AVBP-DSMAG.	15.7 [g/s]	86 [g/s]	101.7 [g/s]
YALES-DSMAG.	16.1 [g/s]	85.9 [g/s]	102.0 [g/s]

Table 3.9: Flow split for simulations of table 3.8.

While flow split results (table 3.9) are closer to experimental data, pressure drop predictions (table 3.10) deteriorate with the Dynamic Smagorinsky model. This phenomenon is explained by the higher levels of turbulent viscosity generated at the solid boundaries (with a $y+$ in the range [30,100]) by the Dynamic Smagorinsky model compared to SIGMA. Higher turbulent viscosity levels create:

- an increase of the dissipation rate of kinetic energy,
- a reduction of the hydraulic section of the vanes, since the velocity at the solid boundary is damped.

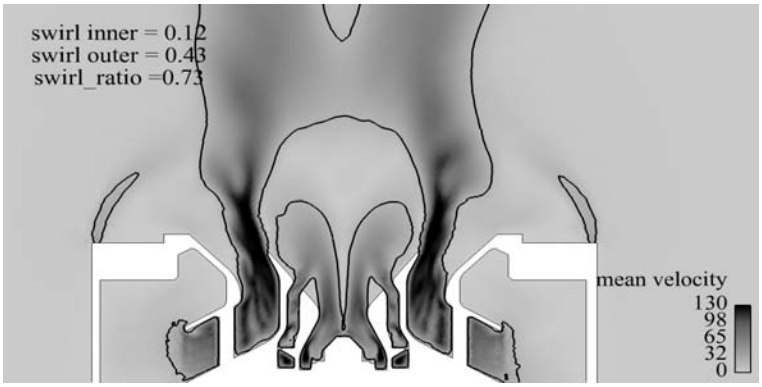

(a) AVBP-DSMAG.

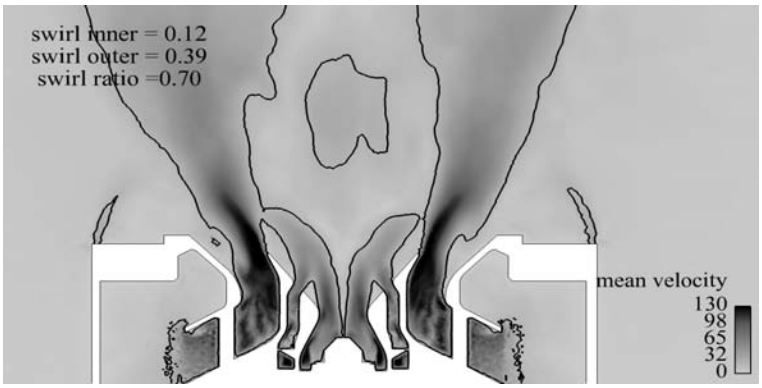

(b) YALES-DSMAG

Figure 3.11: Mean velocity for simulations of table 3.8.

Both effects increase pressure losses through the injector device. The fact that pressure drop predictions deteriorate while comparison of other quantity with experimental data improves (Fig. 3.14) may suggests that pressure drop prediction could be an issue decoupled from velocity prediction. With respect to the simulations of section 3.4, the mass flow rate passing through the radial stage has decreased (tables 3.4 & 3.9). This is an evidence of the dissipation distribution between the passages: as the level of turbulent viscosity increases, the mass flux decreases in the less resolved passage for a given hydraulic diameter, that is for the *basic* mesh, the radial one. However, the effects of the strong curvature of the radial jet, present in the results obtained with SIGMA, can also impact the flow split. It is therefore difficult to separate the dissipative effect of an increased viscosity in the swirler vanes from the different amount of dissipation related to the flow configuration.

3.5.3 Swirl numbers and ratio

The most important difference between the SIGMA computations of section 3.4 and the Dynamic Smagorisnky simulations of table 3.8, is the substantial decrease of the swirl number of the outer jet (from 0.6 to 0.43) and of the swirl ratio of the radial jet (from 0.8 to 0.7). Tables 3.11 and 3.12 show these quantities. Both codes give similar results.

Pressure drop		
code	LES	reference
EXP	4.8 [Kpa]	+0%
AVBP-DSMAG.	12930 Pa	+166%
YALES-DSMAG.	12272 Pa	+155%

Table 3.10: Pressure drop for simulations of table 3.8.

Swirl number		
	AVBP-DSMAG.	YALES-DSMAG.
INNER	0.12	0.12
OUTER	0.43	0.39

Table 3.11: Swirl number, Eq.(2.2), for simulations of table 3.8. To be compared with table 3.6.

Swirl ratio		
	YALES-DSMAG.	AVBP-DSMAG.
mean axial velocity	30.14 [m/s]	29.4[m/s]
mean radial velocity	-41.3 [m/s]	-39.84[m/s]
mean tangential velocity	-29 [m/s]	-29 [m/s]
swirl ratio	0.7	0.73

Table 3.12: Swirl ratio, Eq.(2.3), for simulations of table 3.8. To be compared with table 3.7.

3.5.4 Recirculation zone

The recirculation zone is different in the two codes (Fig. 3.12) even though the overall topology is the same. While the CTRZ is well defined in YALES2, this structure is narrower in AVBP. The narrow central recirculation bubble in AVBP (Fig. 3.12) is related to the behavior of the central jet. Vortex breakdown is triggered by the pressure gradient (induced by the rotational motion) which overwhelms the jet inertia along the axial direction. The central jet in AVBP has a higher inertia along the axial direction (Fig. 3.11) therefore a higher penetration than the jet simulated by YALES2. As a consequence, the size of the recirculation bubble is reduced. Also, the dynamics of the detachment of the jet from the diffuser wall changes with SGS modeling (see the different lip close to the diffuser on Fig. 3.12) and this can affect the jet opening half angle and therefore the shape of the recirculation zone. Peripherical recirculation zones, equivalent to corner recirculation zones, are induced in the flow field (Fig. 3.13). These structures disappear for longer simulation times. It is very likely that the differences observed in Fig. 3.13 are due to the very long time required to converge and to the sensitivity of the recirculation zone to the details of the boundary condition. The asymmetry in the far field flow, visible from Fig. 3.13, can be related to mesh effects (small asymmetry in the azimuthal direction in the far field mesh) as suggested by Moreau [75].

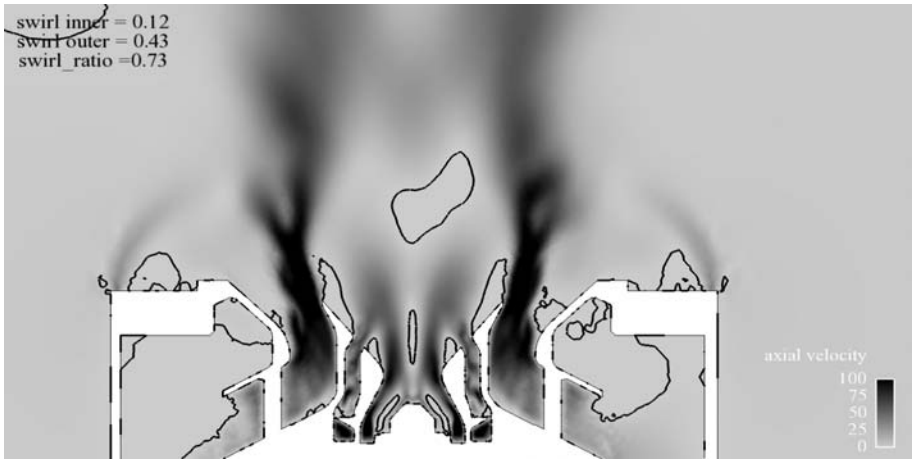

(a) AVBP-DSMAG.

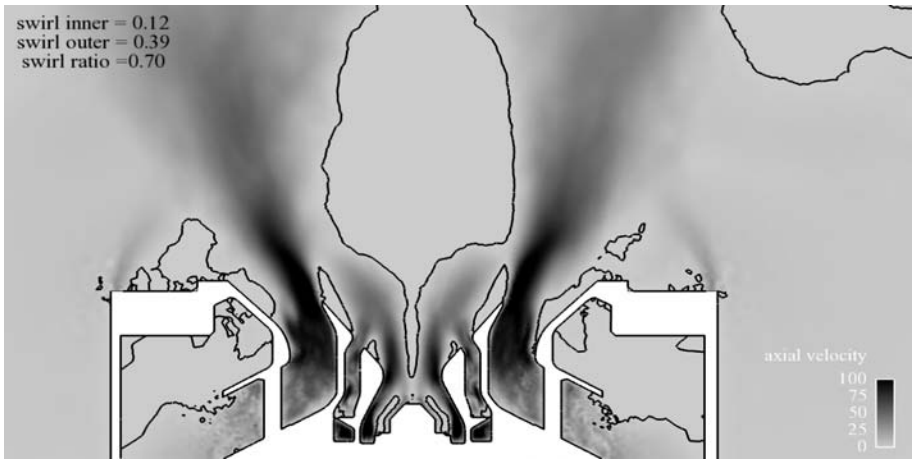

(b) YALES-DSMAG.

Figure 3.12: Recirculation bubble, mean axial velocity component and zero velocity isoline for simulations of table 3.8.

3.5.5 Comparison with experimental data

The smaller recirculation bubble in AVBP is confirmed also by the comparison with experimental data (Fig. 3.14) which is not fully satisfactory but much better than in section 3.4. With respect to the previous configuration both codes show a better comparison with measurement, because the wrong flow topology, the BB state, has been replaced in both solvers by a different state: AJ which is coherent with the experimental data.

3.5.6 Summary of the main features of the run

The SGS model has a deep impact on the flow behavior: the flow state changes radically depending on this parameter. The flow split also changes with an increase of the mass flow rate in the axial stage (table 3.9). A net decrease of the swirl number in all passages and of the swirl ratio of the radial jet is also experienced (tables 3.11 and 3.12). Similarly to the previous case, the two codes predict similar flow split and swirl but in this case the

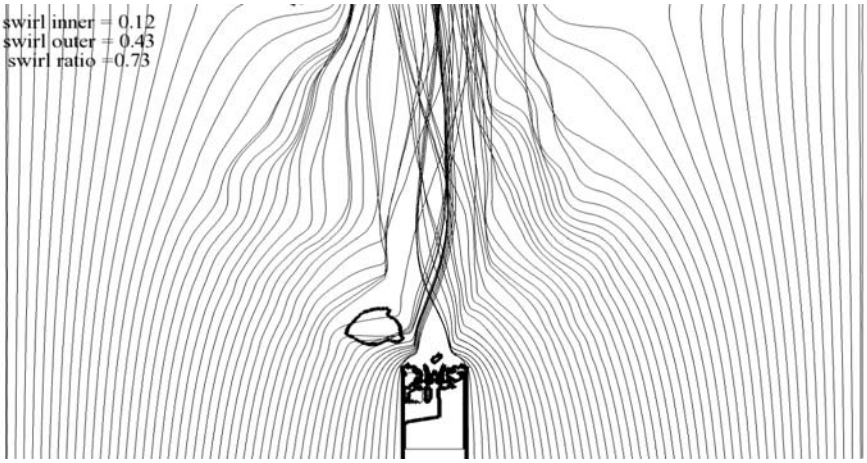

(a) AVBP-DSMAG.

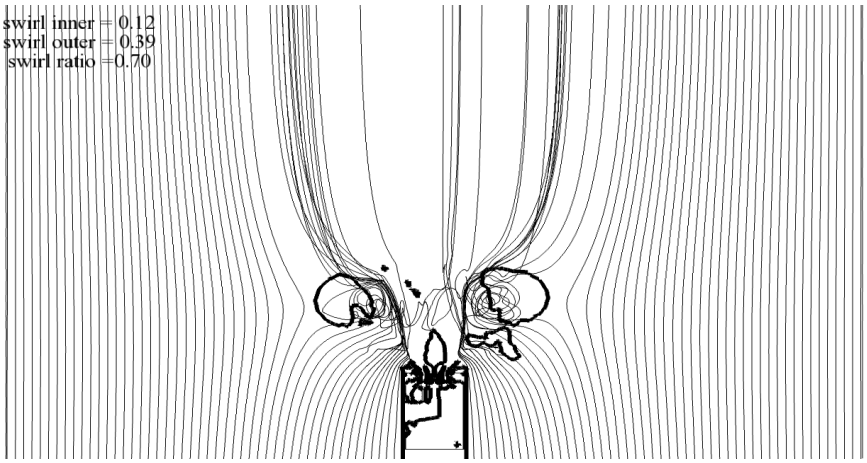

(b) YALES-DSMAG.

Figure 3.13: Recirculation bubble zoom out, zero axial velocity line (thicker black line) and streamlines for simulations of table 3.8.

recirculation zone shape changes (Fig. 3.12): YALES2 shows a well defined CTRZ while AVBP produces a much narrower one. This difference could be related to the central jet, which in AVBP has (Fig. 3.11 or plot 3.14) a higher axial penetration. Comparison with experimental data is sufficient for both codes if compared with the results obtained in section 3.4.

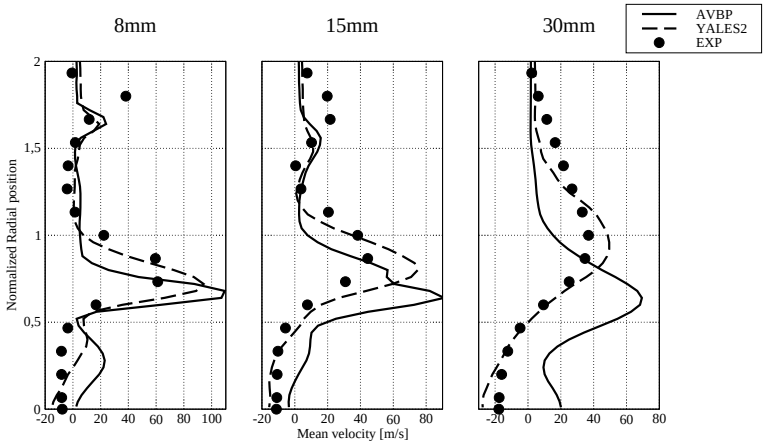

(a) Axial

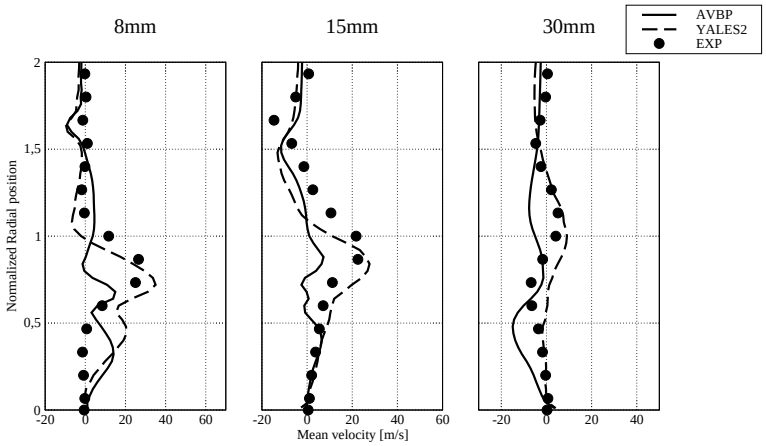

(b) Radial

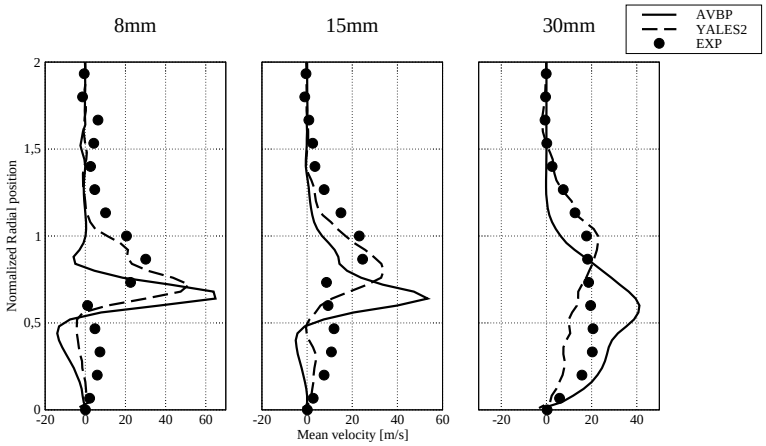

(c) Tangential

Figure 3.14: Velocity profiles for AVBP-DSMAG. and YALES-DSMAG, the normalization radius is $R_0 = 30[mm]$.

3.6 Classification & analysis of the flow states.

The previous sections show that two flow configurations appear depending on the SGS model. The first configuration is obtained with the SIGMA model and corresponds to a jet opening half-angle $\alpha \approx 90\,\text{deg}$ and a BB state. The second configuration is obtained with Dynamic Smagorinsky and corresponds to a jet opening half-angle of $\alpha \approx 20 - 30\,\text{deg}$ and an AJ state. The first configuration ($\alpha \approx 90\,\text{deg}$) is characterized by a wider recirculation zone (Fig. 3.10) and by (inside the CTRZ) a zero tangential velocity (Fig. 3.10), a negligible turbulent activity and sub-pressure (Fig. 3.15). The second configuration is characterized by a recirculation zone smaller than one injector diameter (Fig. 3.14) and a high tangential velocity (Fig. 3.14), a high level of turbulent activity and a high subpressure coefficient ($P_D = \frac{P_{atm}-P}{0.5\rho U_0^2} \approx 0.7$) close to the injector orifice (Fig. 3.15). The comparison of these flow states with Vanierschot s jets [105] is shown in Appendix D.

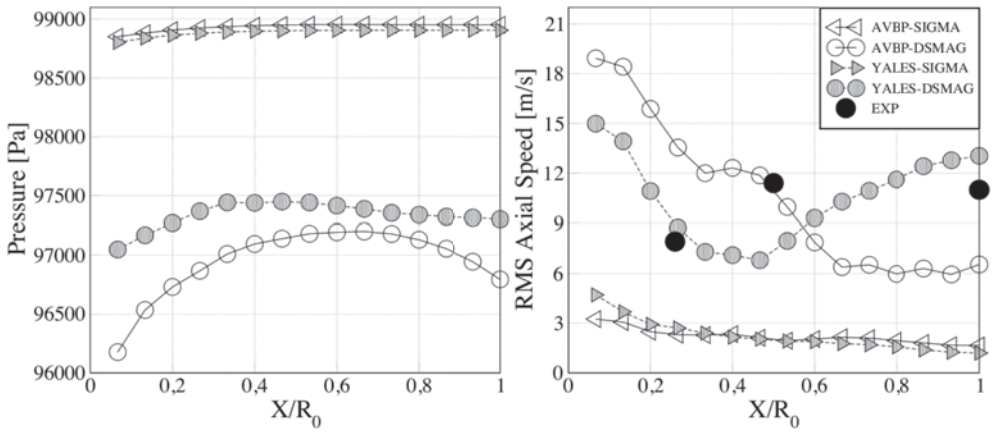

Figure 3.15: Axial velocity RMS and pressure distribution measured along the centerline of the geometry for simulations of tables 3.3-3.8. Results are plotted against normalized axial distance (X/R_0) from the swirler end plate. Experimental data are available only for RMS values.

Considering also results shown in Fig. 3.15, and using the nomenclature introduced in section 2.2.3, the $\alpha \approx 90\,\text{deg}$ state can be classified as a Blasted Breakdown Jet (BB) since it shows flow properties similar to the BB state described by Vanierschot et al. [105]. Similarly, the $\alpha \approx 20 - 30\,\text{deg}$ configuration can be classified as a free Axial Jet (AJ). The BB state is not observed experimentally while the AJ state shows a good comparison with experimental data. Both BB & AJ states appear independently of the LES solver used, i.e. AVBP or YALES2, even if some discrepancies in prediction between the two codes are present.
Obviously, the two LES codes predict two very different states for this flow depending on small changes (LES sub-model). In the next sections these results will be analyzed and it will be demonstrated that they are not due to numerical artifacts but to the fact that the present flow is very close to a bifurcation and therefore very sensitive to all parameters (physical or numerical).

3.7 Sensitivity to the mesh

An interesting observation from tables 3.7 & 3.12 is that the AJ state is characterized by a lower swirl ratio ($S_r \approx 0.7$) in the radial jet (measured on surface S3 of Fig. 3.6) while the BB state is characterized by a higher swirl ratio ($S_r \approx 0.81$) in the radial jet. This variation of the swirl ratio can be justified only by an *effective geometry* variation or by a variation of the fluid dynamics conditions, both due to SGS modeling. As it will clarified in appendix A, SGS modeling in the wakes of the radial swirler vanes and inside the vane itself is able to modify the amount of swirl in the flow. **A low resolution in this zone of high shear can create numerical noise that modifies the jet velocity**[6]. The Dynamic Smagorinsky model damps the velocity gradient because of its higher turbulent viscosity that smoothes the velocity field. The SIGMA model does not: therefore numerical noise can modify the solution. **In order to reduce this noise, the mesh has been refined in the wake of the radial swirler passages, upstream inside the vanes and downstream, inside the swirler bowl**. This new mesh is named *optimized*. The *basic* and the *optimized* meshes (optimization based on the macro flow analysis of section 3.6) are shown side by side in Fig. 3.16. The optimized mesh has 15873485 cells. Typically, the basic mesh had $6-7$ nodes in the flow passages while the optimized mesh has roughly twice this number at the same location[7].

[6]The same issue is happening at all the nozzle lips but is more evident for the radial swirler because its vanes are closer to each others with respect to the inner and outer swirler vanes.

[7]Note that it was not possible to generate a mesh with a prismatic layer at the wall for this configuration because of the complexity of the geometry.

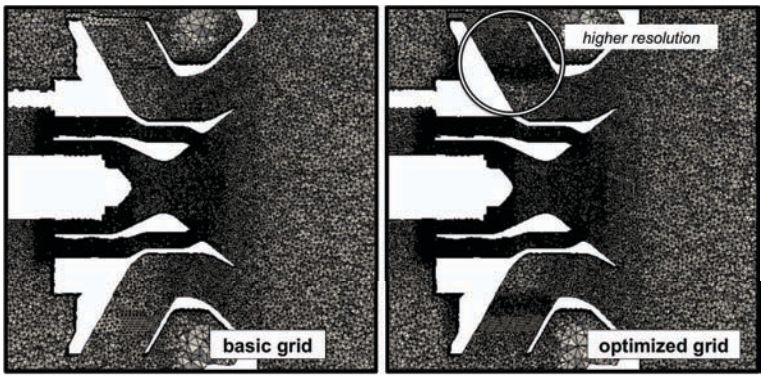

(a) axial-radial directions cut

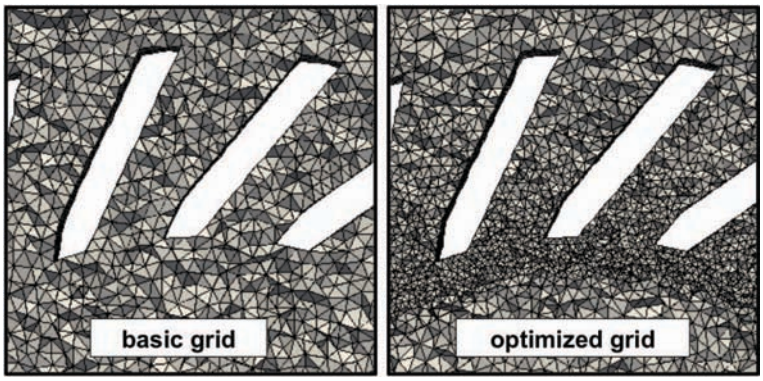

(b) tangential-radial directions cut

Figure 3.16: Optimized vs. basic mesh.

3.7.1 Global flow field

The first remarkable result of the computations performed on the locally refined mesh shown in Fig. 3.16 is that, on the optimized mesh, the flow topology observed for the baseline case (section 3.4) changes again: a strong modification of the jet opening half-angle is observed for the BB state, characteristic of the LES with the SIGMA model, with a net improvement of predictions. The simulations of this section are itemized in table 3.13. LES outputs are still code independent and the AJ state is now predicted by both SGS models as evident from the high subpressure and turbulence intensity fields (Fig. 3.17) or simply from the jet direction (Fig. 3.18).

name	mesh	code	SGS	Wall
YALES-DSMAG_O	optimized	YALES2	DYN.SMAG.	NO SLIP
YALES-SIGMA_O	optimized	YALES2	SIGMA	NO SLIP
AVBP-SIGMA_O	optimized	AVBP	SIGMA	NOSLIP

Table 3.13: simulation table, effects of the mesh

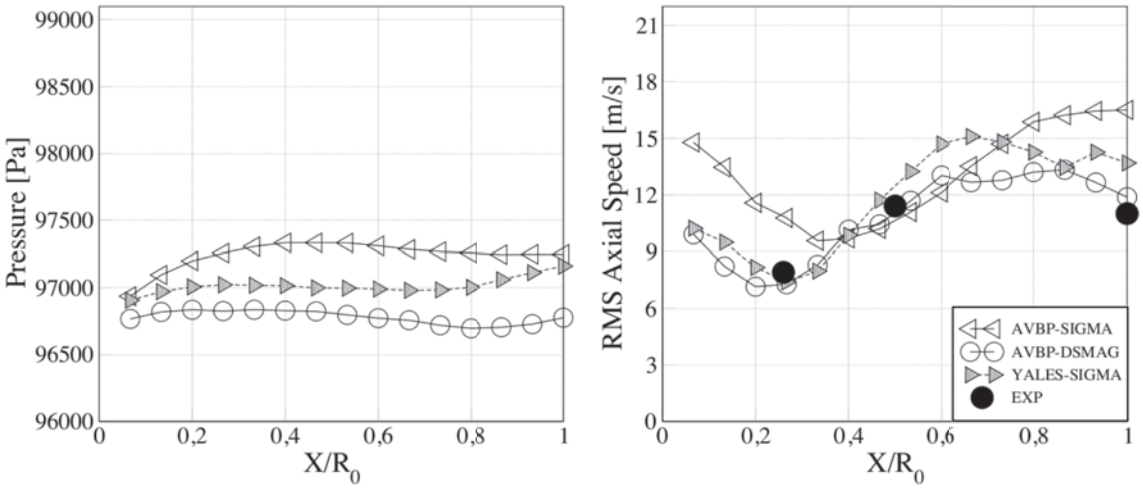

Figure 3.17: Axial velocity RMS and pressure distribution measured along the centerline of the geometry for simulations of table 3.13. Results are plotted against normalized axial distance (X/R_0) from the swirler end plate. Experimental data are available only for RMS values.

3.7.2 Flow split and pressure drop

Flow split and pressure loss predictions are in line with the previous simulations: Dynamic Smagorinsky LES predict a higher pressure drop, table 3.15, and a higher mass flow rate through the axial stage, table 3.14. Pressure drop predictions are similar in both codes.

3.7.3 Swirl numbers and ratio

The scatter of the swirl number of the outer jet for the various simulations already experienced in the previous sections (tables 3.6-3.11), is present also with the optimized mesh (table 3.16). This result is expected since it is related to the mesh resolution along the

Flow repartition			
	axial swirlers	radial swirler	total
EXP	16.5 [g/s]	85.5 [g/s]	102 [g/s]
YALES-DSMAG_O	15.9 [g/s]	86.1 [g/s]	102.0 [g/s]
YALES-SIGMA_O	15 [g/s]	87 [g/s]	102.0 [g/s]
AVBP-SIGMA_O	15.7 [g/s]	85.8 [g/s]	101.5 [g/s]

Table 3.14: Flow repartition for simulations of table 3.13.

Pressure drop		
RUN	LES	reference
YALES-DSMAG_O	10657 Pa	+122%
YALES-SIGMA_O	8535 Pa	+77%
AVBP-SIGMA_O	8647 Pa	+80%

Table 3.15: Pressure drop for simulations of table 3.13.

outer jet streamlines: since the mesh was not modified in this zone, this scatter (related to SGS modeling) had to appear also with the *optimized* mesh. On the contrary, the swirl ratio of the radial jet is lower than 0.8 for all the simulations of table 3.13 (table 3.17) and mesh refinement has reduced the variability due to SGS modeling shown by LES on the basic mesh (tables 3.7 & 3.12) .

Swirl number			
	YALES-SIGMA_O	YALES-DSMAG_O	AVBP-SIGMA_O
INNER	0.12	0.12	0.12
OUTER	0.58	0.4	0.52

Table 3.16: Swirl number, Eq.(2.2), for simulations of table 3.13.

3.7.4 Recirculation zone

Recirculation zones differ in the different simulations because of the different swirl number and because of the central jet detachment dynamics (with Dynamic Smagorinsky the central jet detaches, see section A). YALES2 and AVBP give similar results (Fig. 3.19).

3.7.5 Comparison with experimental data, *optimized* mesh

Comparison with experimental data is sufficient for the Dynamic Smagorinsky simulations while the best agreement is obtained using SIGMA (Fig. 3.20). AVBP and YALES2 give extremely similar curves using the SIGMA model and results are close to experimental data.

3.7.6 Summary of the main features of the run

This section shows how a small refinement, localized in the wake of the tiny jets in the radial swirler bowl, is sufficient to eliminate most of the limitations due to the SGS model

Swirl ratio			
	YALES-SIGMA_O	YALES-DSMAG_O	AVBP-SIGMA_O
axial	34.6	32.8[m/s]	-34.5
radial	-41.45	-41.3 [m/s]	-40.96
tangential	-30.58	-29 [m/s]	-30.71
swirl ratio	0.74	0.72	0.76

Table 3.17: Swirl ratio, Eq.(2.3), for the *optimized* mesh.

effects. Comparison with experimental data is now reasonable for all the simulations using the SIGMA model, independently of the code.

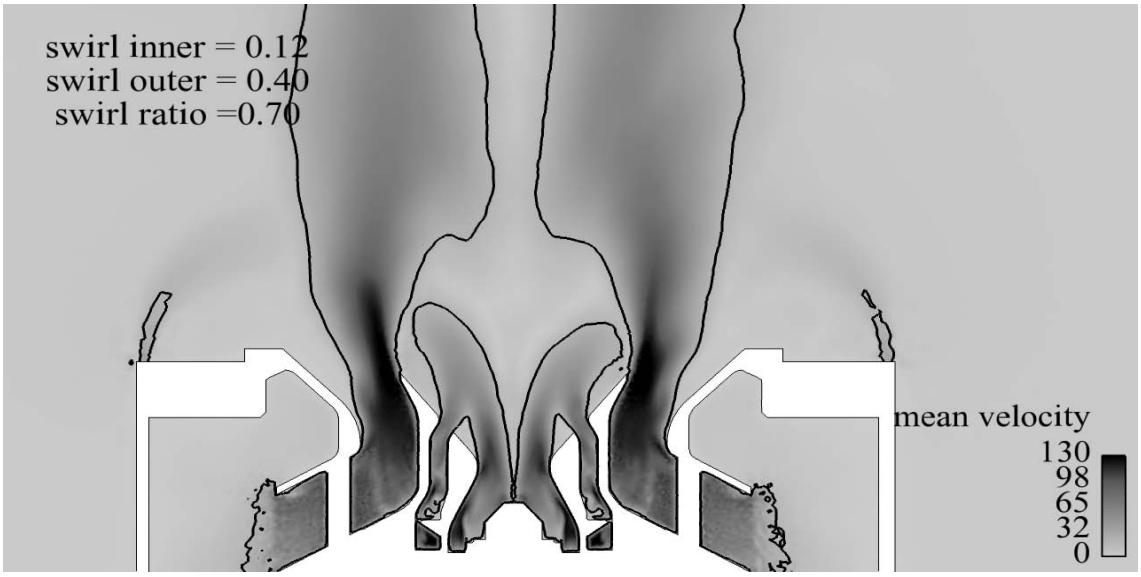

(a) YALES-DSMAG_O

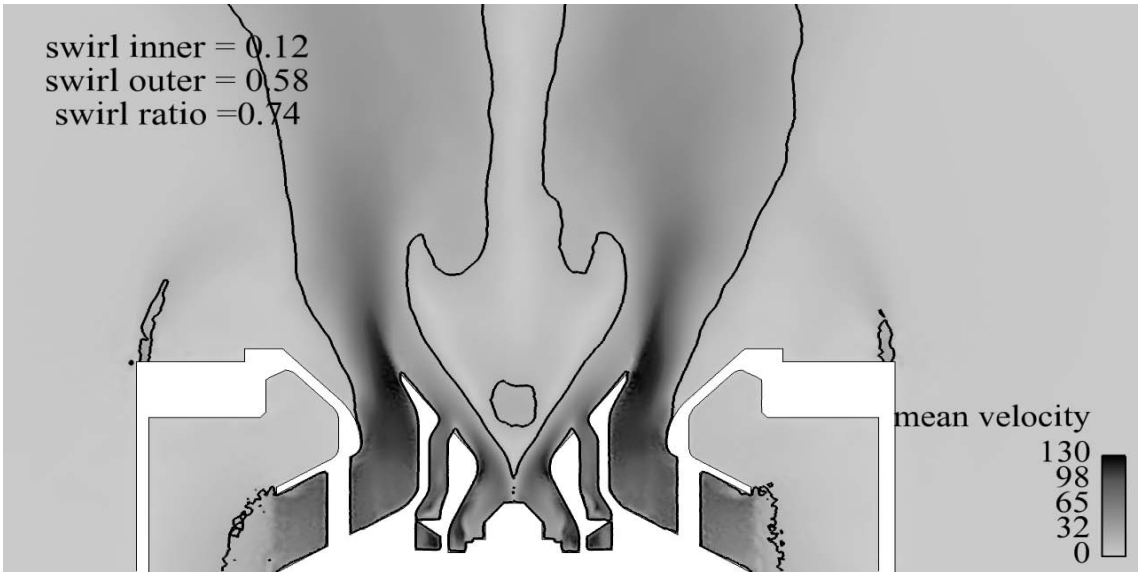

(b) YALES-SIGMA_O

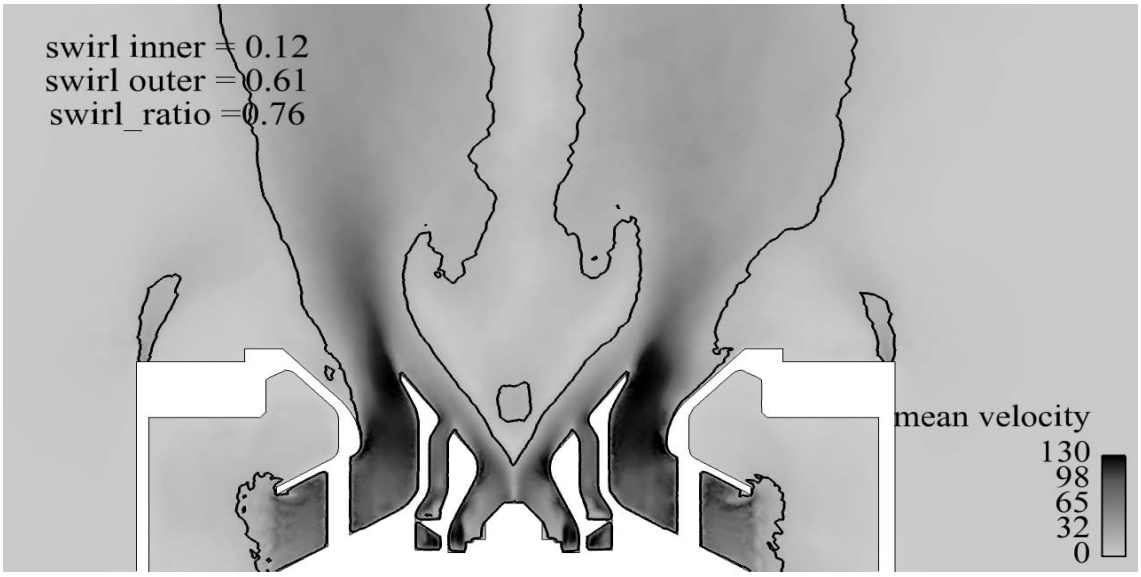

(c) AVBP-SIGMA_O

Figure 3.18: Mean velocity for LES of table 3.13

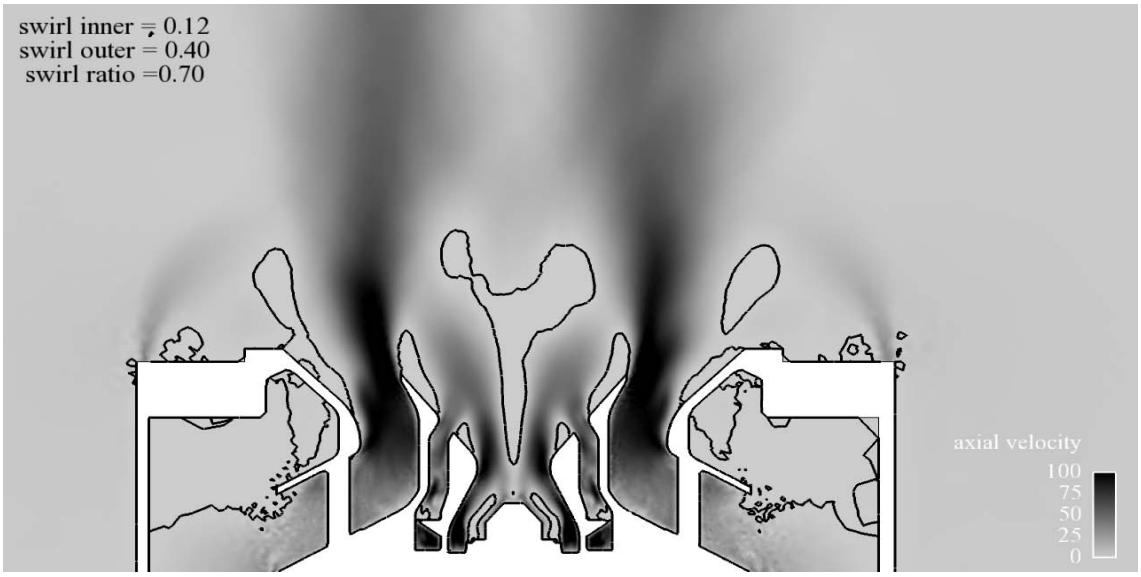

(a) YALES-DSMAG_O, the central jet detaches because of high turbulent viscosity, see section A.

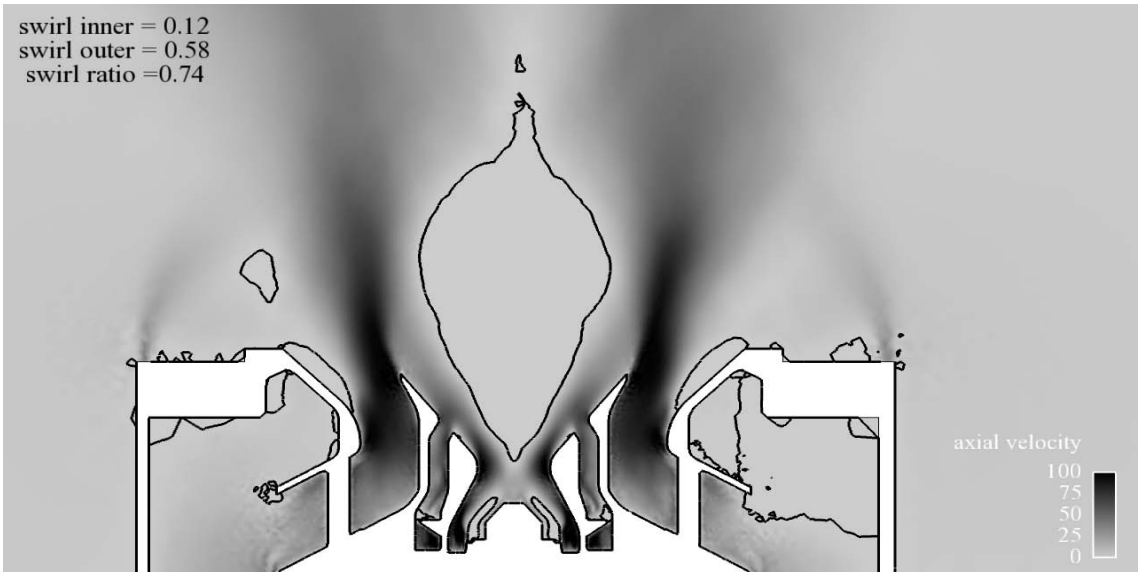

(b) YALES-SIGMA_O

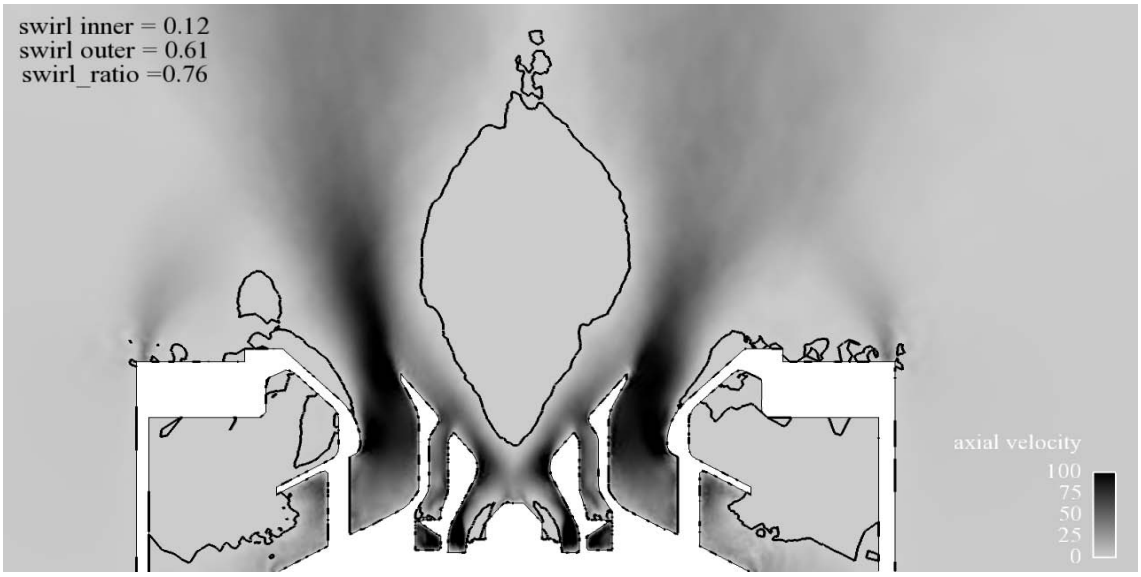

(c) AVBP-SIGMA_O

Figure 3.19: Recirculation bubble, velocity isolines and zero isosurface.

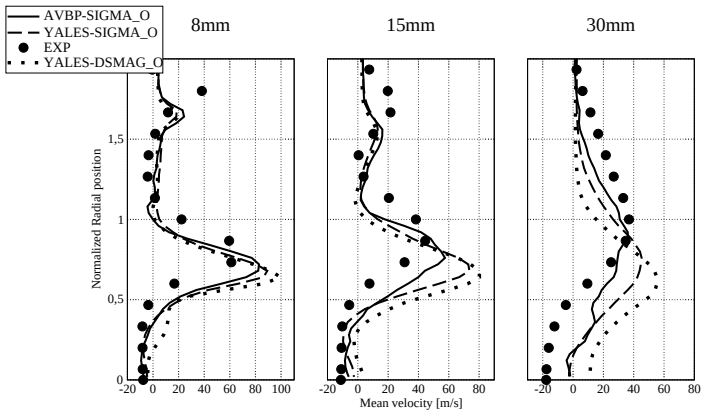

(a) Axial

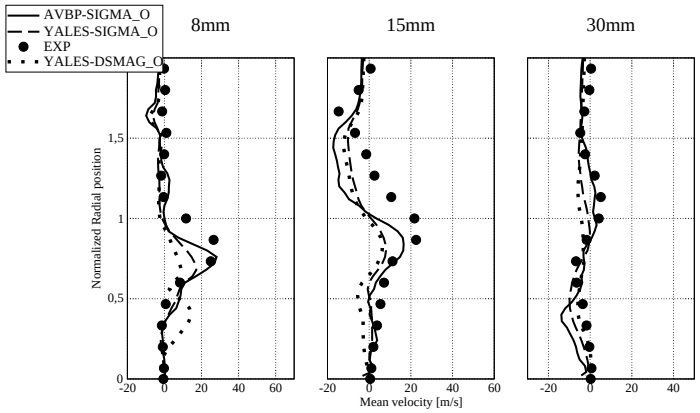

(b) Radial

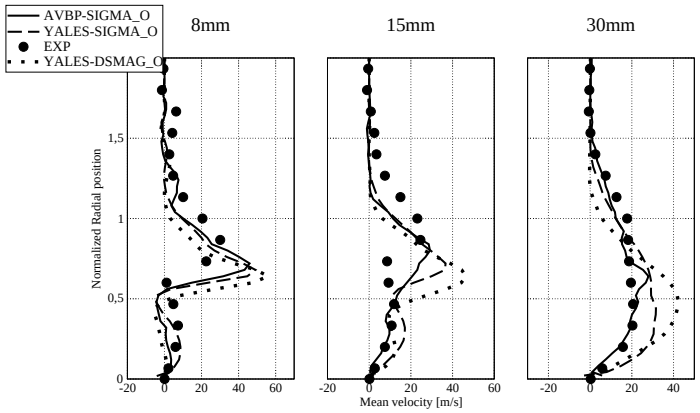

(c) Tangential

Figure 3.20: Velocity profiles, YALES-SIGMA_O, YALES-DSMAG._O, AVBP-SIGMA_O, the normalization radius is $R_0 = 30[mm]$.

3.8 Synthesis of results and explanation scenario

The sensitivity analysis of the LOTAR LES described in sections 3.4 to 3.7 shows that:

1. the swirl ratio (Eq. 2.3) variation of the radial jet is related to numerical noise/error which can be damped or not by turbulent viscosity and reduced by mesh refinement (as explained in appendix A),

2. flow split & pressure loss and the detachment dynamics of the central jet are dependent on the SGS model used (as explained in sections 3.10 and clarified in appendix A: these variations are related to the different amount of turbulent viscosity generated by the SGS model at the solid walls),

3. the mesh quality plays an important role and only the optimized grid allows to obtain coherent conclusions even though the optimized mesh has a $y^+ \quad [30, 100]$.

The previous simulations require further analysis and can be used to propose an explanation for the observed results.

3.8.1 An hypothesis on the source of bifurcation.

The jet opening half-angle and the swirl ratio of the radial swirler are plotted for all simulations of table 2.1 in Fig. 3.21. Independently of the code used, the jet-opening half angle shows a small linear dependence on the swirl ratio (S_r) as long as the flow is in the AJ state ($S_r \leq 0.76$). This result is consistent with the correlation between S and α proposed by Gupta et al. [32] (Eq.(2.8)) which is also displayed[8] in Fig. 3.21.
Above $S_r \approx 0.76$, the linear dependence is lost because the flow undergoes a transition to the BB state: the jet opening half-angle becomes $\alpha \approx 90\,\text{deg}$.

A possible interpretation of Fig. 3.21 is that the state BB is obtained in both codes for a swirl ratio of $S_r = 0.8 - 0.82$ (measured on section S3 of Fig. 3.7), while AJ states are obtained for a smaller swirl ratio ($S_r \approx 0.76$). This suggests a possible explanation for the sensitivity of the flow to the numerical settings: in some cases numerical parameters or mesh (or their coupling) lead to a higher swirl ratio and this change leads to a BB state while, in other cases, numerical parameters lead to a smaller swirl ratio and this change leads to an AJ state. This explanation makes sense only if a small variation of swirl can trigger a large jet re-configuration, something that is possible only if the flow conditions are close to critical. **However, too many flow properties change depending on the mesh resolution or on the SGS model employed** (see tables 3.4-3.6-3.9-3.11-3.14-3.16 which show a high scatter of the flow split and of the swirl number of the inner and outer jets).
If the proposed explanation is valid, i.e. if the flow state is mainly controlled by one parameter only, the swirl ratio S_r, this can be checked by using another set of simulations where only S_r would be changed in a controlled manner. In the fixed geometry setup, S_r was not controlled: it was the result of the numerical setup and, as shown in Fig. 3.21, it was changing over a wide range because the flow within the swirler was changing.

[8] Note that Eq.(2.8) shows the dependence of the jet opening half-angle (α) on the swirl number (S) while Fig. 3.21 is a $S_r - \alpha$ diagram. However, Eq.(3.7) shows that the swirl number and the swirl ratio are equivalent if measured on surface S_3 of Fig. 3.6.

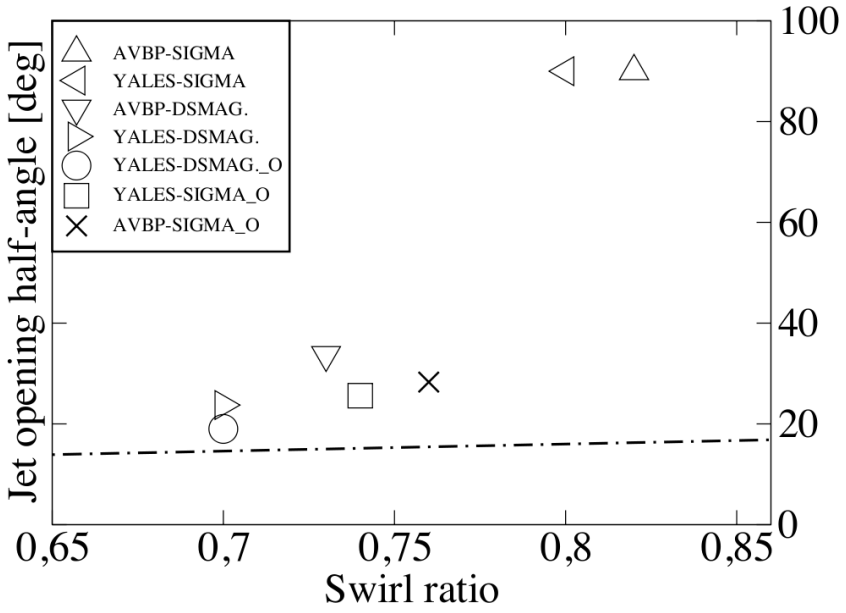

Figure 3.21: Jet opening half-angle (Fig. 3.7), vs. swirl ratio measured on surface S3 of Fig. 3.6 of all LES of table 2.1 performed in this chapter. Dashed lines group the AJ and BB states while the dot-dashed line is the correlation (Eq.(2.8)) proposed by Gupta et al.[32]. The correlation of Eq.(2.8) and LES results do not match very well. This was expected since Eq.(2.8) is obtained by regression of single free-swirling jets, a condition far from the LOTAR experiment.

To clarify this issue, a modified swirler geometry (Fig. 2.1 right) will be tested in LES (chapter 4) where the simplification of the geometry allows to change the swirl levels easily and to decouple each jet from the others while keeping all numerical parameters constant.

3.8.2 Pressure drop

Fig. 3.22 shows the predicted pressure drops measured in all LES of the previous sections. First, the pressure drop is weakly dependent of the particular flow state (AJ-BB) while it is strongly dependent of the SGS model used (turbulent viscosity level modifies the effective hydraulic section of the flow). Second, mesh refinement localized at a position of high numerical error (Fig. 3.16) improves pressure drop, compare[9] YALES-DSMAG. and YALES-DSMAG._O in Fig. 3.22. This is consistent with basic hydraulic concepts: pressure drop is a function of distributed and localized losses. Finally the error level on pressure drop remains too high for all cases shown here and the y^+ (Eq. 3.1) is in the range[10] $[30, 100]$ for all LES performed in this Chapter. Note that the wall resolution in terms of y^+ is also very inhomogeneous in the various swirler vanes, a phenomenon which could affect flow split direclty and pressure drop indirectly.
However, the pressure drop results computed here are in line with previous results obtained on similar geometries (at least when the SIGMA model is used). For instance the LES computations of Jaegle on a very similar injector [47] predict a pressure loss error of +54% despite the use of a dedicated wall function. Similarly Barre et al.[7] mismatched pressure

[9]Note that this comparison makes sense only for the Dynamic Smagorinsky LES which show the same flow state independently of the mesh resolution

[10]In Chapter 9 the y^+ distribution in the domain is shown.

losses from +105% to +52% with respect to experimental data (depending on the grid resolution, from a y^+ of $O(60)$ to O(15) respectively) on a much simpler swirler geometry using both YALES2 and AVBP.

Finally flow split between the swirler and the cooling films is an additional source of uncertainty which could influence pressure drop. The pressure drop issue is not further investigated here but it remains an open question for such type of confined flows and requires further work.

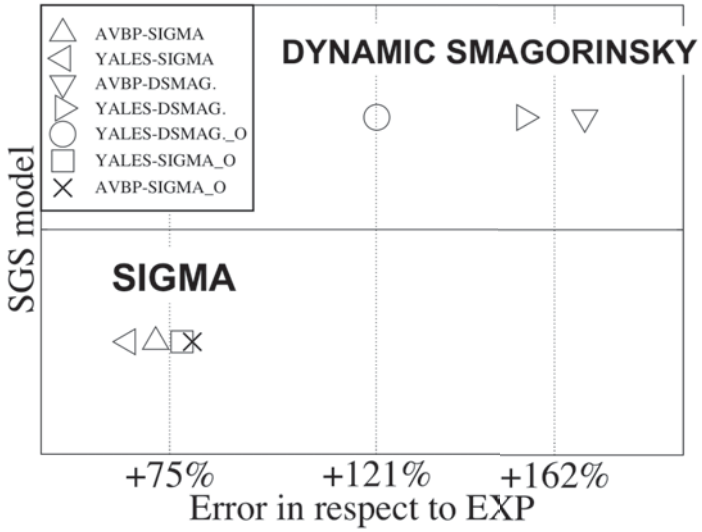

Figure 3.22: Pressure drop of all LES of table 2.1 performed in this chapter.

3.8.3 Numerical considerations

The sensitivity analysis of the LOTAR LES shows that:

- Numerical error is an important issue. The most important (because of its supposed effect on the overall flow behavior, see section 3.8.1) numerical error is generated by the strong velocity gradient soon at the exit of the radial swirler vanes, between the solid boundary and the multiple jets cores.
- High levels of turbulent viscosity can damp numerical error: turbulent viscosity smoothes the velocity gradients and indirectly reduces it.
- A LES with a SGS model which generates low turbulent viscosity, as SIGMA does, can be contamined by numerical noise. Such LES is more demanding in terms of mesh quality, but it can give very good results if the grid is sufficiently refined.
- A LES with a SGS model which generates high levels of turbulent viscosity, as Dynamic Smagorinsky does, is less contamined by numerical noise on under-resolved

meshes. The quality of such a simulation is low, since this viscosity level is not physically justified. The outcome is a **poorer prediction of pressure loss, flow split** and of the velocity profile (on a proper mesh) with respect to SIGMA and the generation of non-physical flow behavior (like the detachment of the central jet, see appendix A).

- A reduced, localized mesh refinement, can have a deep impact on the velocity profiles. In figure 3.23 turbulent kinetic energy, just downstream of the exit of the radial swirler vanes, is shown for two SIGMA simulations on the *basic* vs. *optimized* meshes. A low resolution in this critical area makes the distribution of turbulent kinetic energy fuzzy and undefined, while a higher resolution leads to a flow field of kinetic energy organized along the recirculation bubbles.

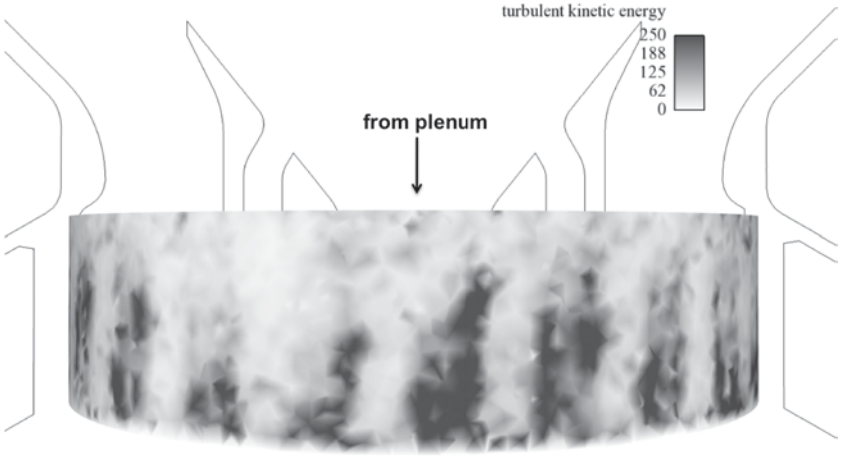

(a) YALES-SIGMA

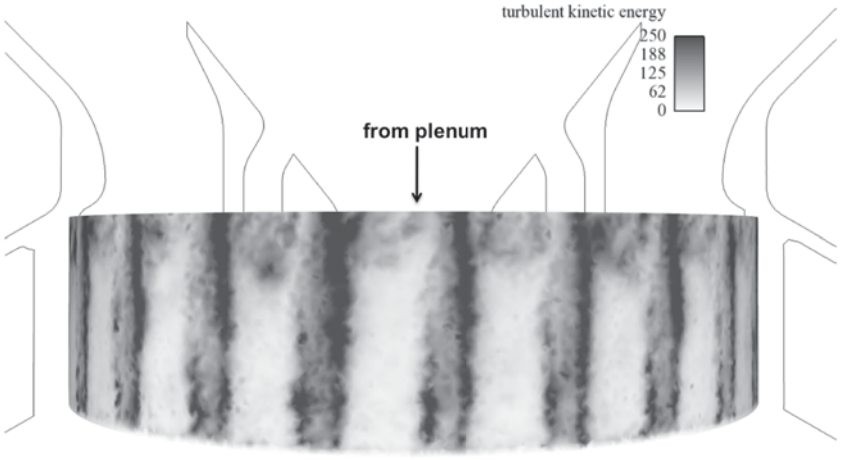

(b) YALES-SIGMA_O

Figure 3.23: Turbulent kinetic energy levels on a cylindrical surface inside the radial swirler bowl, just downstream of the exit of the swirler vanes, (a) *basic* mesh, vs. (b) *optimized* mesh.

Chapter 4

Sensitivity analysis of swirling flows LES to fluid dynamics conditions

4.1 Motivation and methodology

Chapter 3 shows that the two LES codes used in this work predict that the unconfined swirling jet, generated by the LOTAR injector, undergoes bifurcation between two states (AJ-BB) which leads to different flow fields and different jet expansion angles. This bifurcation seems to depend on multiple numerical parameters (mesh, SGS model) but the analysis of results of chapter 3 has suggested that the parameter governing the flow response is the swirl ratio of the radial jet (Eq.(2.3)). The swirl ratio of the radial jet is representative of the total angular momentum of the radial jet for a given mass flow rate. This dependency is made clear by Fig. 3.21 in which the jet opening half-angle is plotted against the swirl ratio: for a swirl ratio above $S_r \approx 0.8$ the jet is in the BB state, while for S_r below ≈ 0.76 is in the AJ state.
This variation of the swirl ratio was related to the different numerical settings employed in the various simulations, which modified the mean velocity profile downstream of the radial swirler vanes. Numerical settings influenced the swirl numbers of the various jet as well as the flow split and the detachment dynamics of the central jet. The effects of such modifications are unknown and cannot be identified clearly from the analysis of chapter 3 because they all act on the flow at the same time.
The assumption that the AJ-BB bifurcation is related to the amount of swirl in the radial jet requires a further verification in a controlled environment: an additional numerical experiment is setup in this chapter, keeping all numerical settings constant and variating simply the fluid dynamics conditions of the jet. The target of this chapter is therefore to prove that it is possible to cause bifurcation in the LOTAR configuration by modifying the swirl ratio of the radial jet only, keeping all numerical parameters constant.
The existence of confined swirling flows exhibiting two or more possible states as a function of the swirl intensity, characterized by a different jet expansion angle, has already been studied experimentally in the past (see Chedaille et al. [46] or Beer and Chigier [8]) and recently (2007) by Vanierschot et al. [105] (as shown in chapter 3, the flow states of LOTAR

and of Vanierschot [105] show common, peculiar properties). Here the same experiment will be repeated numerically for LOTAR. The analysis is conducted as follows:

- In order to remove the dependence on the numerical settings, these are kept constant: YALES2 is used for all tests with SIGMA as SGS model and no slip walls.
- In order to better capture turbulence and the wall phenomena, the resolution is increased at the solid walls and in the whole simulation domain.
- In order to impose the desired fluid dynamics conditions for each of the jets of Fig. 3.6, the simulation domain is modified (Fig. 4.1) making possible to decouple swirl intensity from the swirler geometry. This allows to vary the swirl number continuously.
- In order to study hysteresis, the initial conditions are varied.

Results will confirm the assumption reached in chapter 3: a variation of O(10%) of the swirl ratio is able to cause the bifurcation that distinguishes the AJ from the BB states. Evidences of hysteresis are also included. All simulations performed in this chapter are itemized in table 4.1: the two basic simulations are named basic and high and they start with a zero velocity flow field while the hysteresis LES are named P X _ U (where X is the simulation number and U or D stands for the Up or Down part of the hysteresis loop respectively).

LES name	S (eq. 2.2) inner/outer jet	S_r (eq. 2.3) radial jet	initial condition	jet configuration
basic	0.12/ 0.4	0.75	zero velocity	AJ
high	0.12/ 0.4	0.84	zero velocity	BB
P1_U	0.12/ 0.4	0.84	basic	AJ
P1_D	0.12/ 0.4	0.75	high	BB
P2_D	0.12/ 0.4	0.60	P1_D	AJ
P3_D	0.12/ 0.4	0.75	P2_D	AJ

Table 4.1: First set of LES of the adjustable swirler case.

4.2 Mesh, boundary conditions and numerical settings

The original LOTAR CAD was modified to decouple the flow properties from the geometry of the device. This is achieved by removing the plenum and the swirlers from the domain (Fig. 3.3) keeping un-modified the diffusers and the bowls. This geometry is named *adjustable swirler* (Fig. 2.1 right). Instead of feeding the injector via the *plenum inlet* of Fig. 3.3, three inlets (corresponding to the inner, outer and radial jets) are placed downstream, just at the exit of the swirler vanes (Fig. 4.1). In Fig. 4.2 it is possible to see the various inlets corresponding to each vane (darker parts, clustered together in single boundary conditions) for the three different jets. This geometrical detail is kept since the presence/absence of the end walls had an impact on the bifurcation diagram (this test is not shown here).

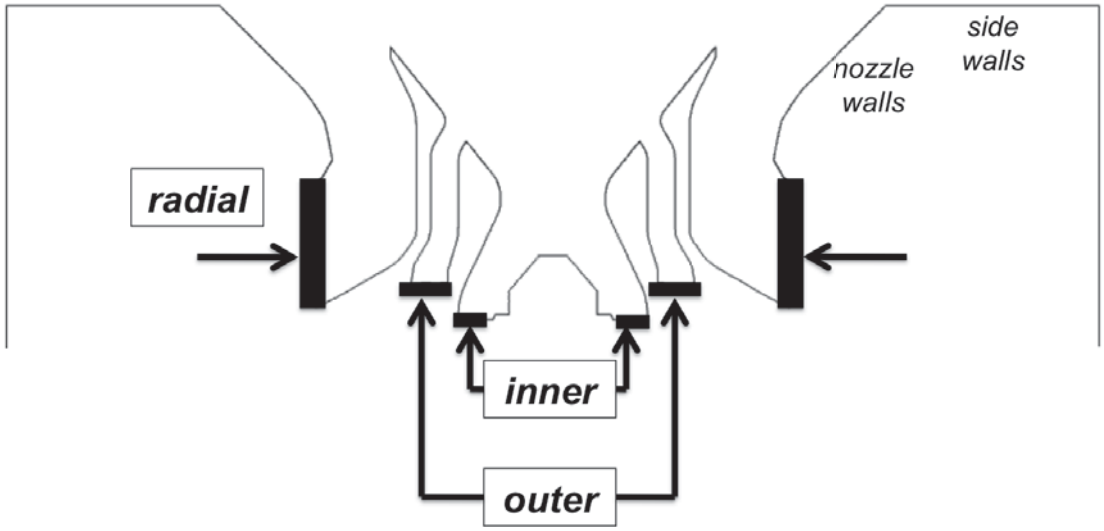

Figure 4.1: Inlet boundary conditions of the LOTAR adjustable swirler case, inside the swirler. Boundary conditions are imposed on the shaded sectors visible in figure and not at the inlet of the plenum which is not resolved anymore.

Geometry simplifications of swirlers are quite common in the literature because they make LES simpler and often allow to tune results since inlet velocity profiles can be adjusted as needed. At CERFACS, this practice is avoided since it requires to implement *ad-hoc* boundary conditions inside the swirler, something that is a different and somewhat *ad-hoc* exercise. In the present case, however, it has a clear intent: it allows to impose the desired swirl number, ratio and Reynolds number (i.e. mass flow rate) for each jet by changing the velocity profiles on the black lines of Fig. 4.1 which corresponds to the inlet sections of the adjustable swirler geometry.
The mesh is shown in Fig. 4.3-4.4. To ensure that the resolution is sufficient, the minimum cell size is 50 times smaller than the smallest element of the *basic* or *optimized* meshes employed in chapter 3. The smallest cells are located at the solid boundaries where a minimum cell size of $50\mu m$ is imposed, while, inside the swirler, elements size varies between $300\mu m$ and $400\mu m$ (Fig. 4.3). The mesh is then smoothly coarsened away from the swirler (Fig. 4.4), the cell size gradation (variation of the cell size in neighbor elements) has been limited to 1.3 and the cell aspect ratio to 2.

4.2.1 Boundary conditions

As in chapter 3, the swirler is mounted on a cylindrical box to mimic open atmosphere. Boundary conditions used in this chapter are the same shown in Fig. 3.3 (far field B.C.s) including the cooling film (Fig. 3.3 swirler B.C.s and Fig. 3.4). A coflow is added like in Fig. 3.3. Annex B shows that this coflow has a very limited effect on the results. Evidently, the plenum inlet in Fig. 3.3 is removed and replaced by three inlets (inner, outer and radial in Fig. 4.1). Boundary conditions are summarized in tables 4.2 and 4.3.

Target values of the new inlets introduced inside the swirler are summarized in table 4.3, the mass flow rate and a specific velocity profile (in terms of mean values), are imposed. The velocity profile is flat (a turbulent velocity profile), but no turbulence is injected. The no-slip boundary condition naturally damps the speed at the solid walls. A

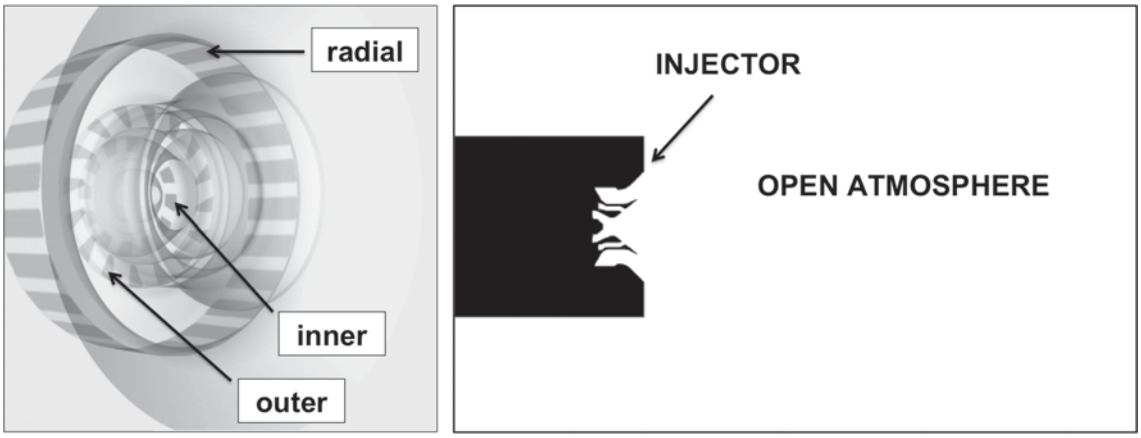

Figure 4.2: Left, Inlet boundary conditions of the LOTAR adjustable swirler case. The different vanes (darker parts) forming the inlet boundary conditions in the swirler, are visible. Right, sketch of the whole configuration of the adjustable swirler case. The jet generated by the swirler expands in the open atmosphere. Only the part in white is simulated.

Reference temperature = 270 [K]		
BC NAME	IMPOSED PROPERTY	TARGET VALUE
coflow	velocity	1 $[m/s]$
cooling film	mass flow rate	30.3 $[g/s]$
outlet	pressure	99000 $[Pa]$
walls	adherence, impermeability, adiabaticity	

Table 4.2: Imposed values for boundary conditions sketched in Fig. 3.3 (with the exception of *plenum inlet* which has been removed).

systematic study of the effects of the injected turbulence (which in the real configuration is generated inside the swirler vanes, a set of turbulent channels) goes behind the scope of this numerical experiment. However this small scale turbulence is supposed to have a limited influence on the large flow structures generated downstream by the swirler because of the different length scales involved. For each INLET of Fig. 4.1:

- the normal velocity component is imposed through the mass flow rate.
- The tangential velocity component is adjusted in order to get the desired swirl number or ratio: this component is the only one that is varied in the various simulations of table 4.1.
- The remaining velocity component is obtained by post-processing simulation YALES-SIGMA_O (this component is ≈ 0 for the inner and outer jets, while for the radial jet is $\approx 31[m/s]$). The choice of this third component is arbitrary since it is supposed to have only a second order effect on the overall jet response.

The swirl ratio (S_r) and the swirl number are evaluated at the same locations (S1, S2, S3) used in chapter 3 (Fig. 3.6). Note that the swirl ratio (S_r, Eq. 2.3) is used to measure the amount of swirl in the radial jet while the swirl number (S, Eq. 2.2) is used for the inner and outer jets, as described in section 3.3.1. The measured mass flow rates are in line

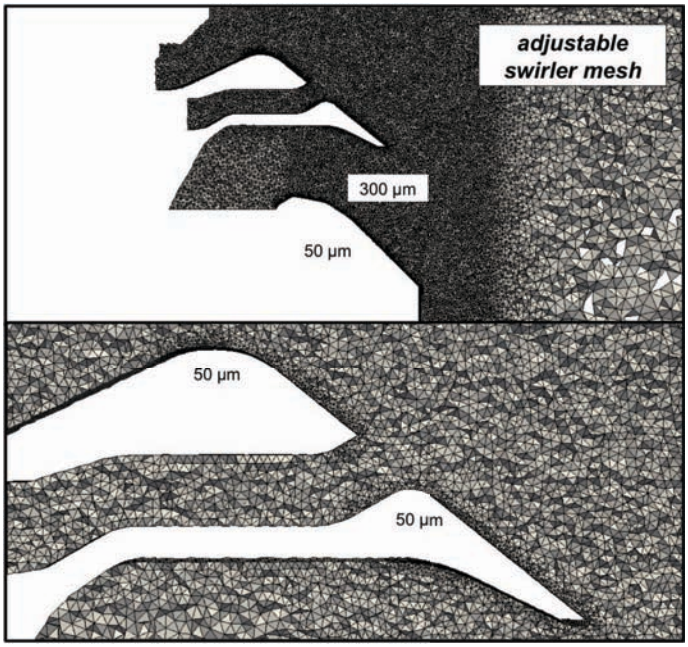

Figure 4.3: Adjustable swirler case mesh, zoom at the swirler.

SWIRLER Boundary Conditions, imposed velocity			
B.C. NAME	axial	tangential	radial
INNER	66.7 [m/s]	-21.5 [m/s]	1[m/s]
OUTER	64[m/s]	38.6 [m/s]	0.9[m/s]
RADIAL	31.6 [m/s]	simulation dependent	-57.9[m/s]

Table 4.3: Imposed boundary values inside the swirler, Fig. 4.1. The only passage that is changed for the simulations is the radial one (with the exception of LES outer as it will be shown later on), which is used to vary swirl intensity.

with the predicted values (error is O(4%) for the axial stage and O(0.5%) for the radial, see table 3.14). The measured swirl ratio of the radial jet and the tangential velocity imposed at the corresponding B.C. are in linear proportion in the whole range tested (Fig. 4.5). This is linear correspondence is a clear result of the high mesh resolution in the radial swirler, a too coarse mesh would have cause a different swirl ratio for the same incoming tangential velocity (determined by the swirler vane angle) as already experienced in chapter 3.

4.2.2 Numerical Settings

The simulations of table 4.1, use the same code (YALES2), SGS model (SIGMA), numerical settings and wall treatment (no-slip solid boundaries). The simulations differ only because of the fluid dynamic properties imposed at the three inlets of the swirler (table 4.3) and of the initial conditions.

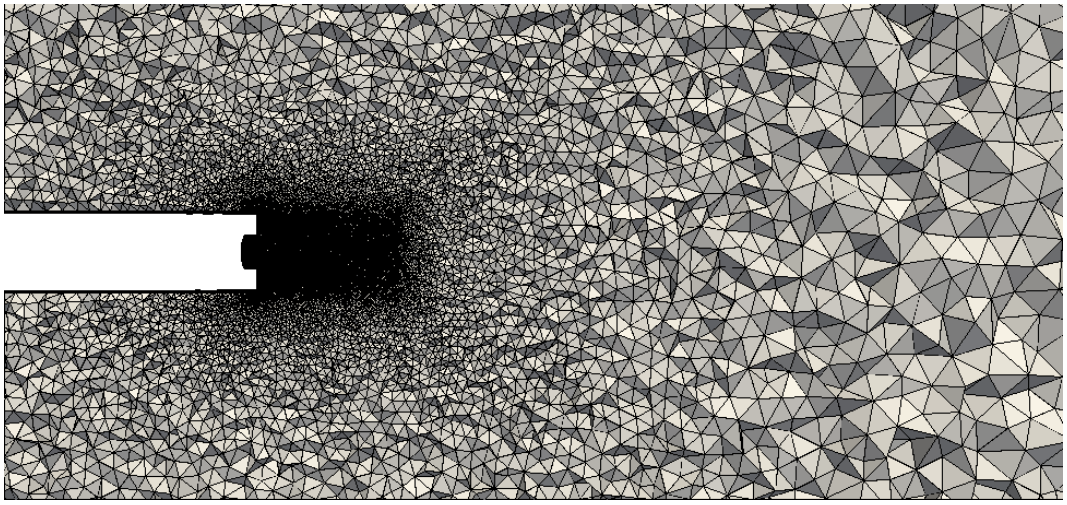

Figure 4.4: Adjustable swirler case mesh, far field.

JET	mass flow rate	swirl number or ratio
INNER	6.5 [g/s]	0.12 (Eq.2.2)
OUTER	9.1 [g/s]	0.4 (Eq.2.2)
RADIAL	86.4 [g/s]	simulation dependent (Eq.2.3)

Table 4.4: Measured mass flow rate and swirl ratio for LES of table 4.1.

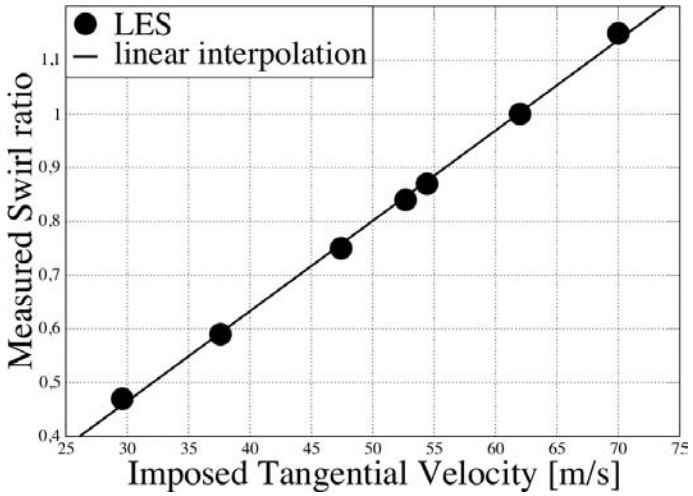

Figure 4.5: Swirl ratio (Eq. 2.3) of the radial jet plotted against boundary tangential velocity imposed at the radial B.C. in Fig. 4.1. The continuous line is the linear interpolation of the points.

4.3 Simulations Quality

LES quality is assured by monitoring multiple sensors: the wall distance nondimensionalized by the boundary layer thickness, the y^+ values, the ratio between laminar and turbulent viscosity and the Pope criterion [89] (ratio of resolved turbulent kinetic energy to resolved plus SGS turbulent kinetic energy, Eq. (4.1)). The values of y^+ (evaluated

at the cell baricentrum) are below 10 everywhere except downstream of the swirler vanes because of the high jet velocity (Fig. 4.6).

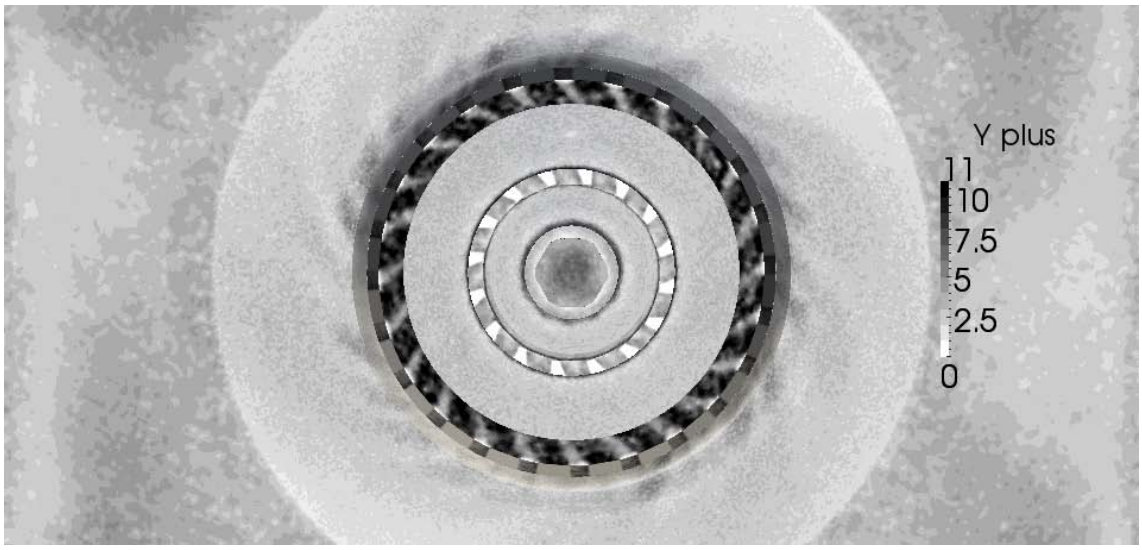

Figure 4.6: Mean y^+ values for LES basic of table 4.1. The swirler surface is seen from the open atmosphere.

The ratio of turbulent to laminar viscosity is low (Fig. 4.7 right and Fig. 4.8), while the Pope criterion [89]:

$$Pope = \frac{k_{res}}{k_{res} + k_{sgs}}, \tag{4.1}$$

is everywhere higher than 0.9 in the proximity of the swirler and equal to 1 inside the well resolved jet (Fig. 4.7 left). Resolved turbulence, k_{res}, is evaluated as $\frac{1}{2}\sum_{i=1}^{3}(u_i{}^2)$ where u_i is the Reynolds decomposition of the velocity component u_i. Subgrid scale turbulence is evaluated as [94]:

$$k_{sgs} = (\frac{\nu_t}{C_M \Delta})^2 \tag{4.2}$$

where $C_M = 0.069$ and Δ is estimated as the cubic root of the elements volume.

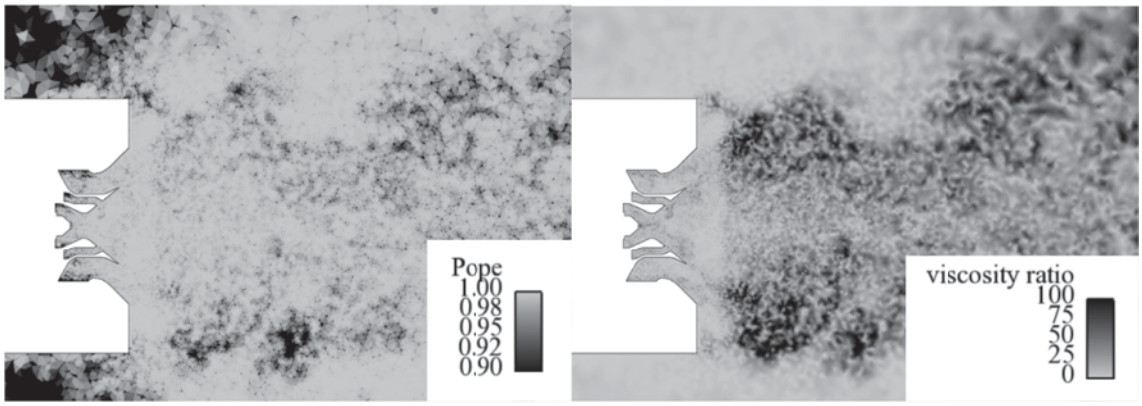

Figure 4.7: Snapshots of ratio of turbulent over laminar viscosity and Pope criterion, Eq. (4.1), for LES basic of table 4.1.

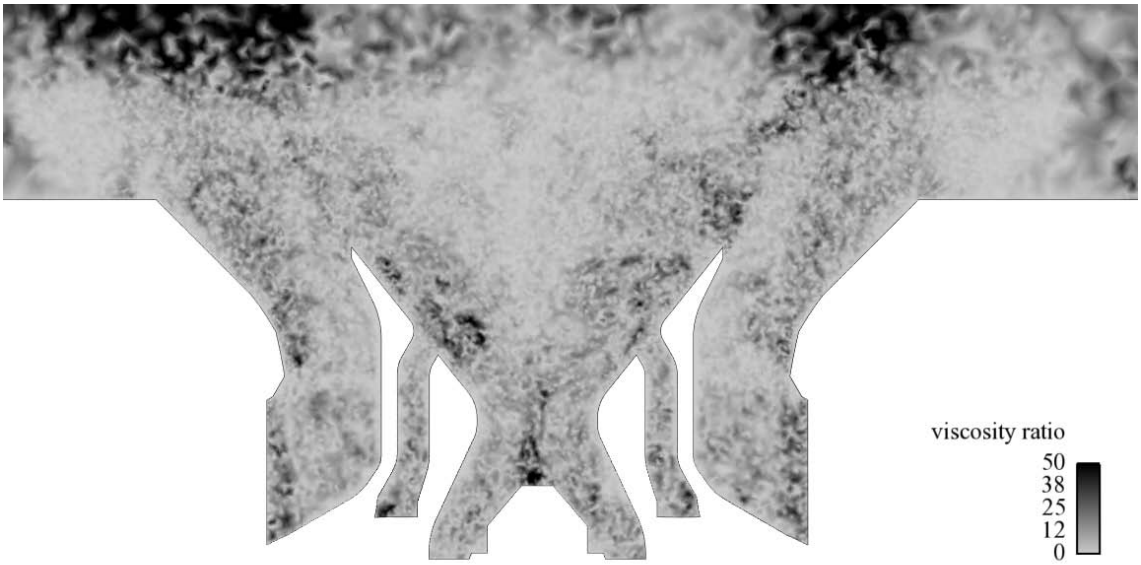

Figure 4.8: Ratio of turbulent over laminar viscosity of LES basic of table 4.1.

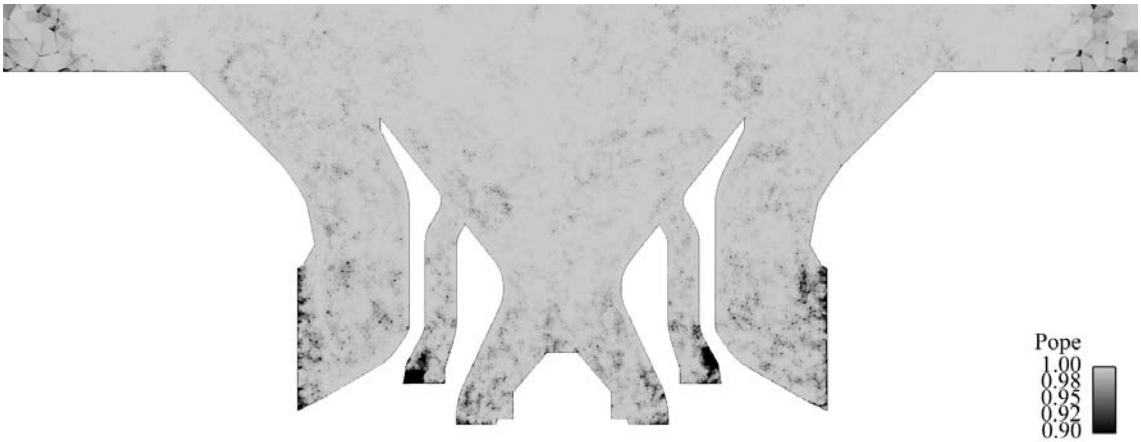

Figure 4.9: Pope criterion of LES basic of table 4.1.

All simulations show a P over ≈ 0.9 in the swirler, with the exception of some localized zone at the swirler inlets, since turbulence is not injected in the simulation domain and it does not have time to be produced by the flow (so $k_{res} \approx 0$, Fig. 4.9).

4.4 Simulation times and convergence

All statistics of LES of table 4.1 were collected after a period of 0.030 [s] and averaged for at least 0.004 [s] equivalent to ≈ 4 flight through times (considering a length scale of twice the injector diameter, $\approx 2D \approx 0.1[m]$, and a convective velocity of $\approx 100[m/s]$). Fig. 4.10 shows the time evolution of volume-average kinetic energy of the **basic & high** simulations of table 4.1. The kinetic energy is evaluated on a box big enough to fully

contain the recirculation bubble of the **high** case (Fig. 4.11) which is the largest observed. This choice is motivated by the fact that to obtain the convergence of kinetic energy in the whole simulation domain (inside the whole cylindrical box used to mimic open atmosphere) it requires a simulation time of $\approx 0.3[s]$ (so 300 simulations for each configuration) and by the fact that the far field has little influence on the jet, as shown in appendix B.

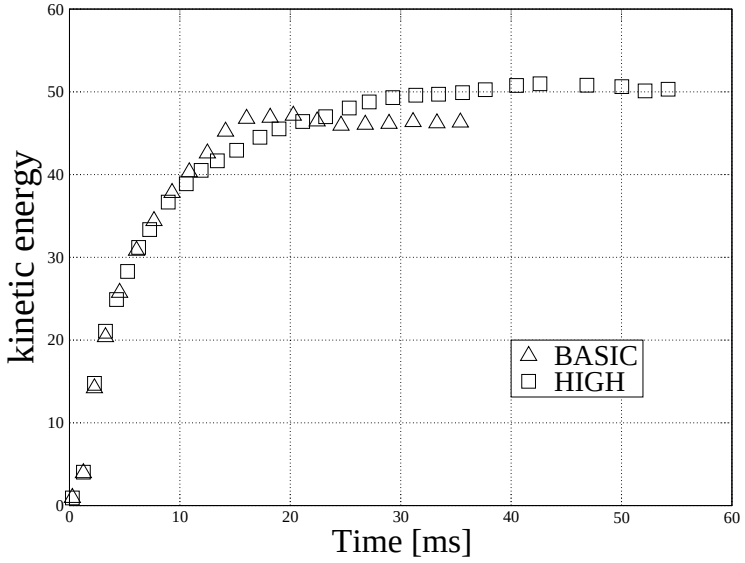

Figure 4.10: Kinetic energy evolution for simulations **basic, high & outer** of table 4.1.

To go from one of the LES of table 4.1 to another one (with a different set of B.C.s), the swirl ratio imposed at the radial boundary condition is varied continuously (unless LES is re-initialized). The acceleration rate of the tangential velocity used for these transition phases is $O(1000)[m/s^2]$. Even if this value is $O(100)$ times the gravitational acceleration, a slower acceleration/deceleration rate would cause a slower convergence to the desired target value. However, two things should be underlined. First, this type of injector is susceptible to acoustics. The characteristic frequency of these waves is $O(100)[Hz]$ with a oscillation in terms of flow speed that could reach $O(10)[m/s]$ [88], which leads to an acceleration rate of $O(1000)[m/s^2]$. Second, stiff transitions are not un-common in LES: a switch from an SGS model to another would cause an even stiffer change in the flow field. Therefore such acceleration rate can be considered as consistent with the common fluid dynamics and/or numerical conditions.

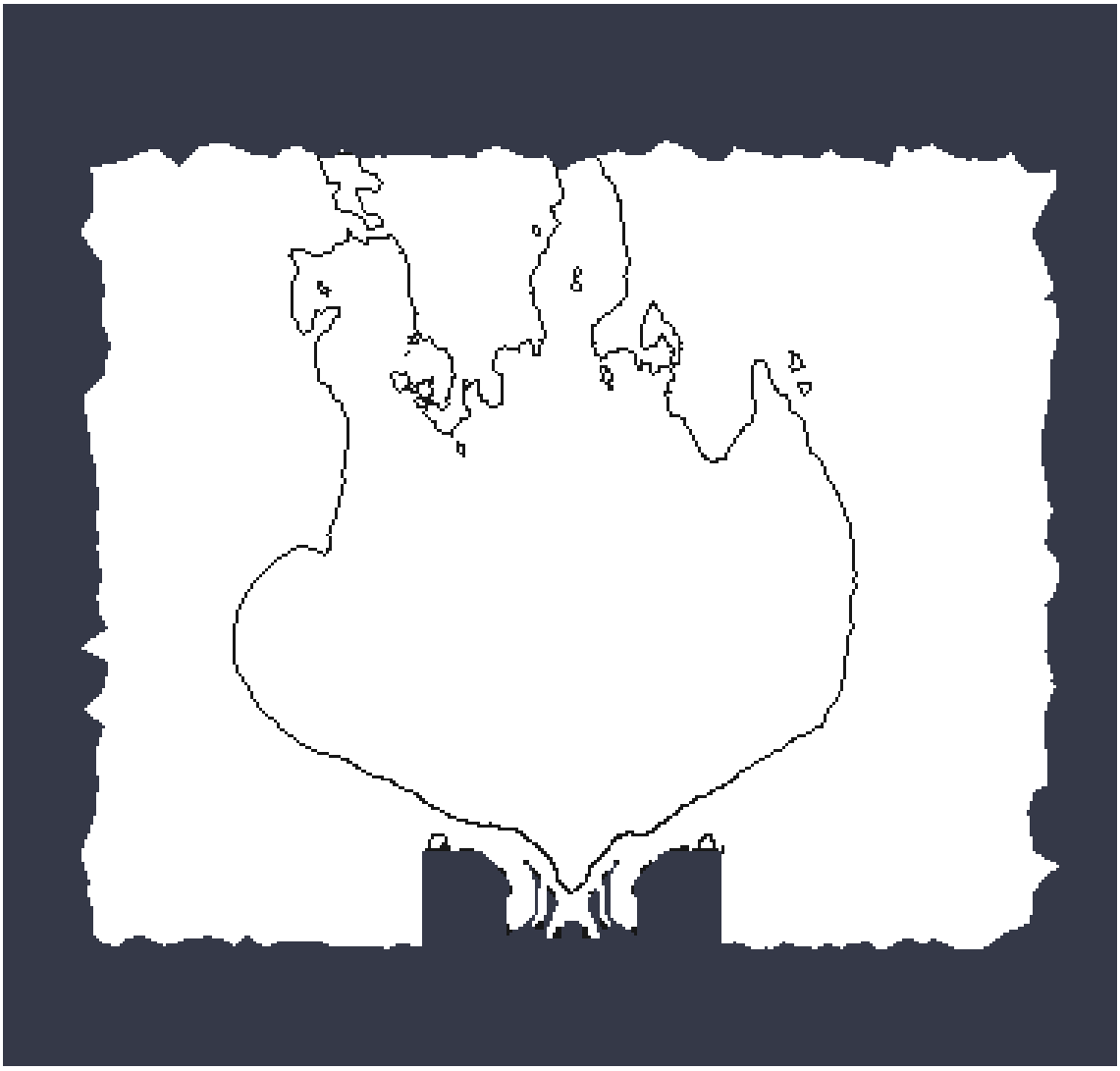

Figure 4.11: White zone: box used to evaluate the jet s kinetic energy. The black line is the zero axial velocity isoline for simulation high of table 4.1.

4.5 Basic configurations

Two simulations are first tested for two different radial jet swirl ratios. The swirl introduced by the inner and outer jets is kept constant ($S = 0.12$ and $S = 0.4$ respectively, the swirl number S, Eq. 2.2, is always used for the two co-axial jets). The first simulation (basic) uses a swirl ratio (the swirl ratio S_r, Eq.2.3, is always used for the radial jet) of the radial jet similar to simulation YALES-SIGMA_O; the second (high), uses a swirl ratio 10% higher ($S_r = 0.84$). The characteristics of these two simulations are summarized in table 4.5, while their flow fields and CTRZs are shown in Fig. 4.12.

LES name	S (eq. 2.2) inner/outer jet	S_r (Eq. 2.3) radial jet	jet configuration
basic	0.12/ 0.4	0.75	AJ
high	0.12/ 0.4	0.84	BB

Table 4.5: First set of LES of the adjustable swirler case.

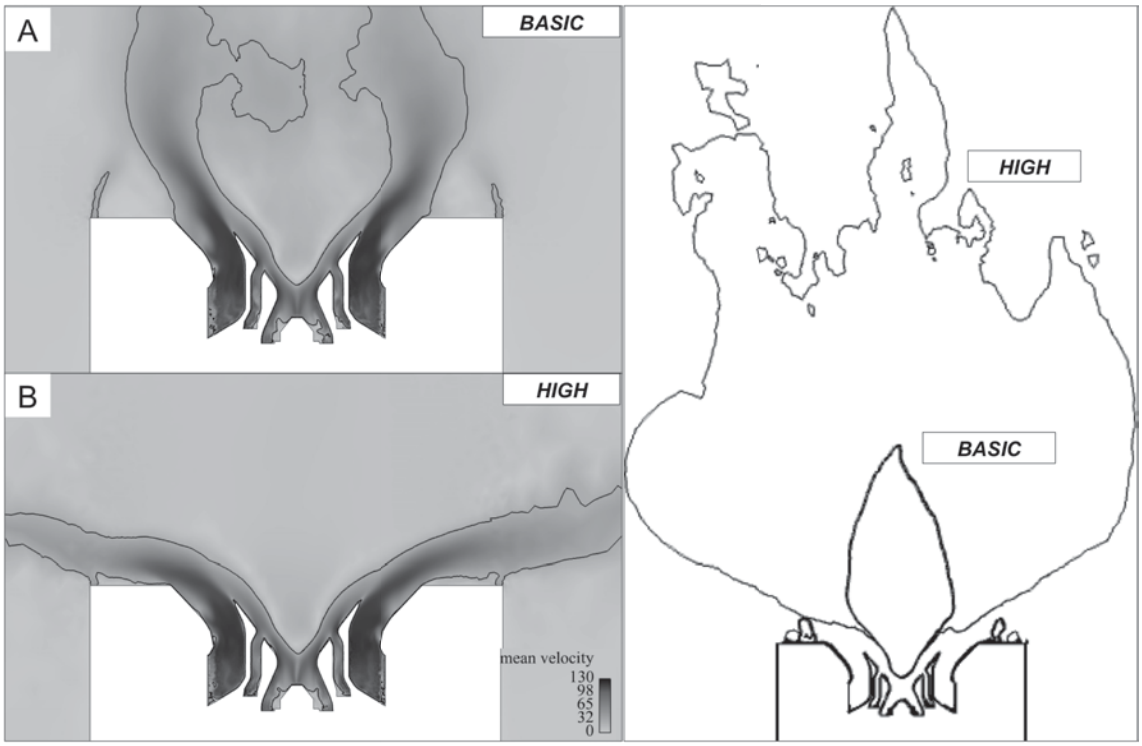

Figure 4.12: A-B: flow fields and velocity isoline ($U = 20[m/s]$) of simulations *basic* & *high* of table 4.5. CTRZs (zero axial velocity isoline) of these simulations are shown in the picture on the right.

The flow configuration of the *basic* case is characterized by a CTRZ smaller than one injector diameter (Fig. 4.12), a high tangential velocity (Fig. 4.13), a high sub-pressure ($P_D \approx 0.44$) and high turbulence intensity inside the CTRZ (Fig. 4.14). On the contrary, the flow configuration of the *high* case is characterized by a CTRZ which is several injector diameters wide (Fig. 4.12), a strong reduction of tangential velocity inside the CTRZ (Fig. 4.13) and a reduced sub-pressure ($P_D \approx 0$) as well as a negligible turbulence intensity inside

the CTRZ (Fig. 4.14). The jet of *basic* LES is therefore in the AJ state while the jet of the *high* case is in the BB state: an increase of 10% of the swirl ratio of the radial swirler jet (from $S_r = 0.75$ to $S_r = 0.84$) is enough to induce a bifurcation of the flow from AJ to BB states. Note also that the flows in the fixed swirler case of chapter 3 (i.e. Figs. 3.10-3.15 & Figs. 3.17-3.20) are similar to the flows in the adjustable swirler case (Figs. 4.13 and 4.14), showing that replacing the full swirler computation by an equivalent set of boundary conditions has a limited impact on the flow organization, as long as both jets are in the same state (AJ or BB).

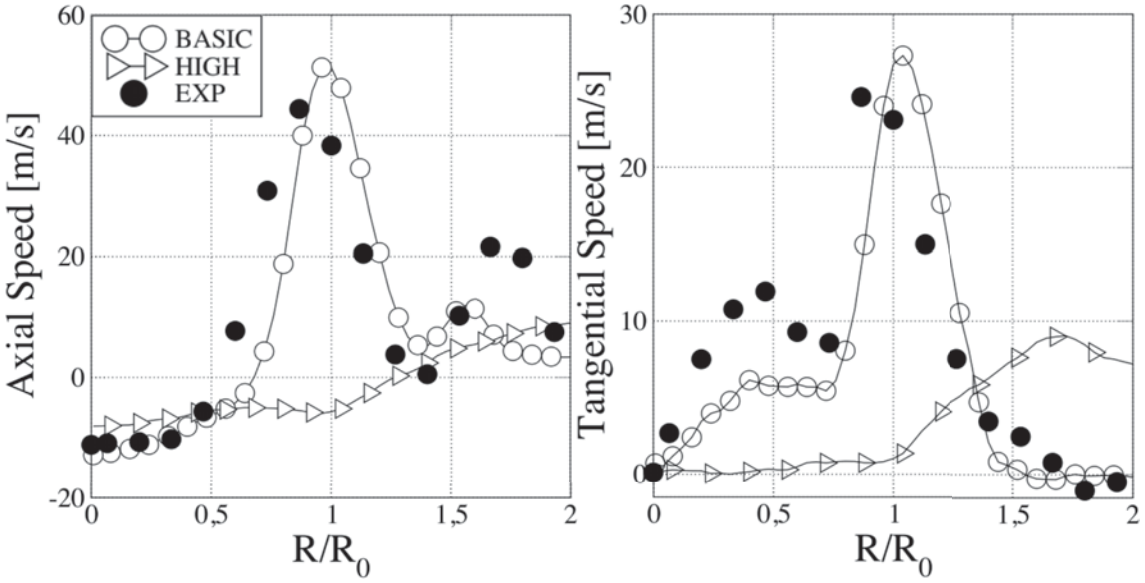

Figure 4.13: Flow velocities plotted against normalized radial positions for simulations of table 4.5. Measurements are taken $0.5R_0$ ($15[mm]$) downstream of the swirler end plate.

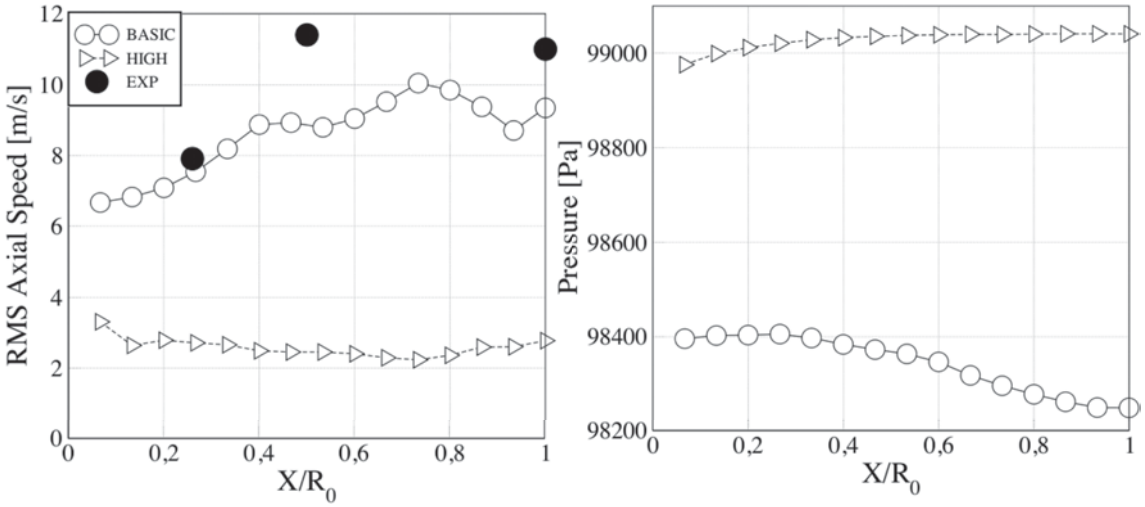

Figure 4.14: Axial velocity RMS and pressure distribution measured along the centerline of the geometry. Results are plotted against normalized axial distance (X/R_0) from the swirler end plate for simulations of table 4.5.

4.6 Pressure fields and flow patterns

Fig. 4.15 shows the pressure fields of simulations of table 4.5 where the different flow states are visualized by the mean pressure distribution. The jet attachment to the side walls (see Fig. 4.1) of simulation *high* is made evident by a localized subpressure in that zone, a phenomenon not observed for LES *basic* (in which a negative pressure gradient is present from the side wall toward the CTRZ core).

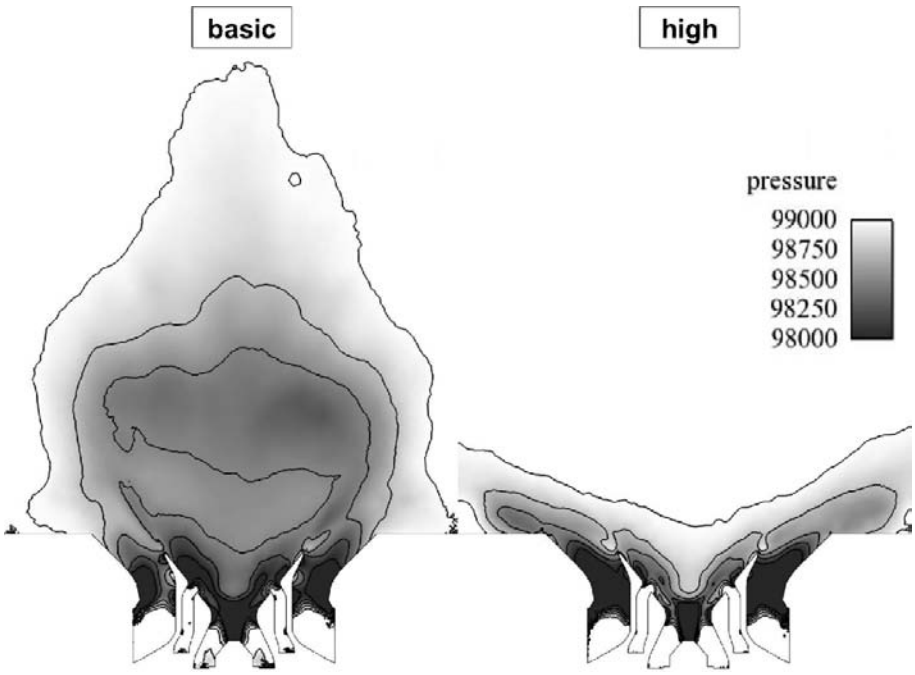

Figure 4.15: Mean pressure field for simulations of table 4.1.

An interesting feature of the *basic* simulation is the dynamics of the central jet, which remains attached. Comparing Fig. 4.16 and Fig. A.1, it is evident that an attached central jet can be obtained despite a low swirl number in the inner and outer jets, see tables 4.3 and 3.11: the detachment dynamics of the central jets are related to the SGS model and to a locally poor mesh resolution, as explained in appendix A, and not to the swirl numbers of the central jet.

To visualize the flow pattern, a passive scalar (the numerical equivalent of the smoke or dye used in the experimental literature on the subject) is injected at the radial inlet. Fig. 4.17 shows the instantaneous distribution of a passive scalar (named R) for simulations *basic* & *high*: the jet direction is made evident by the convection of R.

4.6.1 Comparison with experimental data

Comparison with experimental data is shown here just as a reference for simulations *basic* and *high*, Figs. 4.18, 4.19, 4.20. The *basic* LES shows a very good comparison with experimental data, with the jet opening half-angle matched by LES. The length of the recirculation zone, see Fig. 4.18 third plane, is well predicted by LES.

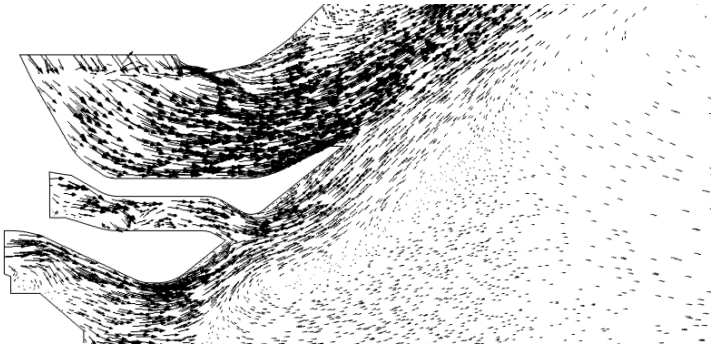

Figure 4.16: Velocity vectors, simulation **basic**.

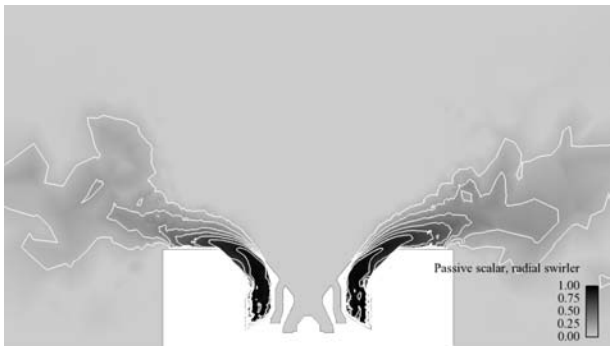

(a)

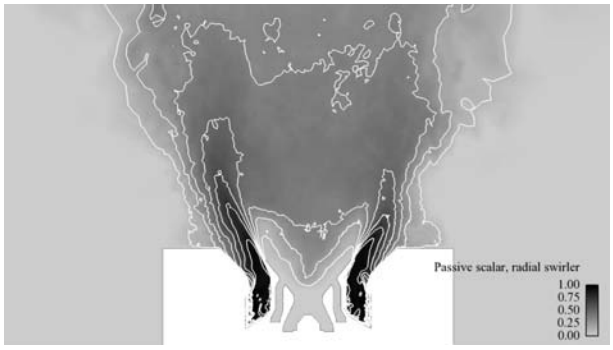

(b)

Figure 4.17: Distribution of the passive scalar R (injected at the radial inlet of Fig. 4.1) **high** (a) vs. **basic** (b).

Differently from the *basic* LES, the *high* simulation forecasts a BB state: results are bad. Note that the true value of the swirl ratio in the experiment is unknown. When setting up this simulation, using a low ($S_r = 0.75$) or an high ($S_r = 0.84$) swirl value is clearly an uncertain parameter. The results of Fig. 4.18 to 4.20 show that this uncertain parameter actually controls a very strong bifurcation and that only the *basic* case corresponds to the experimental data since the flow is in the same state (AJ).

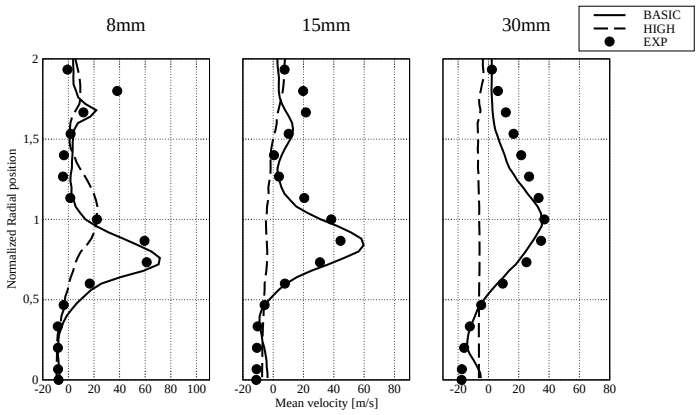

Figure 4.18: Axial velocity for simulations *basic* and *high* of table 4.1, radius for normalization $R_0 = 30[mm]$.

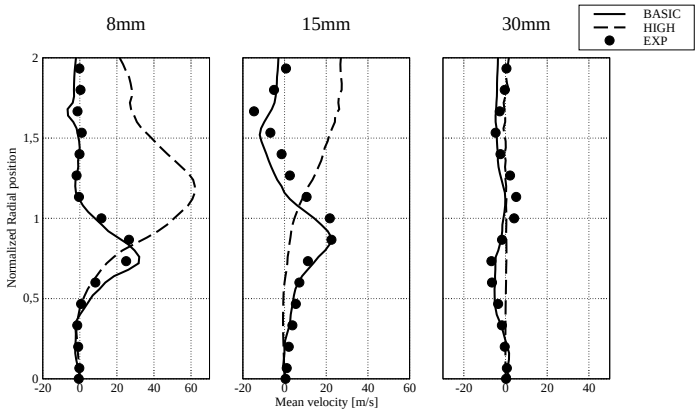

Figure 4.19: Radial velocity for simulations *basic* and *high* of table 4.1, radius for normalization $R_0 = 30[mm]$.

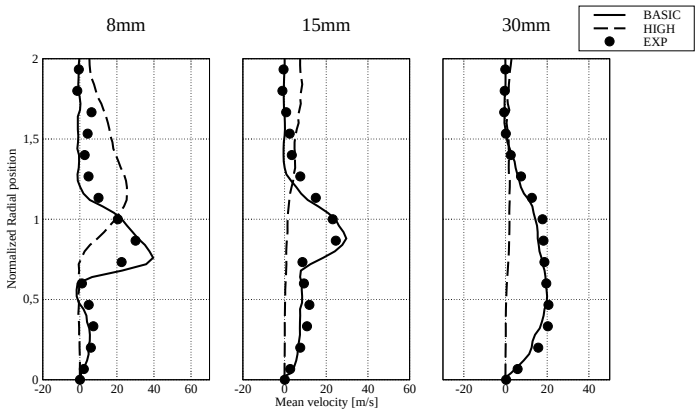

Figure 4.20: Tangential velocity for simulations *basic* and *high* of table 4.1, normalization radius $R_0 = 30[mm]$.

4.6.2 PVC

The PVC can be identified in simulations *basic* and *high* by injecting a second passive scalar (named C) at the pilot injector, in a central position inside the innermost bowl (Fig.4.21a). By monitoring the pressure signal at three different locations (Fig.4.21b), it is possible to identify the frequency of the PVC, which is $\approx 2500Hz$ for both simulations.

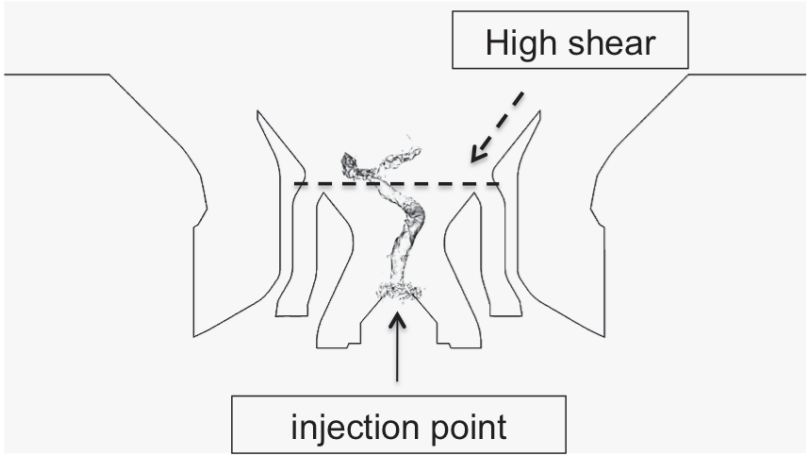

(a) PVC

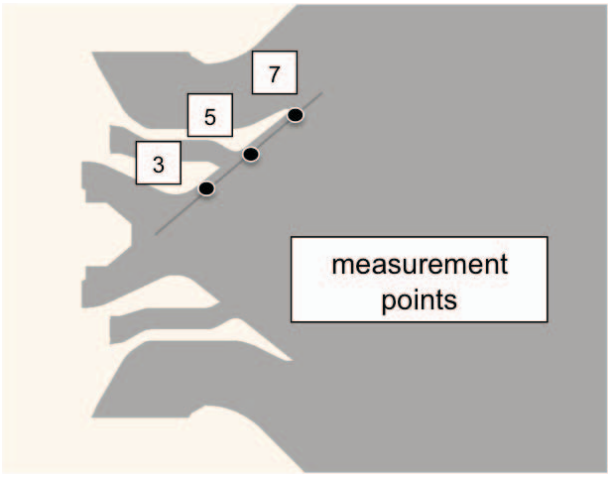

(b) Measurement location of the the pressure signal of Fig. 4.22.

Figure 4.21: (a) Passive scalar C injection point and PVC (made evident by a passive scalar isosurface) of simulations *basic* and *high* of table 4.1.

Fig. 4.22 shows the Discrete Fourier Transform of the pressure signal taken at the different points.

The PVC extends until the position where the inner and outer counter-rotating jets merge (Fig. 4.23). Visually (Fig. 4.24) and from the spectrum of the pressure signal at three different locations (Fig. 4.22) is possible to determine the size of the PVC which ends where the inner and outer counter-rotating jets merge in a single stream (Fig. 4.23). Here, because of the high shear, the *numerical smoke* (the passive scalar C, which evidently can

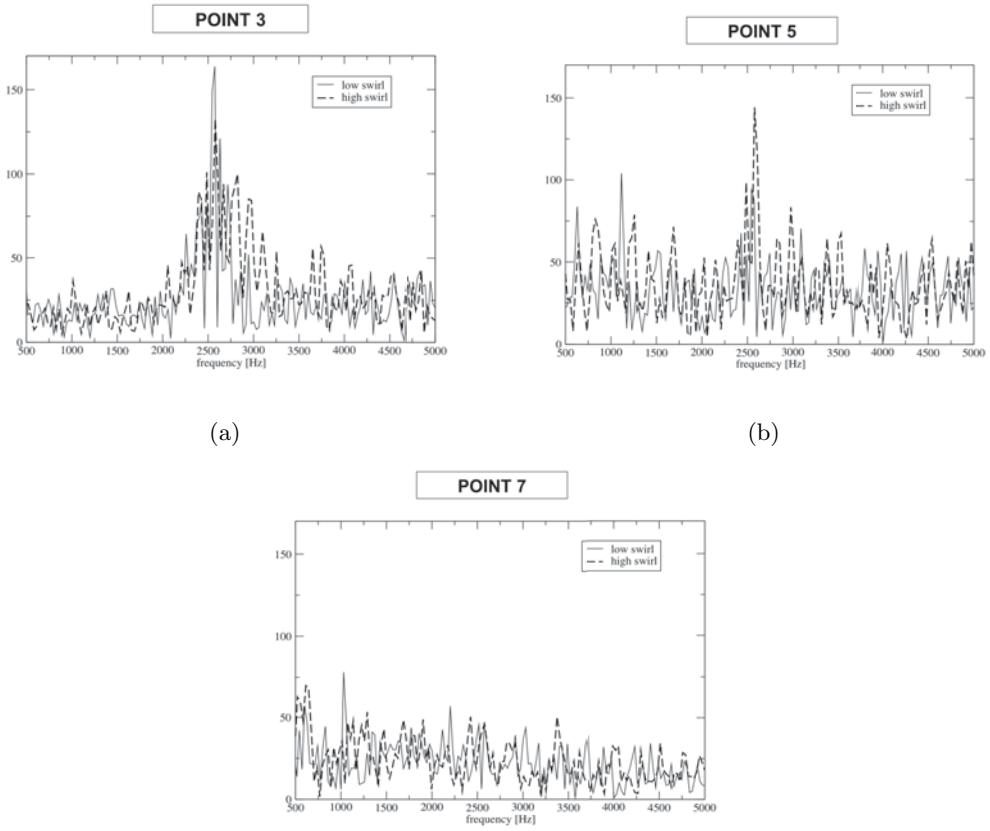

Figure 4.22: Discrete Fourier transform of the pressure signal of simulations *basic* and *high* of table 4.1.

only be spread by the flow) is diffused by turbulence everywhere and the *small tornado* is destroyed. Fig. 4.25 and Fig. 4.26 show the axial cut equivalent to points of Fig. 4.21, at the same time instant: the PVC is clearly destroyed at point 7 (Fig. 4.25c and Fig. 4.26c) with the turbulent diffusion of the passive scalar. As shown in this section, the dynamics of the PVC are similar in the *basic* and the *high* simulations: in this configuration the PVC is somehow independent of the CTRZ (which changes significantly with the jet configurations). This phenomenon can be explained with the fact that the PVC is confined inside the innermost bowl of the swirler. As a consequence, its dynamics are controlled only by the inner axial jet which does not change in the two configurations considered. The Strouhal number (S_t) of the PVC corresponding to a precession frequency of $f = 2500Hz$ is:

$$St = \frac{f\ D^3}{Q} = 0.49 \tag{4.3}$$

where Q = flow rate $= 0.005[m^3/s]$ and D = flow diameter $= 0.01[m]$.

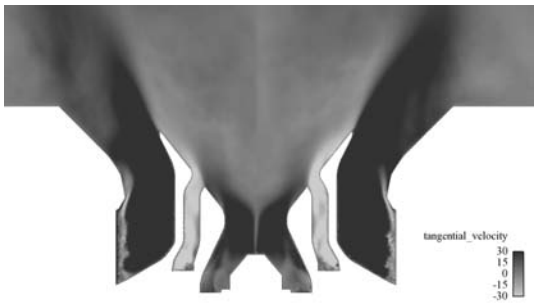

Figure 4.23: Tangential velocity of simulation *basic* of table 4.1.

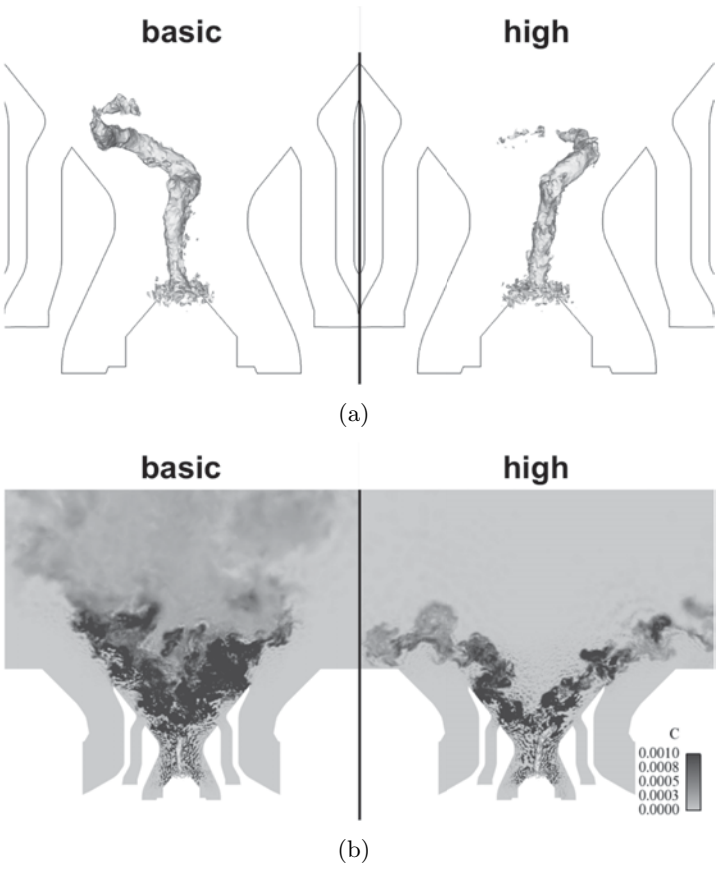

Figure 4.24: PVC in simulations *basic* and *high* of table 4.1 visualized by a passive scalar C isosurface (a). Passive scalar C field (b).

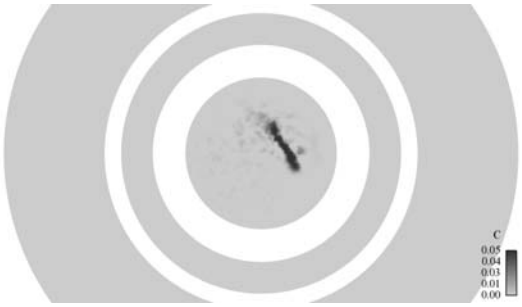

(a) Point 3 (Fig. 4.21) plane

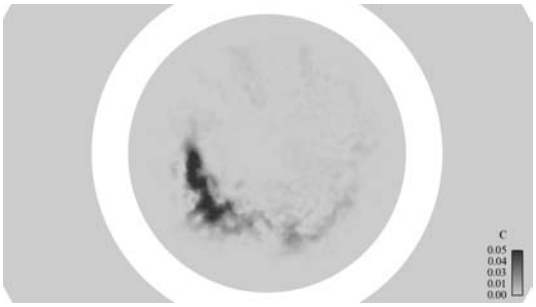

(b) Point 5 (Fig. 4.21) plane

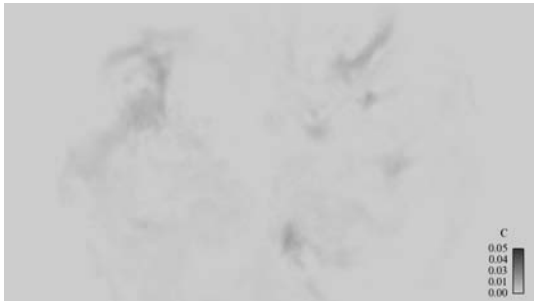

(c) Point 7 (Fig. 4.21) plane

Figure 4.25: PVC, made clear by the passive scalar C, at three planes equivalent to points of Fig.4.21, for simulation *high* of table 4.1.

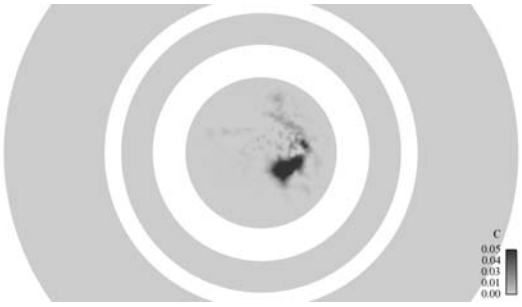

(a) Point 3 (Fig. 4.21) plane

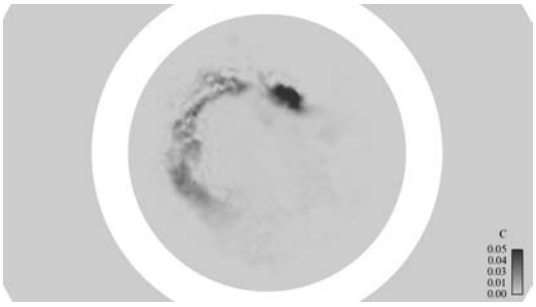

(b) Point 5 (Fig. 4.21) plane

(c) Point 7 (Fig. 4.21) plane

Figure 4.26: PVC, made clear by the passive scalar C, at three planes equivalent to points of Fig.4.21, for simulation *basic* of table 4.1.

4.7 Evidences of hysteresis

In order to verify if hysteresis is also present in the adjustable swirler case and if it is controlled by the swirl level, a second set of tests is performed by changing continuously the swirl ratio of the radial jet while the amount of swirl of the remaining co-axial jets is kept constant at $S = 0.12$ and $S = 0.4$ respectively.
LES are cast in two groups named path A & B. Each path corresponds to a succession of simulations performed with increasing or decreasing values of swirl.

- Path A begins with LES *basic* and the following simulation is obtained by increasing the swirl ratio of the radial swirler jet to the swirl level of LES *high*.
- Path B begins with LES *high* and the successive simulations are obtained by decreasing the swirl ratio of the radial swirler jet except for the final simulation ($P3\_D$) in which the swirl level is brought back to LES *basic* ($S_r = 0.75$).

The investigation is limited to the range $0.6 < S_r < 0.84$, around the working condition of $S_r \approx 0.75$, which is of interest for the present study and which is sufficient to close the hysteresis loop. Above $S_r = 0.84$ no flow change is expected anymore and this zone is not explored. Below $S_r = 0.6$ a transition to an UJ state similar to the one shown in Fig. 2.9 is expected, however such zone corresponds to a very a low swirl level, far from the working condition of the device.
Paths A & B are summarized in table 4.6, while the swirler transition map is shown in Fig. 4.27. The swirler bifurcation diagram (Fig. 4.27) differs from the one of Vanierschot et al. [105] (Fig. 2.10): this does not come as surprise since each transition map is dependent on the particular flow and geometry examined (as made evident in Vanierschot and Van Den Bulck [106], who analyzed the influence of the nozzle geometry on the bifurcation diagram of their original experiment [105], presented in section 2.2.3).

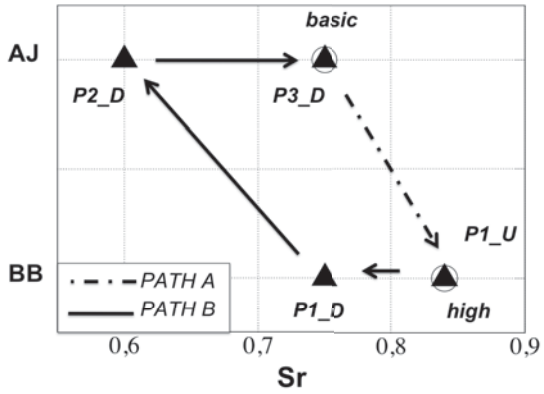

Figure 4.27: Transition map of the aeronautical swirler, adjustable swirler case, where the various simulations and flow states are plotted against the swirl ratio (Eq. 2.3). Circles are LES of path A (which starts with LES *basic*) while black triangles are LES of path B (which starts with LES *high*). The hysteresis loop is closed.

LES name	S_r (eq. 2.3) radial jet	initial condition	jet configuration
P1_U	0.84	basic	AJ
P1_D	0.75	high	BB
P2_D	0.60	P1_D	AJ
P3_D	0.75	P2_D	AJ

Table 4.6: Characteristics of LES of Path A & B.

LES along path A are characterized by multiple bifurcations. At a swirl ratio of the radial swirler jet of 0.84 (simulation P1_U) the jet bifurcates from AJ to a state which is not AJ or BB. All flow properties are in an intermediate level between the AJ and BB states and the central vortex core which characterizes the AJ state is still present but weaker, exactly as described in the Vanierschot case [105] of section 2.2.3. The flow can be therefore classified as a Weak axial Jet (WJ). However, this flow state is unstable and transitory: after a period of $0.05[s]$ the flow bifurcates to the BB state. Transitions change pressure and turbulence intensity distributions (Fig. 4.28) as well as the shape of the CTRZ (Fig. 4.29) which expands both radially and axially after each bifurcation.

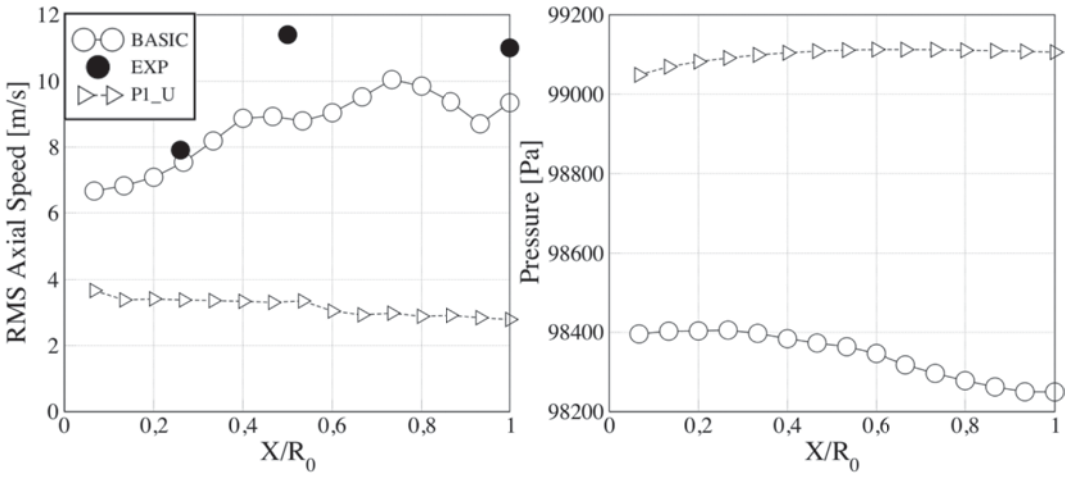

Figure 4.28: Axial velocity RMS and pressure deficit (Eq.(2.9)) measured along the centerline of the geometry. Results are plotted against normalized axial distance (X/R_0) from the swirler end plate, for simulations of path A, table 4.6.

On the contrary, a decrease of the swirl ratio of the radial swirler jet from the value of 0.84 triggers a transition in LES of path B only at $S_r = 0.60$ (simulation $P2\_D$): at this swirl level the jet detaches from the external side walls and bifurcates back to the AJ state (Fig. 4.29-4.30).

The adjustable swirler case results, summarized in Fig. 4.27, show that the aeronautical swirler flow field (with a swirl ratio of the radial jet close to 0.8, see section 3.3) is close to multiple bifurcations (AJ-WJ, WJ-BB, BB-AJ) and this confirms the assumptions proposed in chapter 3.

Two stable flow states (AJ-BB) can appear as a function of the swirl level of the jet and of the initial conditions. Results obtained in the adjustable swirler case are consistent with results of the fixed swirler configuration. They show that the swirl ratio of the radial jet

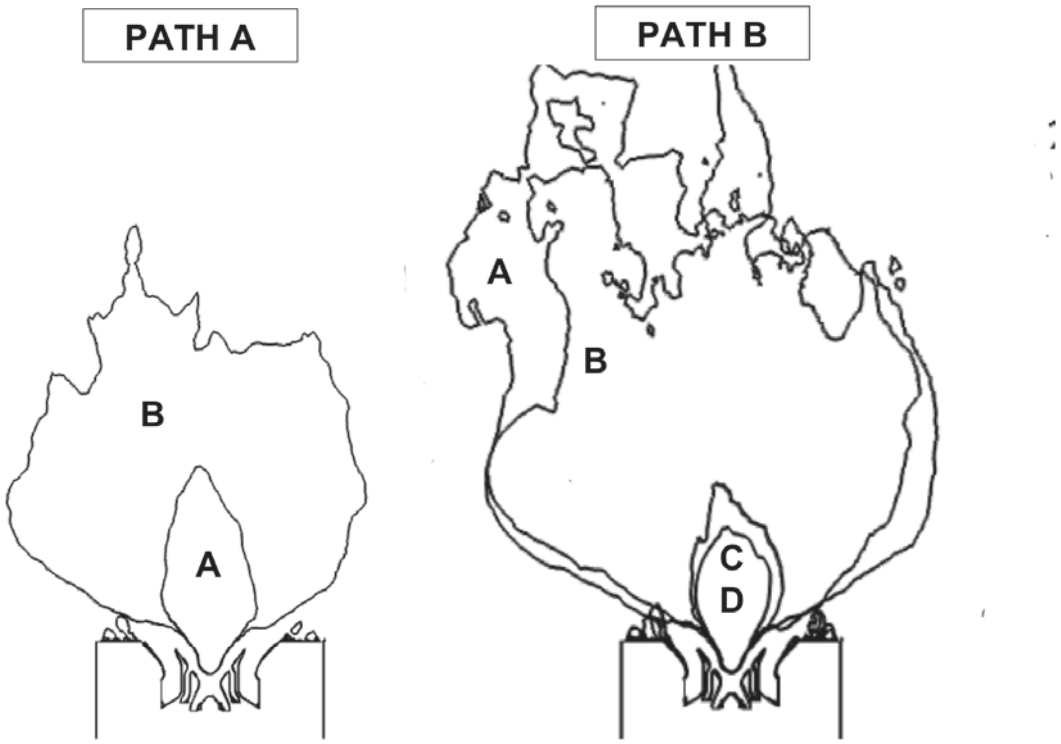

Figure 4.29: Path A: CTRZs of LES *basic* (A), $P1\_U$ (B). Path B: CTRZs of LES *high* (A), $P1\_D$ (B), $P2\_D$ (C), $P3\_D$ (D).

of the fixed swirler case $(0.74 - 0.82)$ studied in chapter 3 is very close to the bifurcation threshold obtained in the adjustable swirler case: between $0.75 < S_r < 0.84$, the flow is bistable. LES senses this property and becomes sensitive to multiple parameters such as grid refinement or SGS model. As a result, characterizing swirling flows using LES can become difficult when the flow is in such conditions. Obviously, performing LES for $S_r < 0.75$ or $S_r > 0.84$ would have been much simpler because the flow is not bistable in these regions. Around $S_r = 0.8$ much more caution must be used since LES becomes much more sensitive , like the real flow does.

4.8 Conclusions

The first part of this thesis has shown that LES of industrial swirling jets can be an extremely difficult task since small flow modifications can trigger large flow re-configurations near critical flow conditions and small changes in the numerical setup of LES are sufficient to induce violent changes of flow state.
In the case examined here, for an adjustable swirler case, LES results demonstrate that the main parameter controlling the flow state is the swirl level of the radial jet. Bifurcations occur when swirl is changed by modifying inlet conditions or when it is changed by a modification of the LES grid or SGS model. This hypothesis was verified in chapter 4 by using a high-fidelity LES to simulate an adjustable swirl device where the amount of swirl in the flow can be controlled and modified easily. These bifurcations, which appeared to be due to uncontrollable errors in LES, were reproduced in a controlled environment where swirl

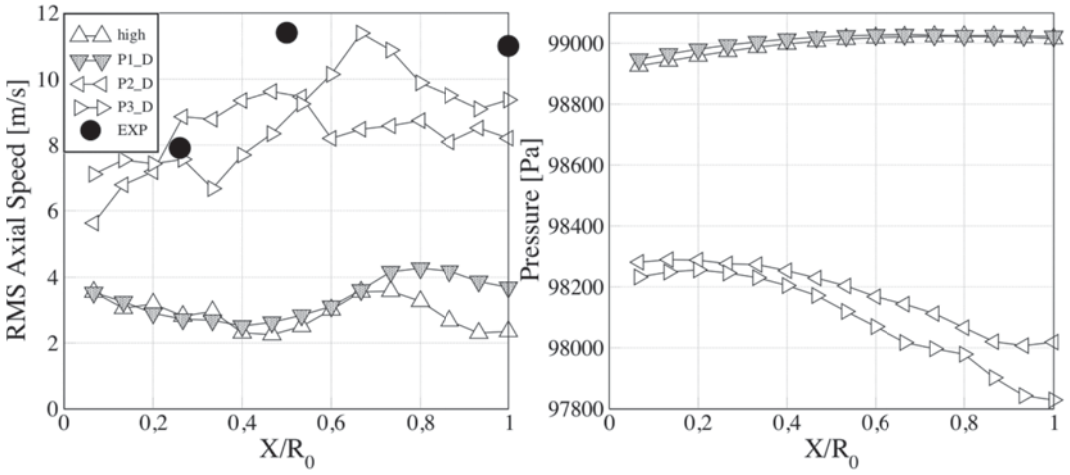

Figure 4.30: Axial velocity RMS and pressure distribution measured along the centerline of the geometry. Results are plotted against normalized axial distance (X/R_0) from the swirler ending plate, for simulations of path B, table 4.6.

was varied continuously. Two flow states were obtained and characterized based on the strength of the central, coherent, turbulent, vortex core associated with vortex breakdown. They are:

- a free Axial Jet (AJ) in which the central vortex core is not (or only weakly, like in simulation *basic* of table 4.1) influenced by the presence of confinement and behave like a free swirling jet,
- a Blasted Breakdown jet (BB), in which the central vortex core, made evident by *high* tangential velocity and turbulence intensity, has disappeared (or blasted).

A third flow state, a Weak axial Jet (WJ) in which the central vortex core is weaker because of a jet expansion angle higher than the one of a free Axial Jet under the same amount of swirl, appeared as an unstable, transient state with the flow bifurcating to the BB state (or to the AJ state in some different conditions) for long simulation times.
These flow states obtained in LOTAR have many features in common with the reference case of Vanierschot et al. [105]. A second useful consideration is that, because of hysteresis, a change in the simulation parameters (in the case of sensitive LES of swirling flows), should be accompanied by a re-initialization of the flow field. More generally, LES for swirled flows with combustion are also very likely to exhibit bifurcating behaviors. Since combustion can act as a triggering mechanism for bifurcations and instabilities, LES codes used to study turbulent swirled confined flames should be expected to exhibit a sensitivity to numerical details (similarly to what shown in this thesis) which is much larger than what has been observed in non-swirling free flames and this might raise significant difficulties.

Lire la deuxième partie de la thèse